Advances in Two-Dimensional THz Spectroscopy: Distinguishing Cascaded Nonlinear Optical Processes in ZnTe

Cross, Martin

Publication date:
2023

Document Version
Publisher's PDF, also known as Version of record

DTU Electro
Department of Electrical and Photonics Engineering

Advances in Two-Dimensional THz Spectroscopy:
Distinguishing Cascaded Nonlinear Optical Processes in ZnTe

Doctor of Philosophy

Author: Martin Cross

Supervisor: Prof. Peter U. Jepsen
Co-supervisors: Assoc. Prof. Edmund Kelleher

DTU Electro
Department of Electrical and Photonics Engineering
Technical University of Denmark
Ørsteds Plads
Building 343
2800 Kongens Lyngby, Denmark

Acknowledgements

Peter – Thank you for giving me the freedom to find my own way, and for always being there with some wit, good humor, and positivity even if I was just spinning in circles. I couldn't imagine a cooler supervisor!

Ed – I wouldn't be here writing this without you. Inviting me to Denmark was a life-changing experience I'll never forget, and always appreciate. It would be amazing to see you on the West coast—maybe 'have a natter' at SLAC or go for a climb :)

Colleagues and Friends at DTU – I've had an amazing time with you all. I couldn't imagine a better mix of people or a better place to do my PhD. Keep up the life/work balance!

Malte and Sergio – You truly became my family away from home. I'll really miss you guys. An office won't ever be the same again without the Tres Amigos.

Joanna – It's hard to imagine meeting someone so special over 5000 miles away. Thank you for always giving me something to look forward to :)

My Family – It was a hard era to be away from home. I want you to know that even though I didn't call enough, I was always thinking about you. Thank you for your unconditional love and support—I am forever grateful.

Summary

The present thesis summarizes recent developments in two-dimensional (2D) terahertz (THz) spectroscopy at DTU, including instrumentation, numerical pulse propagation simulations, and their combined application for distinguishing cascaded and direct nonlinear optical (NLO) process in ZnTe.

Chapter 1 begins with a brief motivational introduction to multidimensional spectroscopy, then delves into a ground-up overview of how 2D terahertz datasets, or 'maps,' are created and interpreted.

In Chapter 2, we describe the design, development, and configuration of the 2D THz instrument. We discuss the rational behind using what we call '2D THz-THz-polarimetry' as the detection method, as well as its implementation. Additionally, we provide several benchmarks of the instrument.

Chapter 3 focuses on the development of numerical pulse propagation simulations. These simulations enable us to isolate the underlying direct and cascaded NLO processes contributing to the measured 2D THz-THz-polarimetric maps.

In Chapter 4, we present 2D THz-THz-polarimetric measurements of direct and cascaded NLO processes in ZnTe, alongside corresponding numerical pulse propagation simulations. This comparative analysis allows us to effectively distinguish between cascaded and direct processes.

Finally, we conclude the thesis with a summary of the findings and directions for future research and development.

Resumé

Denne afhandling sammenfatter de seneste udviklinger inden for to-dimensionel (2D) terahertz (THz) spektroskopi på DTU, herunder instrumentering, numeriske pulspåvirkningssimuleringer og deres kombinerede anvendelse til at skelne mellem kaskade- og direkte ikke-lineær optisk (NLO) proces i ZnTe.

Kapitel 1 begynder med en kort motiverende introduktion til flerdimensionel spektroskopi og går derefter i detaljer med en grundlæggende oversigt over, hvordan 2D terahertz datasæt, eller 'maps', skabes og fortolkes.

I kapitel 2 beskriver vi design, udvikling og konfiguration af det 2D THz-instrument. Vi diskuterer begrundelsen bag brugen af det, vi kalder '2D THz-THz-polarimetri', som detektionsmetode, samt dets implementering. Derudover giver vi flere benchmarks for instrumentet.

Kapitel 3 fokuserer på udviklingen af numeriske simuleringer af pulspåvirkning. Disse simuleringer gør det muligt for os at isolere de underliggende direkte og kaskade NLO-processer, der bidrager til de målte 2D THz-THz-polarimetriske maps.

I kapitel 4 præsenterer vi 2D THz-THz-polarimetriske målinger af direkte og kaskade NLO-processer i ZnTe sammen med tilhørende numeriske pulspåvirkningssimuleringer. Denne sammenlignende analyse giver os mulighed for effektivt at skelne mellem kaskade- og direkte processer.

Til sidst afslutter vi afhandlingen med en opsummering af resultaterne og retningslinjer for fremtidig forskning og udvikling.

Preface

The work and findings reported in this thesis were undertaken during the period from March 1, 2020, to June 28, 2023, in the Group for Ultrafast Infrared and Terahertz Science, Department of Electrical and Photonics Engineering, at the Technical University of Denmark, DTU, in partial fulfillment of the requirements for the degree of Doctor of Philosophy in Photonics Engineering. The work was performed under the supervision of Prof. Peter Uhd Jepsen and Associate Prof. Edmund John Railton Kelleher.

The text, figures, and tables in this thesis are original, unpublished works of the author, Martin J. Cross.

The optical layout of the instrument is a legacy of the following individuals: Associate Prof. Pernille Klarskov Pedersen, Henrik Bødker Lassen, Mattias Rasmussen, and Dr. Korbinian Kaltenecker. Their specific contributions are unknown as their involvement predates mine. Most of the components are in their original location, albeit remounted and realigned. Besides inheriting the layout, the instrument development discussed herein is my own work.

The numerical simulations and measurements were performed by me. The development of the numerical simulations was guided by relevant existing literature, as attributed within the text.

Components used in the experiments were either commercially sourced or manufactured by the in-house workshop at DTU Electro.

The research was fully funded by the Independent Research Fund Denmark (Danmarks Frie Forskningsfond). Partial funding for my external research stay at SLAC National Accelerator Laboratory was provided by the host institution and the Otto Mønsteds Fond.

Kongens Lyngby, 2023-06-29

Martin J. Cross

Abbreviations

1D one-dimensional

2D two-dimensional

AC autocorrelation

AR anti-reflective

BBO β barium borate

BPF band-pass filter

BS beamsplitter

DAQ data acquisition

DAST 4-N, N-dimethylamino-4′-N'-methyl-stilbazolium tosylate

DFG difference frequency generation

DFT discrete Fourier transform

EO electro-optic

FME forward Maxwell equation

FOV field-of-view

FROG frequency resolved optical gating

FT Fourier transfrom

FWHM full-width half-maximum

GT Glan-Taylor

HeNe helium-neon laser

HWP half-wave plate

IR infrared

ND neutral density

NIR near-infrared

NL nonlinear

NLSE nonlienar Schrödinger equation

OAP off-axis parabolic mirror

ODE ordinary differential equation

OPA optical parametric amplifier

OR optical rectification

PD photodiode

PMT photomultiplier tube

PTFE polytetrafluoroethylene

QWP quarter-wave plate

SFG sum-frequency generation

SHG second harmonic generation

THz terahertz

UPPE unidirectional pulse propagation equation

ZnTe zinc telluride

Contents

Acknowledgements i

Summary iii

Resumé v

Preface vii

Abbreviations ix

Contents xi

Introduction 1

1 Two-Dimensional THz Spectroscopy 3
- 1.1 Examples of 2D Datasets . . . 3
- 1.2 Creating a 2D THz Dataset . . . 6
- 1.3 Nonlinear Spectroscopy . . . 8
- 1.4 General Approach for Analyzing 2D Datasets . . . 9
- 1.5 Frequency Vector Representation of 2D frequency-frequency maps . . . 14
- 1.6 Comparison of Instantaneous Nonlinearities . . . 15
- 1.7 Outstanding Issues . . . 18
- 1.8 Moving Forward . . . 19

2 Instrumentation 21
- 2.1 Optical Layout . . . 21
  - 2.1.1 Pump Path . . . 23
  - 2.1.2 Probe Path . . . 24
- 2.2 Alignment Tips and Tricks . . . 26
  - 2.2.1 Aligning Off-Axis Parabolic Mirrors . . . 26
  - 2.2.2 Aligning delay stages . . . 28
- 2.3 Optical Parametric Amplifier . . . 29
- 2.4 Polarimetry and EO detection . . . 29

2.5 Chopping and Timing . . . 31
2.5.1 Chopper phasing . . . 32
2.6 Benchmarking . . . 34
2.6.1 THz power measurement . . . 34
2.6.2 THz Spectrum Measurement . . . 35
2.6.3 Polarimetry Probe-Intensity Dependence . . . 35
2.6.4 Polarimetry WL-IPD4B-Count Dependence . . . 37

3 Numerical Pulse Propagation **41**
3.1 Derivation of the FME and NLSE . . . 42
3.1.1 Deriving the NLSE from the UPPE . . . 44
3.1.2 Deriving the FME from the UPPE . . . 45
3.1.3 Calculating DFT Terms in the FME Jacobian . . . 47
3.2 Calculating Polarization Terms . . . 49
3.2.1 THz-Probe Polarization Terms . . . 49
3.2.2 THz-THz Polarization Terms . . . 51
3.3 THz-THz simulations . . . 52
3.4 THz-probe simulations . . . 56

4 Nonlinear Optical Processes in ZnTe **59**
4.1 Reference Waveforms . . . 61
4.2 ZnTe Polarization Terms . . . 70
4.3 2D THz-THz Polarimetry of ZnTe . . . 77
4.3.1 Improvements and Future work . . . 84

Conclusion **87**

Appendices **89**

Appendix A Nonlinear Polarizations **91**
A.1 ⟨110⟩ ZnTe THz-THz Nonlinear Polarizations . . . 92
A.2 ⟨110⟩ ZnTe THz-Probe Nonlinear Polarizations . . . 93
A.3 ⟨100⟩ ZnTe THz-THz Nonlinear Polarizations . . . 95
A.4 ⟨100⟩ ZnTe THz-Probe Nonlinear Polarizations . . . 96

Publications and Contributions **99**

Bibliography **100**

Introduction

Why terahertz? Why multiple dimensions? As a practical matter, the short answer is that I've had the privilege and good fortune to join the Ultrafast Infrared and Terahertz Science group at DTU. The long answer starts with the surprising fact that *"virtually every force we experience in everyday life, with the exception of gravity, is electromagnetic in origin"* [23]. These forces are carried by electromagnetic fields, with those oscillating near 10^{12} cycles per second—terahertz (THz) frequencies—forming a particularly interesting range. Within this range lie the fundamental 'structural' motions of the nuclei composing the molecules and solids that make up our world, such as rotations, vibrations, librations, and other complex movements. THz spectroscopies have the advantage of specifically exciting and probing these motions. In contrast, long-established infrared (IR) spectroscopies predominantly couple to these motions indirectly through their harmonics or, more often, electronic rather than structural excitations [42]. These higher-frequency excitations obscure the influence of the fundamental motions.

However, this is not to say that THz excitations cannot generate a wide array of complicated phenomena. THz field strengths commonly exceeding tens of $\mathrm{kV/cm}$ allow multiple linear and nonlinear pathways to excite fundamental structural motions [39] or even induce symmetry-breaking structural phase transitions that create new ones [37, 43, 51]. The resulting nonlinear signals are often interwoven and difficult to separate. In order to disentangle them, *multidimensional* spectroscopies that probe the broader pattern of the excitation from two-or-more THz pump pulses have been developed [32, 38, 42, 52]. In the following chapter, we will explore two-dimensional (2D) spectroscopy in more detail.

So far we have emphasized the study of structural motions, but it is important to be aware that we cannot always ignore the electronic contributions at THz frequencies. Indeed, Sidler and Hamm [52] compare nonlinear contributions to 2D THz-Raman spectra in amorphous ice and find a significant electronic contribution, Pal et al. [44] highlight the influence of electronic interband transitions on soft-mode nonlinearities in ferroelectrics, and Kuehn et al. [34] drive the third-order nonlinear response of n-doped GaAs/AlGaAs quantum wells far past the perturbative limit.

In this thesis, we explore the influence of direct and cascaded nonlinear processes in the prototypical zincblende crystal zinc telluride (ZnTe). The processes studied herein are, for the most part, off-resonant and electronic in nature. In comparison to a direct process, cascading involves a *sequence* of lower-order nonlinear processes. The sequential nature provides a degree of flexibility that allows cascades to dominate the direct processes they resemble [10], or proceed when a direct process is symmetry forbidden [15, 25]. The overall cascaded process scales with the constituent fields in the same way as a single quasi higher-order direct

process, making it challenging to separate the two. However, we demonstrate that 2D THz spectroscopy, combined with numerical pulse propagation simulations, allow us to discriminate direct and cascaded nonlinear processes in ZnTe up to third-order.

Specifically, we employ THz-THz-polarimetry, which is technically identical in its implementation to often used THz-THz-Raman spectroscopy [32, 38, 42, 52]. In both, two THz pumps pulses excite the sample, and a third optical probe pulse measures the material response through a modulation of its polarization. The nominal difference between the two techniques reflects the underlying processes being measured. Polarimetry encompasses all sources of polarization modulation, be they inelastic Raman scattering or photon-energy conservative optical mixing processes. In our experiment, the detected signal is predominantly due to the latter electronic contributions. The construction of the 2D THz-THz-polarimeter is discussed in Chapter 2.

The corresponding simulations are developed in Chapter 3. They are critical for discerning whether the nonlinear signals measured with 2D THz-THz-polarimetry in ZnTe occur from 'THz-THz' processes between the THz pump pulses themselves or from 'THz-probe' processes between the THz pump pulses and the optical probe pulse used to read out the response. Unlike in a physical crystal, the simulations allow us to freely enable or disable nonlinear processes to better understand their individual or coupled contributions.

The measurements and simulations are brought together in Chapter 4, where we perform a set of experiments to isolate the second- and third-order contributions to the nonlinear signal in ZnTe. In the first experiment, a $\langle 100 \rangle$ cut ZnTe crystal is used to effectively disable second-order ($\chi^{(2)}$) processes for all field polarizations, regardless of cascading. This serves as a reference for the signature of third-order ($\chi^{(3)}$) processes alone. In the second experiment, a $\langle 110 \rangle$ cut ZnTe crystal is oriented in a way that second-order processes can only occur by cascading through a primary third-order process.

We will carry out the experiments both physically and numerically. With a comparative analysis of the results, we hope to show a high-degree of self-consistency. This will provide the confidence to further utilize the simulations to selectively enable or disable the underlying THz-THz and THz-probe interactions, with the aim of isolating their contributions. Identifying the contributions will allow us to assign specific direct and cascaded nonlinear optical processes to the features in the 2D THz-THz polarimetry maps using the frequency vector representation developed by Kuehn et al. [34, 35].

CHAPTER 1

Two-Dimensional THz Spectroscopy

In this chapter, we present a ground-up overview of two-dimensional (2D) terahertz (THz) spectroscopy. We begin by showcasing the wealth of information generally contained in 2D datasets through a few examples. The details in these examples are not essential, so the reader is free to only retain what interests them.

Subsequently, we lay the ground work essential for understanding the main results presented in Chapter 4. This begins with a high-level explanation of how the 2D maps are constructed from multiple one-dimensional (1D) slices, and how we extract the nonlinear components from these maps. We then guide the reader through the interpretation of an example 2D THz dataset and introduce two simple models for linking the features in these maps to physical processes in the material. The limitations of these models are the point of departure into the core developments of this thesis. We outline the steps to be taken in addressing these limitations and propose the experiment that forms the main result discussed in Chapter 4.

1.1 Examples of 2D Datasets

Before discussing the underlying physics in the 2D maps or how to interpret them, we want to generally motivate the utility of two-dimensional datasets through three examples.

See the forest through the trees

Let us begin by skipping to the end result for a moment to appreciate the broader picture gained from 2D data. In Fig. 1.1 we compare one of our simulations to the measured experimental data. Above and below the 2D maps are slices along their centers. These slices are only one of many one-dimensional (1D) studies that make up the 2D maps. The right column in Fig. 1.1 is unique to 2D-spectroscopy, providing an additional perspective not possible in one-dimension—we will expand on this in the later sections. What we hope the reader can appreciate is that the fine details in any given 1D slice carry relatively limited information in comparison to the broader pattern of how a collection of slices relate to each other. While the simulated and measured 2D maps are not exact replicas, there are clear patterns and symmetries that they share.

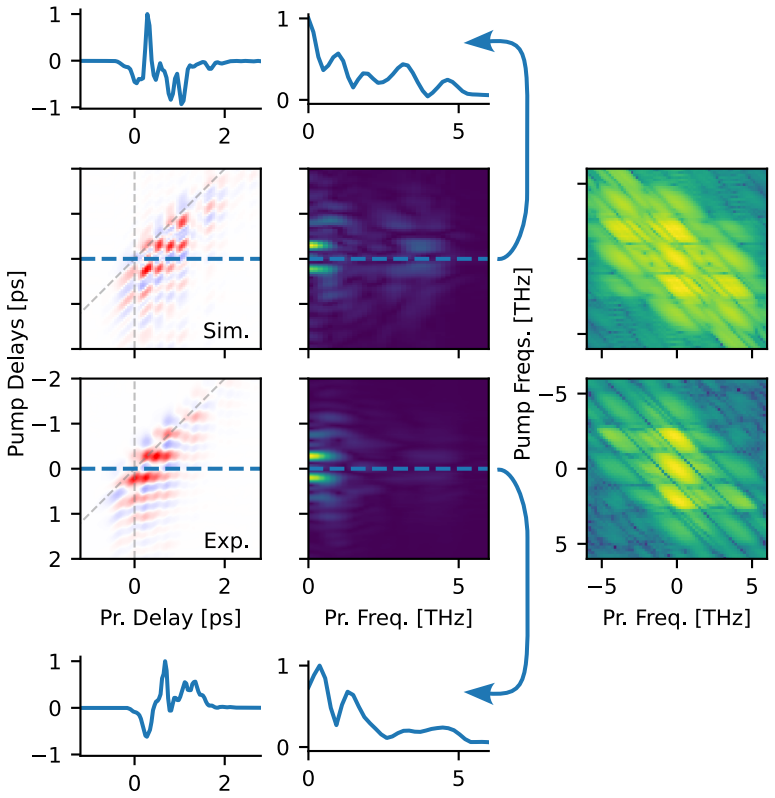

Figure 1.1. Comparing simulated (top) and measured (bottom) 2D THz maps to 1D slices through their centers. The right column is unique to 2D spectroscopy and provides additional insights. For now, the reader is only asked to appreciate the qualitative wealth of information provided by the 2D datasets.

The complex plane

The complex plane is a 2D dataset scientists will already be familiar with. A complex number z can be decomposed into real and imaginary components, x and y, such that $z = x + iy$. The number can then be represented by a point (x, y) on the complex plane in the Cartesian coordinate system, as done in Fig. 1.2. An elegant example for demonstrating how information is lost when projecting from two-dimensions (x, y) to one-dimension (x) starts with the unit circle

$$z = e^{i\theta} = \cos(\theta) + i\sin(\theta). \tag{1.1}$$

We have plotted z in Fig. 1.2(a), and highlighted five *unique* points. One way to project these points onto a single dimension is to only retain their real-value, $\mathrm{Re}(z) = x = \cos(\theta)$, and discard the imaginary component $\mathrm{Im}(z) = y = \sin(\theta)$, as shown in Fig. 1.2(b). In effect, the unit circle has been flattened into a line, and our five unique points have been reduced to three. Another projector is the magnitude operator $||$, which returns the distance of the points

from the origin (0, 0). For points on the unit circle, $|z| = 1$. Thus, in Fig. 1.2(c) all points on the unit circle have been overlapped on a single point at $x = 1$.

As much as this example demonstrates the potential for a severe loss of information though dimensional reduction, a beautiful aspect is that it also shows how a carefully thought-out 1D experiment can retain it—2D experiments are not the be-all end-all solution! If one knows *a priori* that the points lie on a circle of constant radius, then the best single dimension to project onto is $\hat{\theta}$ or the angle of the points about the center (0, 0). From this perspective, exploratory 2D experiments offer a rapid avenue to devising targeted 1D studies.

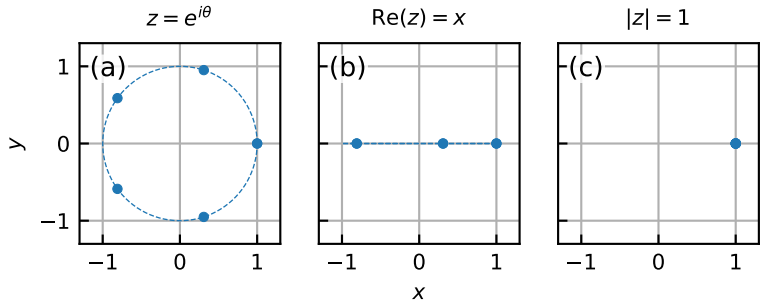

Figure 1.2. Examples of information lost when projecting points from the 2D complex plane to the 1D real line. (a) Points z on a circle in the complex plane. (b) The real components of z. (c) The magnitudes of z.

An ultrafast-optics example

The 2D spectrograms produced by frequency resolved optical gating (FROG) are familiar to those who work with ultra-short laser pulses. For the uninitiated, these maps show the spectrum (frequency composition or 'color') of the pulse as a function of time. FROG was the first technique allowing full characterization of sub-femtosecond duration pulses—the shortest events ever created [55]. To fully appreciate this feat, consider that "30 fs is to 1 second as 1 second is to a million years" [55]. With the proper retrieval algorithm, one can extract the unique spectral phase and amplitude of the pulse that generated the spectrogram.

Without getting lost in the details [55], let us look at the example in Fig 1.3. The colored maps (a)-(c) are the spectrograms of three pulses that are identical except for a linear chirp. The pulse in (a) is down-chirped, its frequency decreases with time, (b) is unchirped (zero-phase), and (c) is up-chirped. One can calculate the time-averaged spectrum by integrating the 2D spectrogram along the delay axis (*i.e.* summing columns left to right). The time-averaged spectrum is shown in (d) and is identical for all pulses since they only differ by a spectral phase (the chirp). This 1D measurement is what we would get with an optical spectrum analyzer, and it cannot distinguish any of the three pulses. We can also integrate the spectrograms along the frequency axis (*i.e.* summing rows top to bottom) to calculate the autocorrelation of the pulses (e)-(g)—another type of 1D measurement. Here we are able to distinguish the chirped pulses from the unchirped pulse, but we cannot tell if the chirped pulse is up- or down-chirped.

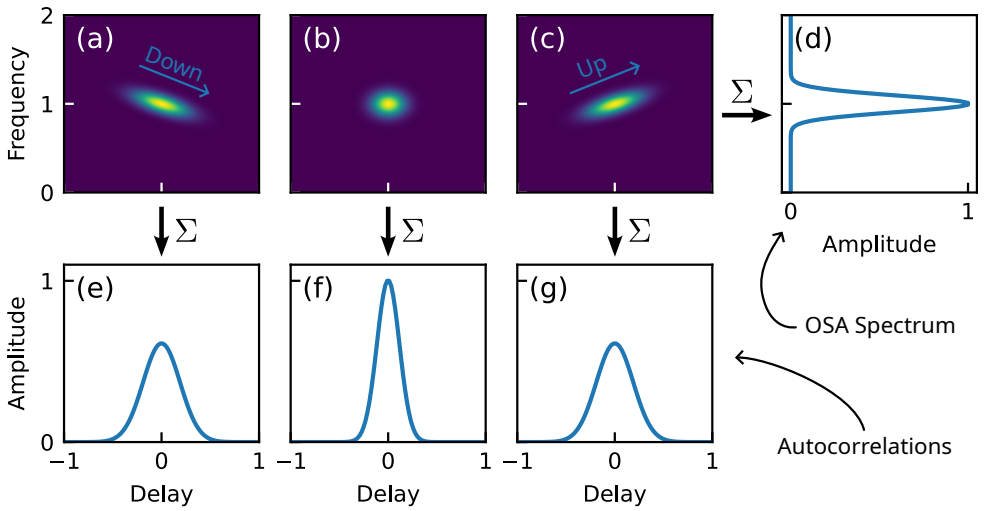

Figure 1.3. Frequency resolved optical gating (FROG) as an example of 2D spectroscopy. (a)-(c) FROG spectrograms showing the frequency vs. time of three unique optical pulses. (a) down-chirped, frequency decreases with time. (b) Unchirped. (c) Up-chirped, frequency increases with time. (d) The sum across columns of spectrogram (a), (b) or (c). Equivalent to the 1D spectrum measured on an optical spectrum analyzer (OSA); note that all pulses have the same 1D spectrum. (e)-(f) The sum across rows of (a)-(c). Equivalent to the 1D autocorrelation of each pulse; note that pulse (a) and (c) have the same autocorrelation.

In conclusion, these are only a few examples of the numerous 2D datasets studied across the sciences, and of course, two dimensions is not the limit. We hope the reader can now appreciate the relative wealth of information contained in a 2D dataset, and the potential for losing a significant amount of information when reducing the dimensionality.

1.2 Creating a 2D THz Dataset

2D spectroscopy is a natural extension of 1D pump-probe spectroscopy, as illustrated in Fig. 1.4. In a pump-probe experiment, the 'pump' pulse excites the sample, and the 'probe' pulse measures a coherent change in one or more properties of the material after a time delay t. In the depicted example, the pump pulse enters the ZnTe sample first and changes its properties. After some time t, the probe enters and samples what remains of those changes. By sweeping t from negative to positive times, one can record the time evolution of the property of interest. We have used ZnTe here because it has the distinctive property that the 'change' sampled by the probe is approximately proportional to the pump's electric field at that very moment. Consequently, the recorded pump-probe waveforms provide a reasonably accurate

representation of the pump pulse's electric field. Note, however, that the limitations of this approximation are the basis of this thesis!

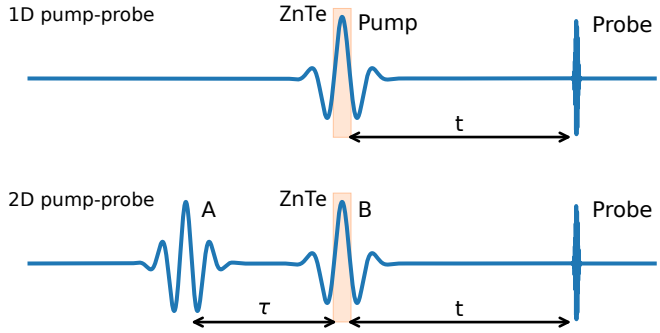

Figure 1.4. 2D spectroscopy as an extension of 1D pump-probe spectroscopy. In 1D pump-probe spectroscopy, a 'pump' pulse excites the sample and a 'probe' pulse measures coherent changes after a time delay t. By sweeping t, the time evolution of the property of interest can be recorded. In ZnTe the measured changes are approximately proportional to the pump's electric field. 2D spectroscopy introduces a second delay dimension τ, representing the separation between two pump pulses $A = E_A(t)$ and $B = E_B(t)$. One can generate a 2D map by stepping τ and sweeping t—*i.e.* stacking many 1D waveforms.

2D spectroscopy adds a second delay dimension τ, which in our case corresponds to the separation between two pump pulses $A = E_A(t)$ and $B = E_B(t)$. By iteratively stepping τ and sweeping t, one can generate 2D maps, such as those in Fig. 1.5. Each horizontal slice though these 2D maps is a single pump-probe waveform with a different delay between A and B. The 'AB'[1] map shows the response for the simultaneous application of A and B. A horizontal slice across this map at $\tau = 0$ shows the A and B pulses are overlapped when there is zero delay between them. In contrast, when τ is negative/positive, the A pulse comes before/after the B pulse.

Because the B pulse's position in t is independent of τ, each horizontal pump-probe cross-section of the B pulse is identical. The peaks and valleys of its field therefore form vertical red and blue stripes in the 2D maps. In comparison, the position of a peak in the A pulse is progressively τ-shifted and follows the relationship $t_{pk}(t) = t_{pk}(0) + \tau$, which is a diagonal line in the maps.

Notably, in Fig. 1.5, we display maps of the response for the A and B pump pulses individually, as well as simultaneously. Doing so is not just for pedagogical purposes, and in the lab, we alternately block the pump pulses to concurrently record all three maps. In the next section, we will discuss how these three maps are used for *nonlinear* spectroscopy.

[1] When A, B or AB are not italicized, they refer to the recorded response for the application of the A, B or $A + B$ pump pulse fields respectively.

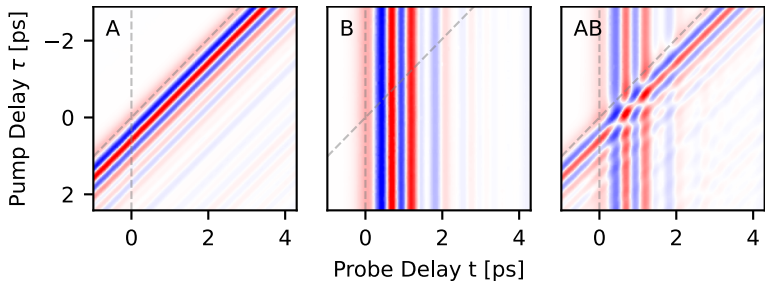

Figure 1.5. 2D maps of the responses A, B and AB for the A, B and $A + B$ pump pulse fields respectively, in a ZnTe detection crystal. Every horizontal row in the map is a separate 1D scan. The response is predominantly proportional to the instantaneous field strength of the pump pulses. Dashed lines mark the leading edge of the pulses. Although not the focus of this figure or Chapter, for reference, the ZnTe crystal is $1\,\mathrm{mm}$ thick, $\langle 110 \rangle$ cut and oriented as shown in Fig. 4.8(c).

1.3 Nonlinear Spectroscopy

As previously mentioned, the response of ZnTe is not strictly linear. In fact, any material exhibits a nonlinear response when subjected to a sufficiently high field strength.

Nonlinear spectroscopy involves isolating the nonlinear (NL) portion of the material response $R(E(t))$, where $E(t)$ is the applied time-varying electric field. To achieve this, we utilize the three maps (*i.e.*, for the A pulse, the B pulse, and both the $A+B$ pulses combined) to calculate the residual or 'nonlinear' component by checking for the additivity condition:

$$R(A+B) \neq R(A) + R(B) \tag{1.2}$$

$$\therefore \mathrm{NL} = R(A+B) - \big(R(A) + R(B)\big) \tag{1.3}$$

To illustrate this concept, let's consider the toy response function $R\big[E(t)\big] = E(t)^2$. In this case, the nonlinear component can be calculated as follows:

$$\mathrm{NL} = (A+B)^2 - (A^2 + B^2) = 2A{\cdot}B, \tag{1.4}$$

with $A = E_A(t)$ and $B = E_B(t)$. Notice that only the cross-term $2A{\cdot}B$ depending on *both* the A and B pulse is retained. This is an important point: the 'nonlinear' signal we measure does not include nonlinearities due to a single pulse field, *i.e.* terms such as A^2 or B^2. Subtracting the responses as we have done in calculating NL is often referred to as a 'differential measurement'. Its importance lies not only in removing single-pulse nonlinearities, but primarily in eliminating the dominant linear A and B components that inherently depend on only one of the fields.

Fig. 1.6 shows how we derive the residual NL signal from the maps in Fig. 1.5. The NL signal only exists in the unhatched region where both the A and B pulse overlap. In the hatched region, where at most one pulse is present at any given pump/probe delay, the large linear component and single-pulse nonlinearities are below the noise floor. From a technical

perspective, this demonstrates the effectiveness of the differential measurement. More generally, it upholds the necessity for causality when considering a signal dependent on both A and B—it cannot exist before the latter of the two pulses arrives [34].

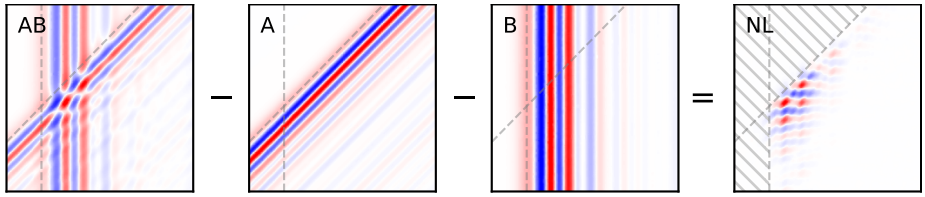

Figure 1.6. Pictogram depicting how the nonlinear (NL) signal is calculated. We subtract the response for the A and B pulse alone from the simultaneous response 'AB', where the sum of the pulses, $A + B$, is applied. Causality requires the NL signal only exist after the arrival of *both* A and B (the unhatched region). Differential measurement ensures signals in the hatched area are removed.

1.4 General Approach for Analyzing 2D Datasets

An effective method for analyzing these 2D maps is to view them both in the time and frequency domains at once [32], as is done in the keystone figure for this section, Fig. 1.7. Each row corresponds to one of the measured A, B or AB responses, or the calculated NL signal. In the left column, we have the measured time-time (t-τ) maps of the data. In the center column we have Fourier transformed the data along the probe axis t to generate a time-frequency (τ-f_{pr}) map, and in the right column we apply the Fourier transfrom (FT) once more along the pump-axis τ to get a frequency-frequency (f_{pu}-f_{pr}) map. To highlight low-intensity spectral features, the f_{pu}-f_{pr} map is log-scale. Furthermore, we have plotted the full frequency domain to more easily visualize the symmetries of the spectral magnitudes, for example, the parallelogram shaped pattern in the NL f_{pu}-f_{pr} map. However, because the measured data is real-valued, the FT is Hermitian and could be uniquely represented on just half of the domain [8, p.13].

The maps become progressively more complicated from top-to-bottom, so we will begin by stepping through the columns of the **B-row**. In the time-time plot, we see that the response oscillates along the probe axis (red-blue-red...) but does not vary along the pump axis (solid vertical red and blue strips). When we FT along the probe axis to obtain the central time-frequency map, we see that the spectral magnitude of the oscillation is peaked around $\nu_{\mathrm{B}} = 2\,\mathrm{THz}$. Because the response is invariant along the pump-axis, the spectral magnitude is the same for all pump delays. In other words, all rows in the time-time and time-frequency maps are the same. When we subsequently FT along the pump-delay axis to get the frequency-frequency map, the time-invariance leads to a nearly pure zero-frequency (or 'DC', as an electrical engineer might say) spectral magnitude in the pump-frequency dimension. The frequency-frequency map thus has spots at $[-2, 0]\,\mathrm{THz}$ and $[2, 0]\,\mathrm{THz}$, that is, at $\pm 2\,\mathrm{THz}$ along the probe-frequency axis and $0\,\mathrm{THz}$ along the pump-frequency axis.

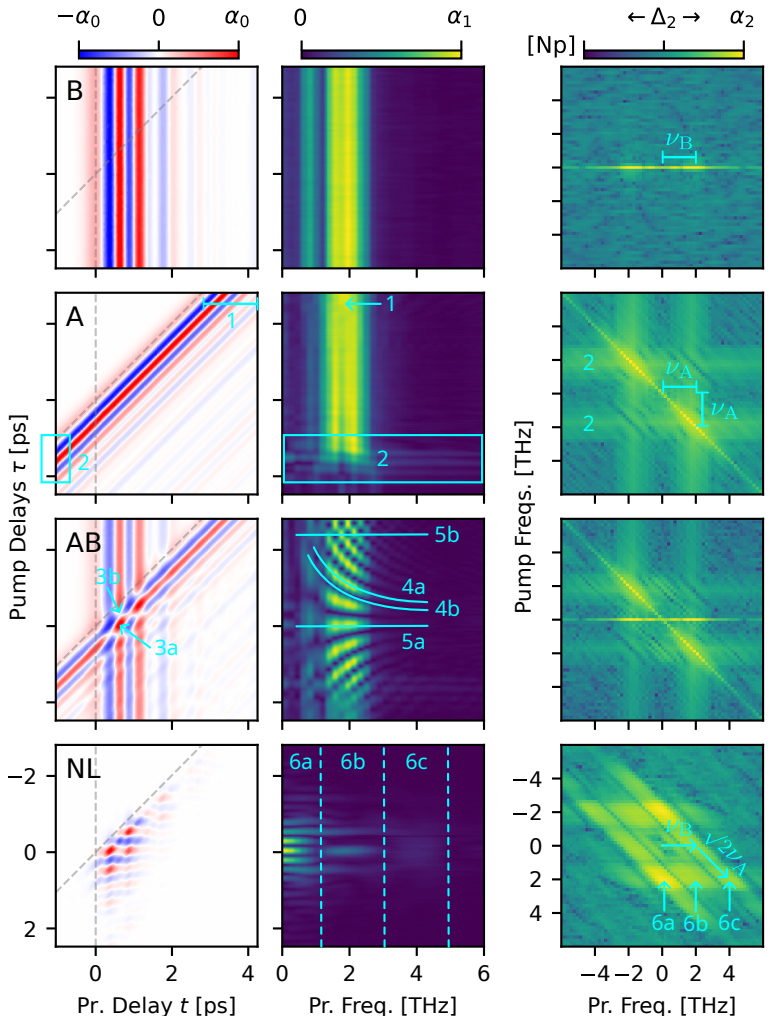

Figure 1.7. Time- and frequency-domain analysis of 2D maps. Rows A, B and AB represent measured responses; NL is the calculated nonlinear signal. The columns show different time-frequency representations: (left) time-time maps, linear-scale; (center) time-frequency maps, absolute-value linear-scale; (right) frequency-frequency maps, log-scale. Log-scale is used to highlight low-intensity spectral features in the frequency-frequency maps. The central frequencies of pulse A and B are $\nu_\mathrm{A} \simeq \nu_\mathrm{B} \simeq 2\,\mathrm{THz}$. The scales $\alpha_0, \alpha_1, \alpha_2$ and Δ_2 are not equal, and in this case, arbitrary. *Artifacts due to data truncation:* (1) shorter duration recording leads to reduced spectral resolution, 'filling' a spectral dip; (2) clipping leads to a step-function like edge with broadband spectral components. (3a/b, 4a/b) Constructive/destructive interference. Constructive interference follows a $f_\mathrm{CI} = m/\tau$ dependence. (5a→5b) Number of constructive interference peaks increases with τ. *New spectral features:* (6a) near-DC components due to horizontal red-blue-red banding in the time-time map; (6b) correlates to constructive interference at $\sim \nu_\mathrm{A/B}$ (only red bands); (6c) 'cloud' of frequencies around $\sim 2 \times \nu_\mathrm{A/B}$. Vector addition of the central frequencies points to (6c): $[\nu_\mathrm{B}, 0] + [\nu_\mathrm{A}, \nu_\mathrm{A}] = [\nu_\mathrm{B} + \nu_\mathrm{A}, \nu_\mathrm{A}] = [4, 2]\,\mathrm{THz}$.

Let us now consider the **A-row**. In the time-time map, there are oscillations along both the pump and probe axes. Visually, the wavefronts (contours of constant amplitude or red/blue stripes) appear more closely spaced than those of the B pulse. However, the time-frequency map reveals that horizontal slices through the A pulse time-time map also have a central frequency, ν_{A}, of approximately $2\,\mathrm{THz}$. Upon further reflection, one can reason that slicing diagonally across the wavefronts effectively widens the alternating red and blue bands.

The positive $45\,\mathrm{deg}$ slope from left to right of the wavefronts simply results from delaying the A pulse by τ. Recalling the FT shift theorem [8, p.111], a shift in the time domain is only an associated phase in the frequency domain. Thus, the magnitudes of the FT in the central time-frequency plot are the same for each row, except at the top and bottom of the map where there are measurement artifacts due to the response being clipped at the edges of the map. This 'windowing' results from only being able to scan a finite time-domain. In signal processing, this would be referred to (somewhat uncreatively) as a 'rectangular window', since all the measured data is equally weighted.

The clipping has two main effects, highlighted by the following annotations in the figure: (1) the recorded response duration along the probe-axis is shorter near the upper-right of the map, reducing our resolution in the frequency domain and thus filling a spectral dip just below $2\,\mathrm{THz}$; (2) the response is discontinuously truncated in the lower-left, effectively creating a step-function that has very broad spectral content. In the frequency domain this results in a nearly uniform band of spectral magnitudes across all frequencies. These bands are even more evident in the frequency-frequency plot. The vertical broad-spectrum bands in the frequency-frequency plot come from the discontinuity in the upper-right of the time-time map when taking the second FT along the pump-delay axis.

Because the wavefronts are on a positive $45\ deg$ slope from left to right, both vertical and horizontal cuts through the map will yield the same pulse shape—the location of the cut only determines by how much the waveform is shifted in time. Therefore, if the time-time map is instead Fourier transformed along the pump-delay axis, we will get a frequency-time map the is simply a rotated version of the time-frequency map. These vertical frequency components are the reason why the spectrum of the A pulse is displaced by $[\nu_{\mathrm{A}}, \nu_{\mathrm{A}}]\,\mathrm{THz}$ in the frequency-frequency map. Given the similarity of the B and A time-frequency maps, one might be wondering how a FT of the latter yields such a different frequency-frequency map: see Note 1.1 for details.

Before looking at the AB-row, it is useful to note that one can also take an 'image processing' perspective to analyze the results. The measured time-time maps are effectively images that can be decomposed into a spectrum of spatial frequencies. The locations of features in the frequency-frequency maps are related to the magnitude and direction of the wavevector of a component spatial frequency, where the direction is normal to the wavefront (contour of constant amplitude). For the B response, one can see that the wavefronts run vertically, hence the wavevector points horizontally and the two points in the frequency-frequency map are displaced horizontally from the origin by $[\pm\nu_{\mathrm{B}}, 0]\,\mathrm{THz}$. For the A response, the wavefronts

Note 1.1 FT of the A pulse time-frequency map

The time-frequency maps for the A and B pulses are similar, since the method used to generate them is the same (to be discussed in Section 2.1). One might briefly be confused how a second FT along the pump-delay axis of the time-frequency map could lead to the vertically displaced spots in the frequency-frequency map. The answer is simple: we do not FT the map as it is plotted, which only shows the spectral magnitudes, but rather the complex-valued map that also contains phase information. In the left two columns of Fig. 1.8 we have plotted the *real*-part of the complex time-frequency maps for the A and B pulses. For the B pulse there are no oscillations along the pump-delay axis, but for the A pulse there are clear oscillations. These maps corroborate the clear differences seen in the time-time maps for the A and B pulse.

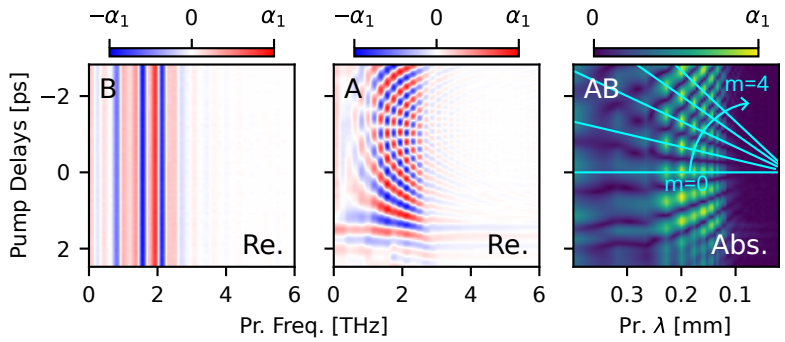

Figure 1.8. Complementary perspectives on Fig. 1.7. (left/center) Real component of the time-frequency maps for the (B/A) response. (right) Time-frequency spectral magnitudes for the AB response plotted against wavelength instead of frequency. The lines are on $\tau = m\lambda_{\mathrm{rm}}/c$, where m is an integer, c is the speed of light and λ_{rm} the wavelength of constructive interference. The scales α_1 vary between the plots, and in this case, are arbitrary.

run diagonally across the image with a positive slope from left to right. Again, the wavevector is normal to these fronts, thus we get two points displaced by $[\pm\nu_{\mathrm{A}}, \pm\nu_{\mathrm{A}}]$ THz along a negatively sloped line in the frequency-frequency map. To follow this convention, note that the pump-frequency axis has intentionally been flipped, with positive values at the bottom and negative values at the top.

The **AB-row** maps are predominantly a linear combination of the A and B maps. There are significant nonlinear components, but they are only evident after taking the differences of the maps [Eqn. (1.3)] as done in the NL-row. The main features in the time-time AB plot are areas of constructive (3a) and destructive (3b) interference where the pulses overlap (see annotations). Spectrally, we also see a clear pattern of constructive (4a) and destructive (4b) interference. The arcs of constructive interference follow a $f_{\mathrm{CI}} = m/\tau$ dependence, where

m is an integer. A special case is when the A and B pulses completely overlap ($\tau = 0$) and $m = 0$, where we see constructive interference at all frequencies (5a). Generally, as the delay between pulses increases, so too does the number of interference peaks (5b). This relationship is more clear if we plot the AB time-frequency map in terms of the probe-*wavelength,* as done in Fig. 1.8. In these units, the arcs of interference become lines defined by $\lambda_{\mathrm{CI}} = c\tau/m$, where c is the speed of light. The delay between pump-pulses is analogous to the distance between mirrors in an etalon. Light will interfere constructively when the round-trip distance is equal to a multiple of the wavelength. From a frequency perspective, the m-th harmonic of the light will be resonant with the etalon. This suggests another useful perspective on 2D spectroscopy: the pump-delay interferometrically selects a range of frequencies with which to pump the sample; sweeping the pump-delay is effectively like tuning the frequency of the effective $(A + B)$ pump pulse.

The **NL-row** in the main figure (Fig. 1.7) is rich with new information that, as illustrated in Fig. 1.6, occurs only once the A and B pulse have both arrived. Intuitively, the temporal peaks in the NL signal align with regions in the AB time-time map where strong constructive or destructive interference occur. A prominent feature of the temporal peaks is that they lie in horizontal bands of alternating polarity (red and blue). Notably, in addition to these continuous 'DC' offsets, is a more rapid modulation or structuring that is particularly evident in the negative blue bands. Comparing with the time-time map in the AB-row, it is clear the modulation period is shorter than the fundamental oscillation period of the pump pulses, which correspond to the central frequencies ν_{A} and ν_{B}.

In the time-frequency maps, the DC offset of each band is evident around $0\,\mathrm{THz}$ (6a), where we also see similar banding. The banding carries over due to the alternating nature of the temporal bands in the pump-delay direction, which have nodes or zeros between the red and blue stripes. Interestingly, There is also banding around the central frequencies ν_{A} and ν_{B} at approximately $2\,\mathrm{THz}$ (6b). However, in this case, every other band is missing. The remaining bands appear to be correlated to the red temporal bands where constructive interference takes place.

The higher frequency modulations on the DC bands manifest as a 'cloud' centered around $4\,\mathrm{THz}$ (6c), which is twice the value of ν_{A} and ν_{B}. In the frequency-frequency map we see there is one prominent spot located at a probe frequency of $4\,\mathrm{THz}$. It is shifted along the pump frequency axis by $2\,\mathrm{THz}$. Based on the frequency-frequency maps for the A and B pulses, it is apparent that the vector-sum of their frequency components overlaps this new feature at $[4, 2]\,\mathrm{THz}$ in the NL map. Similar arguments can be made for the other features, as they generally fall on a grid spanned by the basis vectors $[\nu_{\mathrm{B}}, 0]$ and $[\nu_{\mathrm{A}}, \nu_{\mathrm{A}}]$ for the B and A pulse respectively. We will expand on this frequency vector representation in the next section.

1.5 Frequency Vector Representation of 2D frequency-frequency maps

A frequency vector representation was employed by Kuehn et al. [34] for a third-order (four-wave-mixing) signal, and generally can be used to assign plausible nonlinear mixing processes to the discretely spaced features in the 2D frequency-frequency maps. In Fig 1.9 we have applied the technique to the second-order nonlinear optical processes listed in Boyd [7, p.7]. Namely, second harmonic generation (SHG), optical rectification (OR), sum-frequency generation (SFG), and difference frequency generation (DFG). For simplicity, it is assumed that the pulses are plane waves with a carrier frequency $\nu_0 = \nu_{\mathrm{A}} = \nu_{\mathrm{B}}$. The fields are then defined as

$$\tilde{E}_B(t) = \mathcal{E}_B e^{i2\pi\nu_0 t} + \mathcal{E}_B^* e^{-i2\pi\nu_0 t} \tag{1.5}$$

$$\tilde{E}_A(t,\tau) = \mathcal{E}_A e^{i2\pi\nu_0 (t+\tau)} + \mathcal{E}_A^* e^{-i2\pi\nu_0 (t+\tau)} \tag{1.6}$$

where $\mathcal{E}_{B/A}$ are the complex amplitudes, and $\mathcal{E}^*_{B/A}$ are their complex conjugates. The tilde over $\tilde{E}$ indicates the single-frequency approximation. Before the sample the total pump field is their sum,

$$\tilde{E}_{\mathrm{pu}}(t) = \tilde{E}_B(t) + \tilde{E}_A(t). \tag{1.7}$$

Inside the sample these fields generate additional polarization terms. The second-order polarization term is [7]

$$\tilde{P}^{(2)}(t) = \epsilon_0 \chi^{(2)} \tilde{E}_{\mathrm{pu}}(t)^2 \tag{1.8}$$

$$\tilde{P}^{(2)}(t) = \sum_n \mathcal{P}(\nu_n) e^{i2\pi\nu_n t}, \tag{1.9}$$

where $\mathcal{P}(\nu_n)$ is the complex amplitude of the polarization component oscillating at frequency ν_n and $\chi^{(2)}$ is the second-order nonlinear susceptibility. The polarization amplitudes for the various second-order products are listed on the right of Fig 1.9. Only half the terms are listed, which correspond to the points in the lower-right quadrant of the frequency-frequency map; their complex conjugates also exist, which are at the negative frequencies in the upper-left quadrant. In the frequency-frequency map, one interaction with the positive frequency component of $\tilde{E}_B$ displaces us by $[\nu_0, 0]$. For the positive frequency component of $\tilde{E}_A$, it is $[\nu_0, \nu_0]$. It is the presence of τ in $\tilde{E}_A$ that results in the vertical, pump-frequency component of its vector. The negative frequency components of $\tilde{E}_B$ and $\tilde{E}_A$ similarly have associated vectors, but pointing in the opposite direction.

When we overlay the positions of the second-order mixing products on our measured NL signal in Fig.1.9(left) we see that the corners of the parallelogram pattern likely result from sum- and difference-frequency products between the A and B pulse. It is also reassuring to see that single-pulse second-harmonic products are not present in the map, as expected for a differential measurement. Notably, the 'four leaf clover' shaped pattern cannot be explained by second-order mixing products and there is a central spot coincident with the

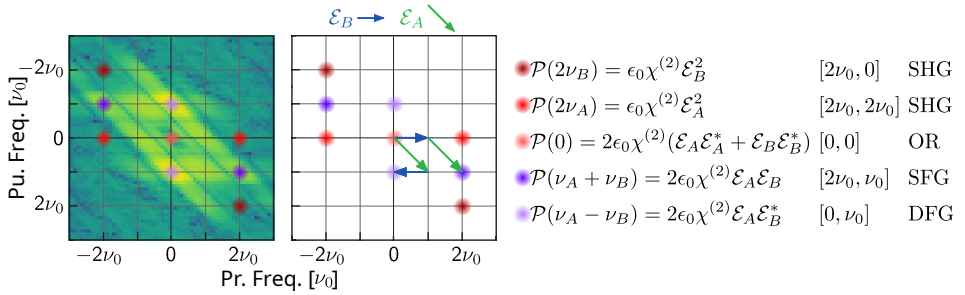

Figure 1.9. Second-order contributions to 2D frequency-frequency maps in the plane-wave approximation. The carrier frequency is ν_0. (right) Second order polarization amplitudes [7]. Purple and red dots are for mixed and single-pulse nonlinearities, respectively. Second harmonic generation (SHG); sum frequency generation (SFG); difference frequency generation (DFG); optical rectification (OR). (center) Vector-chain diagram derived from [34] for the second-order polarizations. One photon from the B pulse ($\propto \mathcal{E}_B$) moves us by $[\nu_0, 0]$ and for the A pulse ($\propto \mathcal{E}_A$) it is $[\nu_0, \nu_0]$. The complex conjugates $\mathcal{E}_B^*$ and $\mathcal{E}_A^*$ point in the negative direction. Vector addition to the locations for SFG and DFG are demonstrated. (left) Overlay on the nonlinear signal from Fig. 1.7, with $\nu_0 = 2$ THz, showing SFG and DFG likely contribute to the corner features.

optical-rectification products that should be eliminated by the differential measurement. We will come back to these outstanding issues in a moment, but for now let us apply the insights gained to some simple instantaneous models.

1.6 Comparison of Instantaneous Nonlinearities

A particularly powerful aspect of 2D spectroscopy is being able to create maps of model nonlinearities and compare those 'fingerprints' to the measured data. We can easily create several instantaneous models using the measured A and B maps. 'Instantaneous' refers to using the amplitude of the pump fields at a single time, rather than integrating over past values. This is a coarse approximation because the A and B maps are measured responses, not the fields before the material, but it is a good starting point. We will consider three models:

1. $\mathrm{NL}_{\mathrm{DFG/SFG}} \propto A \cdot B,$ (1.10)
2. $\mathrm{NL}_{\mathrm{SHG/OR}} \propto A^2 + B^2,$ (1.11)
3. $\mathrm{NL}_{\mathrm{Over\text{-}Rot.}} \propto \sin(A + B) - \sin(A) - \sin(B),$ (1.12)

which represent difference frequency generation (DFG)/sum-frequency generation (SFG), second harmonic generation (SHG)/optical rectification (OR), and 'over-rotation', respectively. The first two models are nonlinear products resulting from the expansion:

$$(A + B)^2 = A^2 + B^2 + 2A \cdot B, \tag{1.13}$$

which is proportional to the second order polarization Eqn. (1.8). As demonstrated in Eqn. (1.4), we expect that the A^2 and B^2 terms, which both contain SHG and OR products, will be re-

moved by the differential measurement. In contrast, the cross term $2A \cdot B$, which contains both SFG and DFG products, should remain. Importantly, the A and B fields are real-valued, allowing multiple products to be contained in a single term (see Note 1.2).

The third model is proportional to a nonlinearity commonly called 'over-rotation' [3] that is inherent in the technique used to measure the THz fields in ZnTe, as discussed further in Sections 2.4 and 4.1. The detection response function is sinusoidal and the nonlinear portion, $\mathrm{NL}_{\text{Over-Rot.}}$, is found by preforming the differential measurement numerically.

Note 1.2 A and B are real-valued

As a reminder, the fields $A = E_A(t)$ and $B = E_B(t)$ are *real*-valued, and therefore can be decomposed into a pair of complex-conjugates that effectively contain both positive and negative frequency components. For example, if A and B were single-frequency plane-waves, then the decomposition would be identical to Eqns. (1.5) and (1.6). However, A and B are in actuality pulses containing a broad spectrum of component frequencies. Thus, the terms A^2, B^2 and $2A{\cdot}B$ are composed of a vast number of products between the complex amplitudes associated with each frequency: $\mathcal{E}_A\mathcal{E}_A$, $\mathcal{E}_A\mathcal{E}_A^*$, $\mathcal{E}_B\mathcal{E}_B$, $\mathcal{E}_B\mathcal{E}_B^*$, $\mathcal{E}_A\mathcal{E}_B$, $\mathcal{E}_A\mathcal{E}_B^*$ and $\mathcal{E}_A^*\mathcal{E}_B$.

The models are shown in Fig. 1.10, alongside the measured NL signal in the left column. The DFG/SFG model accurately reproduces the four corners of the parallelogram pattern observed in the measured NL signal. In contrast, the SHG/OR model is not well represented in the data. The high-frequency SHG components are narrow lines falling in regions where there is only noise in the NL signal (as predicted in the vector diagram overlay shown in Fig. 1.9). Furthermore, the low-frequency OR components appear as two narrow lines intersecting at $[0, 0]$ THz, while the measured data has a small parallelogram or dot feature. However, this latter feature and the 'four leaf clover' pattern are well accounted for by the over-rotation model.

In the right-most column of Fig. 1.10, we have naively taken a weighted sum of the SFG/DFG and over-rotation models to produce a fairly convincing analog of the measured NL signal. However, it is important to be aware that these maps simply show the products of fields—the order in which these products occur has yet to be determined. In the next section, we will discuss the questions that remain.

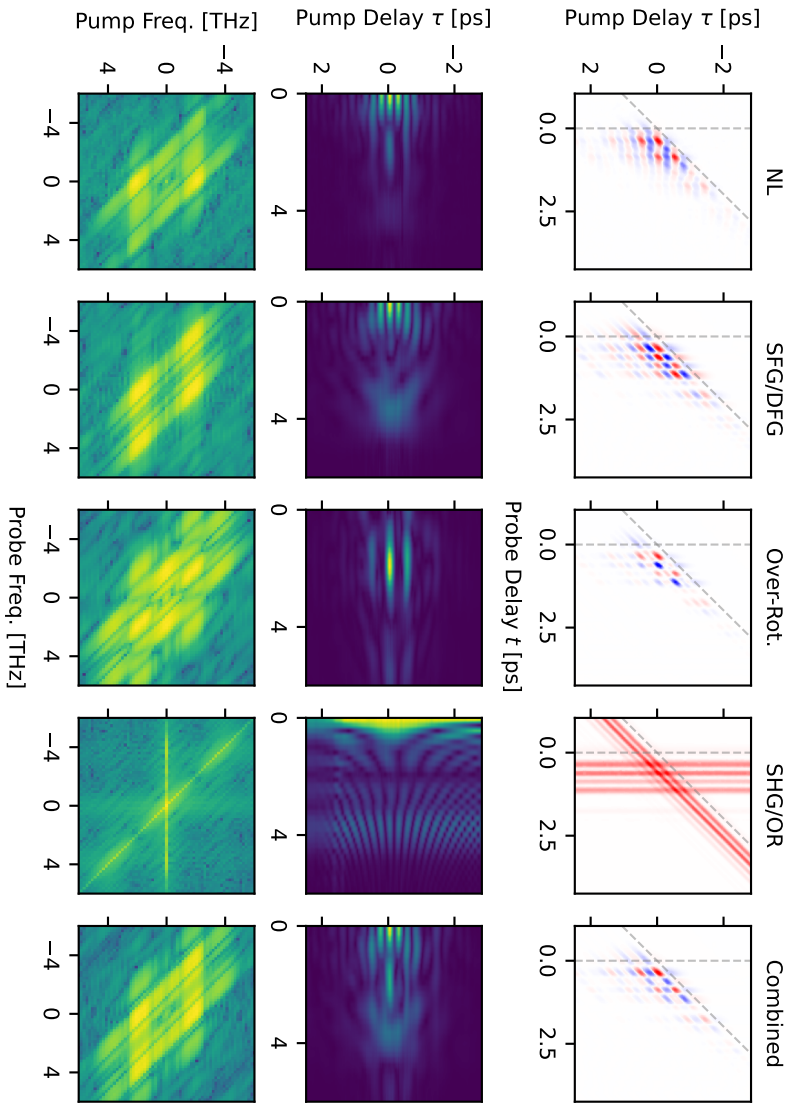

Figure 1.10. Simple instantaneous nonlinearity models. Columns left to right: measured nonlinear signal (NL); sum/difference frequency generation (SFG/DFG); over rotation (Over-Rot.); second harmonic generation and optical rectification (SHG/OR); weighted sum of the SFG/DFG and over-rotation models (Combination). Characteristics of the SHG/OR model are not found in the data, as predicted in the vector diagram overlay shown in Fig.1.9. The combined model captures many of the features present in the measured nonlinear signal.

1.7 Outstanding Issues

There are, however, a few issues with what we have discussed so far. Firstly, we are not directly measuring the THz pump fields, we are measuring the *optical* probe. This will be discussed further in the coming chapters. For now, know that the THz fields, $E_{A/B}$, slightly modify the optical probe field, E_{pr}, through a second-order nonlinear process generating a polarization like the following [19]:

$$P(\omega_{\mathrm{pr}}+\Omega)=\epsilon_0\chi^{(2)}E_{A/B}(\Omega)E_{\mathrm{pr}}(\omega_{\mathrm{pr}}) \quad \rightarrow \quad E'_{\mathrm{pr}}(\omega_{\mathrm{pr}}+\Omega), \tag{1.14}$$

which radiates a new field component $E'_{\mathrm{pr}}(\omega_{\mathrm{pr}}+\Omega)$, where ω_{pr} and Ω are optical and THz angular frequencies respectively. Critically, $E_{A/B}(\Omega)$ represents only *one* of the positive or negative frequency components in the fields $A=E_A(t)$ or $B=E_B(t)$. To get a product of the fields, $A\cdot B$, we need at least a third-order *direct* process, or two *cascaded* second-order processes. For example:

$$\text{Direct:} \quad P=\epsilon_0\chi^{(3)}E_AE_BE_{\mathrm{pr}} \tag{1.15}$$

$$\text{Cascaded:} \quad P=\epsilon_0\chi^{(2)}\underbrace{\left[\chi^{(2)}E_AE_B\right]}_{\text{Reradiated}}E_{\mathrm{pr}}. \tag{1.16}$$

These two processes are quite different beasts. In the direct process, we immediately generate a new optical probe field that only differs in frequency from its parent by a few THz. To put that in perspective, the center frequency of the $800\,\mathrm{nm}$ probe is $375\,\mathrm{THz}$. In contrast, the first step of the cascaded process is an interaction between the two THz fields, wherein new fields at either the sum or difference of their frequencies are generated—a very large deviation. The second step then 'reads-out' the newly generated components with a small modulation of the optical probe, as in the direct process. Vector diagrams and the instantaneous models cannot determine if either the direct or cascaded process occur, and/or whether they both happen simultaneously.

There is a similar degree of uncertainly within the vector diagrams themselves. As shown by Kuehn et al. [34, Fig.1], there can be multiple Louisville pathways to the same spot in the map. In Fig. 1.11(a), we have illustrated two such paths to the positive SFG feature. As one can imagine, the number of paths grows rapidly with the number of fields involved.

Moreover, all spots on the diagram are invariant to products of complex conjugates, such as $\mathcal{E}_B\mathcal{E}_B^*$ and $\mathcal{E}_A\mathcal{E}_A^*$. For instance, in Fig. 1.11(b) the positive over-rotation feature could be reached with a single $\mathcal{E}_A$ vector, but we know that is unlikely for two reasons: firstly, in the NL map of Fig. 1.7 the feature is a parallelogram-shaped spot, whereas the A map has only a narrow diagonal line; secondly, the differential measurement should eliminate single-pulse features. If we expand our over-rotation model to third-order, a good hypothesis emerges. Since $\sin(x)\simeq x-x^3/6$, Eqn. (1.12) becomes

$$\mathrm{NL}_{\text{Over-Rot.}}\propto -\frac{A^2\cdot B}{2}-\frac{A\cdot B^2}{2}. \tag{1.17}$$

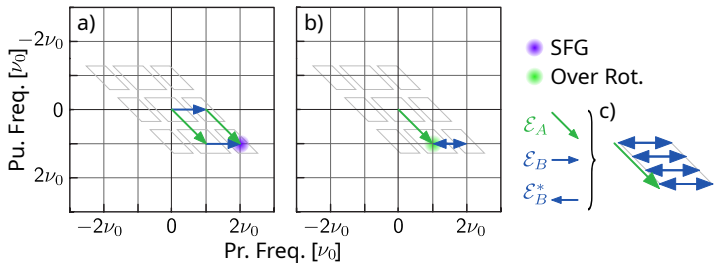

Figure 1.11. Examples showing non-uniqueness of the vector diagrams. (a) Two Louisville pathways to the same point. (b) A third-order path to a first-order location. Products of complex conjugates, such as $\mathcal{E}_B\mathcal{E}_B^*$, cancel in the vector diagram. SFG, sum-frequency generation; Over Rot. over-rotation. (c) The parallelogram-shaped features result from the addition of many different frequency vectors.

Both terms are cross-products of A and B, which are what we would expect to measure. The last term contains one factor of A, and two of B (importantly an even number). If we expand this latter term considering just the central frequency component ν_0, one of the products is proportional to $\mathcal{E}_A\mathcal{E}_B\mathcal{E}_B^*$. As illustrated in Fig. 1.11(b), the product $\mathcal{E}_B\mathcal{E}_B^*$ is just a hop away-and-back to the same spot at the end of the $\mathcal{E}_A$ vector. In the vector diagram, $\mathcal{E}_B\mathcal{E}_B^*$ does nothing. However, since our fields have a broad bandwidth around ν_0, different frequency components—with different length vectors—mix to create the parallelogram shaped spot. A schematic of the concept is sketched in Fig. 1.11(c). What we have described is in fact nothing more than the convolution theorem of the Fourier transform [8, p.115]. In the time-domain we have the product of multiple fields, therefore, in the frequency-domain we have their convolution.

1.8 Moving Forward

It is at this point that we delve into the core research of this thesis. We have a general understanding of how to interpret the 2D THz datasets we will be working with, and two useful tools for analyzing the physical processes behind them. However, as discussed, these tools have their limitations. While vector diagrams provide valuable information about possible Louisville pathways and the *net* number of A and B fields involved in the nonlinear processes, they do not reveal the order in which the fields are combined. The question of whether these processes are direct or cascaded remains unanswered. Additionally, from a practical perspective, vector diagrams are limited to representing only a single frequency component from each pulse. To address this, we created several simple instantaneous models incorporating the broad bandwidth of the pulses involved, but similarly, these fail to reveal the sequence of the underlying processes. Moreover, both the vector diagrams and instantaneous models do not account for dispersion and loss, which significantly affect the propagation and interactions between the THz pump pulses, as well as their simultaneous detection with the optical probe.

To overcome these limitations and gain a more comprehensive understanding of the investigated nonlinear effects, the subsequent chapters will explore an experimental approach combined with numerical pulse propagation methods. Our focus will be on discriminating direct and cascaded nonlinear processes in ZnTe. The experiment has two parts: in the first, a $\langle 100 \rangle$-cut ZnTe crystal is used to effectively disable second-order ($\chi^{(2)}$) processes for all field polarizations, regardless of cascading. This will serve as a reference for the signature of third-order ($\chi^{(3)}$) processes alone. In the second part, a $\langle 110 \rangle$-cut ZnTe crystal is oriented in a way that second-order processes can only occur by cascading through a primary third-order process.

The numerical methods enable us to corroborate the measured influence of the second- and third-order processes by selectively turning them on or off, allowing us to observe their individual contributions. Equally important is the ability to isolate the nonlinear interactions between the THz pumps from those between the pumps and the probe. Unlike the instantaneous models, these pulse propagation simulations incorporate dispersion and loss, which have a major influence at THz frequencies in ZnTe. They also allow second- and third-order processes to occur sequentially along the length of the crystal.

Before exploring these results, the following chapters will also provide a detailed account of the design and implementation of the instrumentation used to measure the 2D maps. This will ensure a complete understanding of the experimental setup and the reliability of the obtained data.

By combining experimental measurements, numerical simulations, and theoretical analysis, we aim to gain a comprehensive understanding of the complex nonlinear phenomena at play in our system. The subsequent chapters will build upon the foundations established in this introductory chapter, providing deeper insights into the intricate interplay between direct and cascaded processes, the effects of dispersion and loss, and the interpretation of the acquired 2D maps.

CHAPTER 2
Instrumentation

In this chapter, we provide a comprehensive guide for constructing the 2D THz instrument. We begin with an overview of the optical layout and its components, along with some useful tips and tricks for alignment. Next, we delve into the detection method used to measure the response of our sample, namely polarimetry. We detail the implementation of polarimetry, which is technically equivalent to the methods employed in electro-optic (EO) detection and THz-Raman spectroscopy. We also explain our rationale for choosing polarimetry in this particular context.

Subsequently, we discuss the implementation of the differential measurement technique introduced in Section 1.3 for isolating the nonlinear components of the signal. In particular, we cover the timing system that allows us to acquire the A, B, and AB maps in a nearly parallel manner while suppressing background noise.

Finally, we conclude the chapter by benchmarking the system to quantify several performance metrics, and to ensure the instrument is operating as expected.

2.1 Optical Layout

With reference to Figure 2.1, we will start at the laser amplifier in panel (a), stepping through the components sequentially in the direction of propagation. The source laser for our setup is a "Solstice Ace" Ti:sapphire regenerative amplifier from Spectra-Physics. It is a typical table-top source centered at $800\,\mathrm{nm}$, with $1\,\mathrm{kHz}$ repetition rate, and a $4.7\,\mathrm{mJ}$ pulse energy. Further output characteristics can be found in Table 2.1. The output of the laser amplifier is fed to a custom "HE TOPAS" optical parametric amplifier (OPA) from Light Conversion, which consists of a standard "TOPAS C" OPA—used as a seed/preamplifier—and the final amplification stage of a standard HE TOPAS. For a fundamental review of optical parametric amplification, see Boyd [7, sec. 1.2.5 and sec. 2.8]. The output wavelength of the OPA is set to $1500\,\mathrm{nm}$, at which the pulse energy after the wavelength-separator (WLS) is typically $850\,\mu\mathrm{J}$. The depleted $800\,\mathrm{nm}$ pump light from the last amplification stage in the OPA is sampled with a fused silica wedged (W) and repurposed as a probe. In Section 2.3 we discuss the OPA and using the depleted pump light as a probe in more detail. Here, at the output of the OPA, the $1500\,\mathrm{nm}$ pump and $800\,\mathrm{nm}$ probe diverge. We will examine the pump path first, then return to trace the probe path.

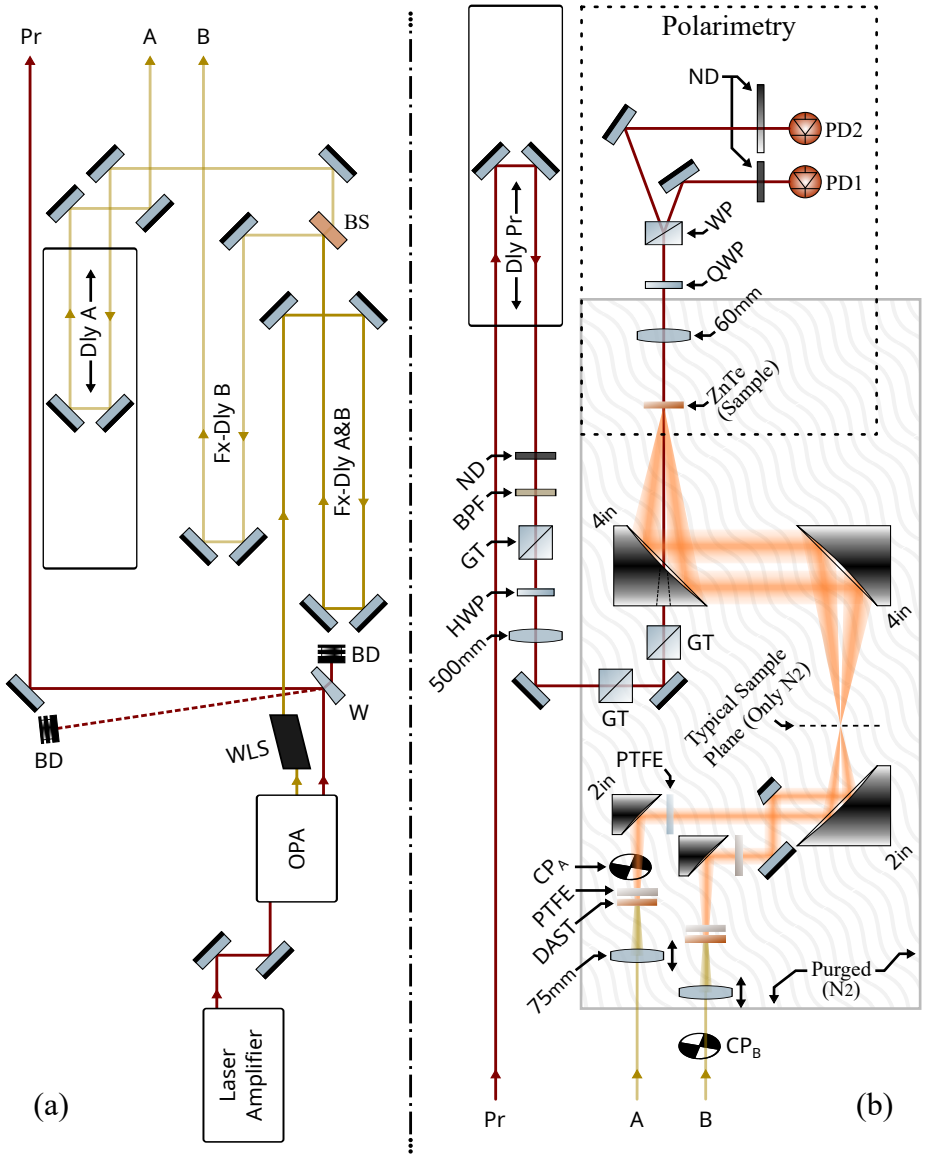

Figure 2.1. Schematic of the 2D THz instrument. (a) Shows the 800 nm probe (red) and 1500 nm pump (yellow) beam routing after the OPA and leading up to the second section in (b). (b) The 800 nm probe is conditioned (amplitude, spectral content, polarization), and the 1500 nm pump is converted to THz (in a purged environment). The 800 nm probe and THz pump are overlapped on the ZnTe sample. The interaction between pump and probe in ZnTe is measured with polarimetry. Component abbreviations: OPA, optical parametric amplifier; WLS, wavelength separator; W, wedge; BD, beam dump; Fx-Dly, fixed delay; BS, beam splitter; BPF, band pass filter; CP, chopper; DAST, 4-N, N-dimethylamino-4′-N'-methyl-stilbazolium tosylate; PTFE, Polytetrafluoroethylene; ZnTe, zinc telluride; N2, nitrogen; HWP, half-wave plate; QWP, quarter-wave plate; GT, Glan-Taylor polarizer; WP, Wollaston polarizer; ND, neutral density filter; PD, photo diode.

Table 2.1. Typical output characteristics of our Solstice Ace laser amplifier.

Parameter	Value
Pulse Width	90 – 100 fs
Repetition Rate	1 kHz
Average Power	4.7 W
Pulse Energy	4.7 mJ
Pre-Pulse Contrast Ratio[1]	1000:1
Post-Pulse Contrast Ratio[1]	100:1
Operating Temperature Range[1]	±5°C
Energy Stability[1]	<0.5% rms over 24 hours
Beam Pointing Stability[1]	<5 µrad (rms)7
Wavelength	780–820 nm
Spatial Mode[1]	TEM00 (M2 <1.25, both axes)
Beam Diameter (1/e²)	10-11 mm (nominal)
Polarization	Linear, Horizontal

[1] Factory specifications, see details at `https://www.spectra-physics.com/en/f/solstice-ace-ultrafast-amplifier`.

2.1.1 Pump Path

The wavelength-separator (WLS) separates the OPA signal from the idler, the latter of which is internally dumped. The beam passes through a fixed delay line (Fx-Dly A&B) to compensate for the extra length of the probe path, then is split by the 50:50 beamsplitter (BS; Thorlabs BSW12) for the separate 'A' and 'B' THz generation stages. The B path-length is fixed, but offset (Fx-Dly B) so that the A and B path lengths are equal when the motorized stage in the A delay line (Dly A) is at the center of its range.

Continuing on panel (b), the A and B pump beams enter a sealed acrylic box purged with nitrogen (N_2) to displace water-vapor-laden ambient air. The extent of the purge-box is indicated by the gray hatched box in panel (b). Both the A and B THz generation stages and the full extent of the THz beam path are housed in the purge-box. We use two separate but identical THz generation stages to avoid nonlinear interactions between the two $1500\,\mathrm{nm}$ pump pulses that could otherwise occur if they were temporally coincident in a single 4-N, N-dimethylamino-4′-N'-methyl-stilbazolium tosylate (DAST) crystal. Using two crystals results in dissimilarities between the two THz pulses, however, due to the field-resolved nature of the studies performed herein, it is straight forward to characterize each pulse and account for the differences in later modeling.

As described in more detail in Section 2.6.1, we loosely focus the $1500\,\mathrm{nm}$ pump pulses on the DAST crystals with $75\,\mathrm{mm}$ lenses such that the full $5\,\mathrm{mm}$ aperture of the crystal produces a visible emission. This emission is presumed to be the second harmonic of the $1500\,\mathrm{nm}$ pump, given its reddish color and strong correlation to the intensity of the THz field that is generated by the twin process optical rectification (OR; see Note 2.1).

If we conservatively estimate that $99\,\%$ of the pump intensity falls within the $5\,\mathrm{mm}$ aperture, then the $1/e^2$ and 'top-hat' diameters are $3.2\,\mathrm{mm}$ and $2.3\,\mathrm{mm}$ respectively [53, p.665]. The latter value yields an average fluence of $10.6\,\mathrm{mJ/cm^2}$ for a pump pulse energy of $450\,\mu\mathrm{J}$. This upper-bound on the fluence just crosses the $10\,\mathrm{mJ/cm^2}$ threshold where degradation of the transparency [21] and ablation [17] in DAST have been observed.

Note 2.1 Intra-pulse difference frequency generation

THz generation in nonlinear crystals is commonly referred to as 'optical rectification' for the sake of simplicity. However, a more accurate description of the process is intra-pulse difference frequency generation. This perspective emphasizes the fact that short pulses possess a wide spectral bandwidth, and the components within that bandwidth intermix to produce a diverse range of THz frequencies [10, 46].

Because optical rectification is a coherent process [4], the THz field will initially inherit the wavefront curvature of the pump field and also come to a focus after the $75\,\mathrm{mm}$ lens. However, due to the frequency dependence of diffraction, the focal position will be somewhat shifted. To account for this, the $75\,\mathrm{mm}$ lenses are placed on translation stages so that the divergence of the THz beams can be optimized [49]. Afterwards, the THz beams are collimated with $2\,\mathrm{in}$ focal length, $1\,\mathrm{in}$ diameter off-axis parabolic mirrors (OAPs). The $99\,\%$-transmission beam diameters are approximately $(10 \pm 2)\,\mathrm{mm}$. The beams are made parallel and equidistant to the 'collimated' axis of a $2\,\mathrm{in}$ focal length, $2\,\mathrm{in}$ diameter OAP that overlaps their foci at the *typical* sample plane. To reduce comatic aberrations, a D-shaped mirror is used to bring the two collimated beams close together before the focusing/combining OAP, such that they are nearly touching. The focus at the (typical) sample plane is then remapped by two $4\,\mathrm{in}$ focal length, $2\,\mathrm{in}$ diameter OAPs onto the ZnTe crystal—ordinarily called the 'detection' crystal, but here it is our *sample*. At this point, the probe pulse is recombined and used for polarimetry, discussed in detail in Section 2.4.

2.1.2 Probe Path

Let us now return to the output of the OPA and consider the path of the probe pulse. An uncoated fused-silica wedge (W) samples the depleted $800\,\mathrm{nm}$ pump from the OPA to be used as the probe. A wedge is the preferred method for taking a few-percent sample of a beam, as we can easily separate the dispersion-free first-surface reflection from the reflection off the back face that passes through the material. In comparison, parallel-surface optics such as absorptive or reflective neutral density (ND) filters would act as etalons producing a series of attenuated echos after the probe pulse that appear as pre-pulses when used for pump-probe measurements. Furthermore, transmission optics—particularly absorptive ND filters—are susceptible to thermal lensing [50] at high average powers.

Notably, it is important that the wedge is not anti-reflective (AR) coated for $800\,\mathrm{nm}$, since we want to enhance, not suppress, the $800\,\mathrm{nm}$ content of the sampled portion of the beam. The refractive index of fused silica is relatively flat across the visible and near-infrared (NIR)

portions of the spectrum [41], so that other by-products of the optical parametric amplification process (such as the second harmonics of the signal and idler) are not preferentially enhanced.

A motorized stage delays the probe with respect to the A and B THz pulses (Dly pr). After the delay stage, a series of optical components condition the probe. The first is an ND filter, which adjusts the maximum amplitude of the probe pulse, and since it is designed for the visible range, also acts as a long-wavelength-pass filter. Further spectral filtering with a $40\,\mathrm{nm}$-wide, $800\,\mathrm{nm}$-centered band-pass filter (BPF; Thorlabs FBH800-40) attenuates by-products of the optical parametric amplification process. The first Glan-Taylor (GT; Thorlabs GT15) polarizer cleans up the probe polarization. The subsequent half-wave plate (HWP) and GT polarizer act as a variable attenuator (see Note 2.2).

Note 2.2 Polarization-based variable attenuator

It is important to remember that a polarization-based attenuator should only be used for fine-tuning the optical power. If used to nearly extinguish the passed light, the signal (pulse) will be severely degraded. Rotating the HWP effectively increases the transmission of orthogonally-polarized light. If the signal is supposedly linearly polarized, then the orthogonal component is noise. Increasing the attenuation therefore decreases the signal-to-noise ratio. Large attenuation factors are best done with a spectrally-flat reflector at a near zero-degree incident angle; for example, the first-surface of a fused silica wedge.

The final GT polarizer is placed right before the through-hole in the OAP that combines the probe and THz beams. Having a polarizer as the last element mitigates the depolarizing effects of scattering in the components before it. However, crystal polarizers like the GT rely on total internal reflection to separate polarization components, and therefore can only tolerate a limited range of input angles. This range is called the field-of-view (FOV), and care must be taken when focusing though the prism to stay within it. The $17.2\,\mathrm{mm}$ hard aperture of the GT polarizer, before the $500\,\mathrm{mm}$ focal length lens, limits the maximum angle of incidence to $0.99\,\mathrm{deg}$, which is just within the FOV of $[\pm 1, \mp 6.5]\,\mathrm{deg}$, where the sign is dependent on the orientation of the polarizer.

After the ZnTe crystal, the probe is recollimated with the $60\,\mathrm{mm}$ lens and (in the absence of any depolarization) made circularly polarized by the quarter-wave plate (QWP). The S- and P-polarized light components are then separated by a Wollaston prism and detected separately on photodiodes PD1 and PD2. The fixed and variable ND filters, before PD1 and PD2 respectively, are used to balance the response of the two photodiodes. One should not use the QWP to balance the photodiodes, but rather find the inflection point in the differential signal between PD1 and PD2 as the QWP is rotated. This point corresponds to the point of maximum circularity on the polarization. Operating away from the point of maximum circularity results in an asymmetric response for positive versus negative phase retardations between the S- and P- polarized components

2.2 Alignment Tips and Tricks

In this section, we will briefly provide a few tips and tricks for aligning the setup. The information is not necessary for understanding the experiment or the results, but could prove useful for more than 2D THz spectroscopy.

2.2.1 Aligning Off-Axis Parabolic Mirrors

Let us start with a reliable procedure for aligning off-axis parabolic mirrors, as illustrated in Fig. 2.2. OAPs are often cursed for being difficult to align, but the key to success is being methodical and eliminating free parameters one at a time. The first step is to mount the OAP at the correct height on a rigid post, as shown in panel (a). We aim to be within $\pm 10\,\mu\mathrm{m}$ of the target beam height. Importantly, if the OAP is mounted in a mirror mount, it should also be fixed on a rectangular base so that later fine-alignment is preserved. The initial coarse alignment of the mirror mount needs to be within the range of the actuators, but the closer the better. Laying the assembly shown in panel (a) down on the optical table with a flat plate under the mirror mount face is a good way to rough-align all the components. For the fine alignment, we use a helium-neon laser (HeNe) that is aligned along a row of holes and leveled at the target beam height, as depicted in panel (b). The beam is expanded to around $25\,\mathrm{mm}$ in diameter. It is important to use optics that do not aberrate the beam in the expander, since we will later use aberrations to identify OAP misalignment. With the reference beam set, the mounted OAP is inserted in the path as shown in panel (c), and the beam is reflected down a perpendicular row of holes. We move iris I2, which was used to level the HeNe beam, and use it as a target. Another iris, I3, is placed along the row of holes near the focus. The goal at this stage is to fix rotation angle R1. We take an iterative approach. First, I1 is closed so that the beam diverges more slowly, and R1 is coarsely adjusted to level the beam over a long distance. Then, with iris I1 open, we translate (T1) the OAP and minimize the coma. Moving a piece of card stock through the focus should reveal a uniformly expanding circular beam. In contrast, a comatic beam crosses the focus at an angle and expands asymmetrically. Next, rotation angles R2 and R3 are adjusted to remove astigmatism, which is seen as an elliptic beam with a major axis that rotates through the focus. The last step of the cycle is to close iris I1 again and adjust T2 and R1 to center the beam through both iris I3 and I2. The cycle is repeated until there is a diminishing return. The last part of the alignment procedure, shown in panel (d), fine-tunes rotation angles R2 and R3, as well as translation T1. A beam profiler is used to closely inspect for astigmatism and coma about the focus. It is mounted on a stage so that it can be precisely moved through the focus. We iteratively sweep across the focus while making small changes to R2, R3, and T1 and monitoring for improvement. Once the beam maintains a circular shape through the focus, this typically corresponds to the smallest achievable spot size. It is prudent to repeat the cycle in panel (c), making slight adjustments to R1 and T2 if the beam is no longer centered on iris I3—if changes are made, one must also repeat the procedure in panel (d). As with all alignment, repeat to exhaustion.

The *ex-situ* alignment just described is repeated for each OAP in the setup. The rectangular bases make it easy to then position the pre-aligned OAPs with respect to each other. As

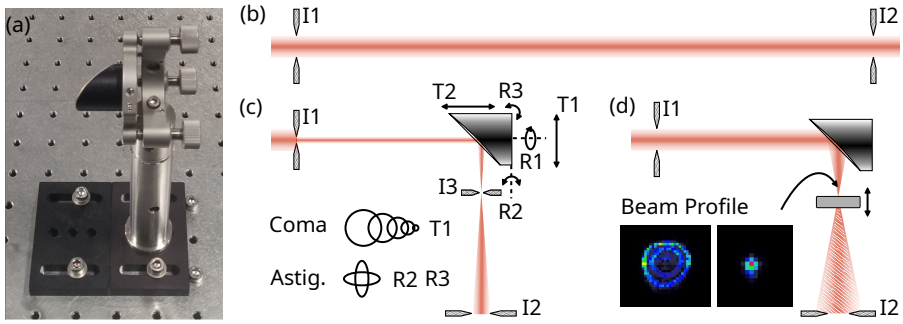

Figure 2.2. *Ex-situ* alignment of off-axis parabolic mirrors. (a) The OAP is mounted on a rectangular base at the correct height ± 10 um (b) The HeNe beam is aligned along a row of table holes and leveled at the correct height with irises I1 and I2. (c) The OAP is inserted in the beam and adjusted to reflect it down a perpendicular row of holes. Translation T1 and rotations R2/R3 are associated with coma and astigmatism, respectively. Translation/rotation T2/R1 only affect the horizontal/vertical pointing. The iris I1 is narrowed to restrict the divergence after the OAP. (d) A beam profiler is placed at the focus of the OAP. Fine alignment of the OAP increases the focused spot circularity and decreases the size. Iris I1 is opened to maximize aberrations. The left and right beam profile insets are examples from the instrument at SLAC. The left inset shows relatively circular diffraction rings from iris I1 just outside the focus. The right inset shows the focused spot—any structure is below the 6.5 x 6.5 um pixel size.

captured in Fig. 2.2 (a), the base is butted up against two M6 screws with carefully matched head sizes. The same screws can be used to re-reference the OAP in another location. In addition, a second base can be butted up against the OAP base and used as a parallel reference for translating the OAP. Typically, we repeat procedure (c) and (d) in Fig. 2.2 for each OAP as they are placed sequentially, but OPAs used for recollimation are more difficult because they do not focus the beam. A procedure like in Fig. 2.2 (c), but for a collimated beam, works well even if one has to use a plane-mirror to divert the beam a few meters to look for coma, astigmatism and collimation (defocus). Another option, if there are space constraints, is a shearing interferometer like the one depicted in Fig. 2.3 (also see Chapter 4 in [40]). The beam is well collimated when the interference fringes are parallel to the inscribed line. Curved fringes indicate aberrations other than defocus, and one can adjust the OPA position to try and correct these errors.

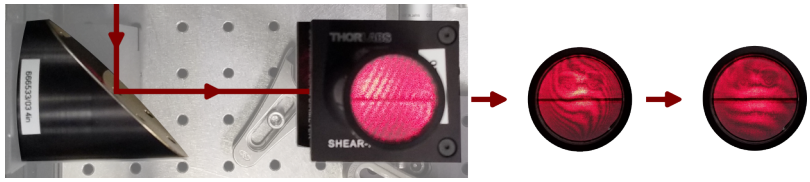

Figure 2.3. Adjusting collimation with a shearing interferometer. The beam is collimated when the interference fringes are parallel to the inscribed line. Curved lines indicate aberrations other than defocus.

2.2.2 Aligning delay stages

There is already a comprehensive guide to aligning optical delay stages from WiredSense [58], we will only add a few suggestions. Much of the work can be eliminated by using a retro-reflector or hollow roof-mirror. A hollow roof-mirror has the advantage that it does not vertically displace the beam (without one easily knowing). However, these components are quite expensive, so we use two right-angle prism mirrors butted against a common flat back surface to make our own hollow roof-mirror, as illustrated in Fig. 2.4 (a). This configuration

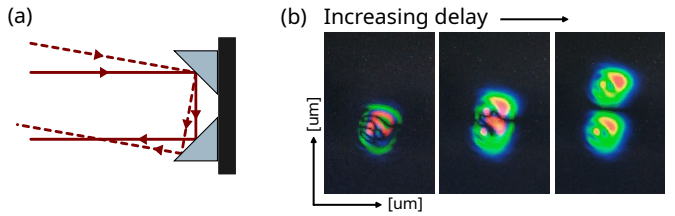

Figure 2.4. Delay stage alignment hints. (a) Using a hollow roof-mirror makes alignment relatively easy, since incoming and outgoing beams are always parallel. (b) Movement of the beam profile with stage displacement. A reference image of the focused beam profile (bottom) is saved, and we see the difference in intensity as the beam walks up (top). When the incoming beam is parallel to the stage, there is no displacement.

also allows us to vary the separation distance of the mirrors. With the mirrors known to be at a right angle to each other, we can assume the incoming and outgoing beams are parallel. Moreover, the alignment is insensitive to a rotation of the assembly in the plane of reflection. Therefore, the only critical adjustment is ensuring the incoming beam is parallel to the stage. We find that placing a beam profiler at a focus after the stage makes this alignment fairly easy. The procedure is as follows:

1. Move the stage to one end.
2. Save a reference image—the bottom beam profile in Fig. 2.4 (b).
3. Move the stage to the other end.
4. Look for a displacement of the beam profile—the top profile in figure Fig. 2.4 (b).
5. Angle the incoming beam in one direction—remember the direction.
6. Save a reference image.
7. Move the stage back to the initial end.
8. If the displacement is larger, angle the incoming beam in the opposite direction, if it is smaller, continue in the same direction.
9. Repeat until the beam profile displacement is negligible.

It may seem obvious, but if one cannot eliminate a vertical displacement of the focused beam profile using this process, then they should make sure the translation stage is mounted to a flat surface. Sometimes a small dent in the table needs to be honed with an oil stone. Furthermore, it may be necessary to evenly (and lightly) torque all the screws mounting the stage to the optical table. Using a torque-wrench would be the ideal solution.

2.3 Optical Parametric Amplifier

To efficiently pump the DAST organic crystals, an optical parametric amplifier (OPA) is used to convert the $800\,\mathrm{nm}$ pulses from the Ti:sapphire amplifier to $1500\,\mathrm{nm}$. Although this is not the optimal wavelength for the intra-pulse difference frequency generation process in DAST, which is around $1450\,\mathrm{nm}$ [30, Fig. 9], it was selected because the OPA is most efficient there. Nonetheless, the spectral bandwidth of the $100\,\mathrm{fs}$ full-width half-maximum (FWHM) pulses is only $0.44/100\,\mathrm{fs} = 4.4\,\mathrm{THz}$ [53, Eqn. 9.13], and within that range, pump wavelengths between $1250\,\mathrm{nm}$ and $1500\,\mathrm{nm}$ have comparable coherence lengths in DAST [30, Fig. 9].

After the last stage of amplification in the OPA, the depleted $800\,\mathrm{nm}$ pump light is repurposed as a probe. By doing this, we maximize the common path between pump and probe, which reduces the impact of pointing drift and vibrational noise. Furthermore, any path length differences due to thermal expansion in the OPA are naturally matched.

However, a detrimental aspect of using the depleted pump light is that fluctuations in the OPA's conversion efficiency are mapped to the probe's intensity. Moreover, the static birefringence of the β barium borate (BBO) crystal used in the final amplification stage of the OPA, as well as the polarization-sensitive nature of phase matching in the parametric amplification process [7, sec. 2.3], lead to a significant decrease in the extinction ratio of the probe polarization after it passes through the crystal. Moreover, poor alignment of the OPA exacerbates the problem, and should be an early suspect if there is a substantial increase in probe intensity and polarization noise between measurements.

In a future design revision, we recommend sampling a small portion of the pump light just before the BBO crystal. To reduce the noise further, one could sample the oscillator output and use some form of active path length compensation. However, the reader is forewarned to ensure that their detection scheme is able to gate-out the requisite probe pulse, which is now separated from its neighbors by just $1/80\,\mathrm{MHz} = 12.5\,\mathrm{ns}$.

2.4 Polarimetry and EO detection

The detection method we employ can broadly be defined as polarimetry. Its implementation is depicted in Fig. 2.5, and its context in the larger 2D THz instrument is indicated with a dashed box in Fig. 2.1. The measured quantity in polarimetry is a polarization modulation of the $800\,\mathrm{nm}$ probe. Before the sample (ZnTe crystal), the $800\,\mathrm{nm}$ probe is linearly polarized. Interactions with the THz pump fields in the sample modulate the probe polarization, inducing ellipticity. The following quarter-wave plate (QWP) biases the polarization such that, in the

absence of a sample or THz-field, the probe polarization would be circular and divided equally into linear S- and P-polarization components by the Wollaston polarizer (WP). However, the slight modulation of the polarization by the sample and THz-field creates an imbalance that is measured as an intensity difference, ΔI, on photodiodes PD1 and PD2. The overall signal measured with polarimetry is a normalized intensity difference or 'modulation' $\Delta S = \Delta I / I_0$, where I_0 is the total probe intensity. To ensure that the intensity difference on the photodiodes is zero in the absence of a THz field, we use a fixed and variable neutral density (ND) filter to balance the intensities with the THz beam blocked. The $60\,\mathrm{mm}$ lens is solely for recollimating the beam, which is focused through the ZnTe sample.

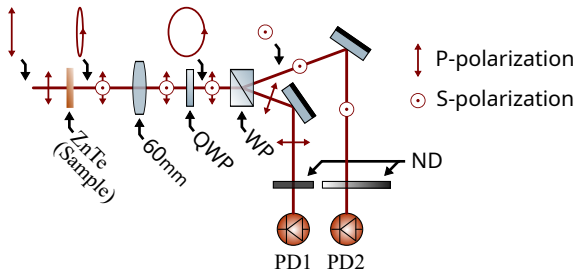

Figure 2.5. Schematic of polarimetric detection. The $800\,\mathrm{nm}$ probe is initially linearly polarized. The polarization is modulated by the sample (ZnTe crystal) and THz pump fields, inducing an ellipticity. A cartoon polarization evolution is drawn at several locations. The quarter-wave plate (QWP) biases the polarization to make it circular in the absence of a sample or THz-field. The Wollaston polarizer (WP) separates circularly polarized light into equal S- and P-polarization components, but the sample and THz-field induce an imbalance. This imbalance is detected as an intensity difference on photodiodes PD1 and PD2. The neutral density (ND) filters are set to balance the intensities with the THz beam blocked. The $60\,\mathrm{mm}$ lens recollimates the beam after passing through the ZnTe sample.

Polarimetry encompasses all sources of polarization modulation, be they inelastic Raman scattering or photon-energy conservative optical mixing processes. The prior source is often used to great success in 2D THz-THz-Raman spectroscopy [32, 38, 42, 52]. However, in our experiment the detected signal is predominantly due to the latter electronic contributions, thus we will nominally call the method used in this thesis 2D THz-THz-polarimetry. To emphasize, THz-THz-Raman spectroscopy and THz-THz-polarimetry are technically identical in their implementation; it is the specificity that distinguishes the two.

It should also be made clear that both THz-THz-Raman spectroscopy and THz-THz-polarimetry are *in-situ* measurements—information about the sample is directly encoded in the optical probe by the THz pump fields. This is in contrast to *ex-situ* THz-transmission spectroscopy [34, 44], where information about the sample is encoded in the THz pump fields and subsequently extracted by the probe with THz-THz-polarimetry in a separate detection crystal. In the context of THz-transmission spectroscopy, the latter stage of THz-THz-polarimetry in a detection crystal is called 'electro-optic (EO) detection'. EO detection is typically considered to be linearly proportional to the THz field strength in the low-field limit [2, 45] and, therefore, any measured nonlinearities should be due to the sample, not the detection. As can be seen in Fig. 2.1, our instrument was designed for THz-transmission spectroscopy (based

on [34]). The typical sample plane is indicated at the first intermediate focus of the THz beams, and the detection plane is at the final focus where the ZnTe crystal is located. Given the design of our instrument, why have we called the ZnTe crystal the *'sample'*? Well, it soon became clear that outside the small-field limit, there are a wide variety of nonlinear processes occurring in the ZnTe detection crystal that are worth investigating in themselves. This realization is the basis of Chapter 4. For now, we will continue to focus on the instrumentation in a material-agnostic fashion.

2.5 Chopping and Timing

As discussed in Section 1.3, we use a differential measurement technique to extract the nonlinear signal, 'NL'. This involves recording the response for the individual application of the THz pump pulses—referred to as 'A' and 'B'— and their simultaneous application, 'AB'. In addition, we record a null response, 'N', that is used for removing background noise. In implementing this technique, we aim to maximize the data acquisition speed and improve the statistical accuracy of our measurements by utilizing every laser pulse effectively. To achieve this, we employ a chopping scheme that generates a cyclic permutation of the sequence [AB, A, B, N]. To reduce common-mode noise, it is crucial to record the A, B, AB, and N data points sequentially for each delay position in the 2D maps.

The positions of the choppers in the instrument are indicated in Fig. 2.1. Chopper $\mathrm{CP_B}$ operates at half the laser repetition rate ($f_r/2$), while $\mathrm{CP_A}$ operates at a quarter of the repetition rate ($f_r/4$). A timing diagram showing the open and closed windows of the chopper blades is provided in Fig. 2.6. The master clock is a trigger signal from the laser amplifier synchronized to the repetition rate, f_r. From f_r, we derive the 'DELAY' signal that is shifted by half the repetition period, $500\,\mu$s. Chopper $\mathrm{CP_B}$ is synchronized to the rising edge of the DELAY signal, and chopper $\mathrm{CP_A}$ is synchronized to the rising edge of the phase-locked-loop (PLL) output from $\mathrm{CP_B}$. By synchronizing $\mathrm{CP_A}$ to $\mathrm{CP_B}$, instead of directly to the DELAY signal, we eliminate any ambiguity regarding which rising edge to synchronize to. This ensures that we consistently maintain a cyclic permutation of [AB, A, B, N], and avoid permutations of [A, AB, N, B].

To determine our position in the cyclic sequence [AB, A, B, N], we utilize an AND gate to generate an index pulse from the PLL outputs of $\mathrm{CP_B}$ and $\mathrm{CP_A}$. This index pulse is set to a high state when both the A and B pulses are unblocked— *i.e.* the AB pulse. By monitoring this index, we can precisely determine our position in the sequence and assign measurements to the correct map.

The timing system was designed to mitigate errors due to asynchronous jitter in the PLLs of the choppers (approximately $4\,\mu$s). This jitter leads to overlaps between the falling edge of $\mathrm{CP_A}$ and the rising edge of $\mathrm{CP_B}$, creating short glitches ($< 8\,\mu$s) in the AND signal. However, we sync the choppers to the DELAY signal instead of directly to the laser trigger signal f_r. The rising edge of the DELAY signal is shifted 500 µs after the rising edge of the trigger signal, ensuring that the trigger signal is centrally positioned between the rising edges of the DELAY signal. By doing so, we push the glitches far outside the measurement window,

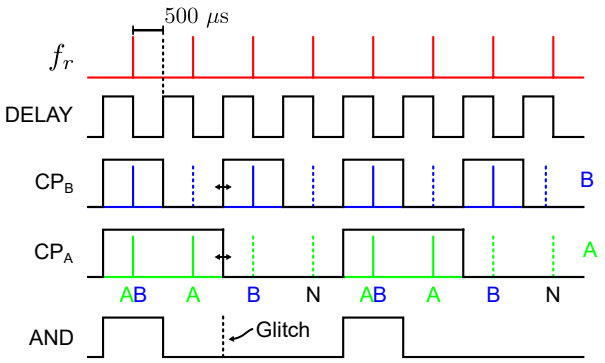

Figure 2.6. Long

which is only 20 μs after the rising edge of the trigger signal f_r. To be clear, the integrating photodetector (IPD4B) used for the measurement is directly triggered by the laser at f_r to minimize jitter.

The timing system is shown schematically in Fig. 2.7. So far, we have discussed the timing signals generated synchronously from the laser amplifier trigger signal f_r. Those are the DELAY, PLL $f_r/2$, PLL $f_r/4$ and AND signals. In addition, there is an asynchronous 'GATE' signal generated by a data acquisition (DAQ) device (NI USB-6008) controlled by the instrument driver running on our computer. When the gate signal is pulled LOW, the trigger signal to the IPD4B is blocked and it stops integrating pulses. The GATE signal is pulled low while the delay stages are moving and settling. Once we are ready to acquire data, the GATE is opened, the requested number of pulses are integrated, and the GATE is closed again. The asynchronicity of this process requires us to record the AND signal along with each integrated pulse, that way we can correctly index the pulses to the cyclic [AB, A, B, N] sequence. We also discard the first reading, since the rising edge of the GATE can cause a glitch.

To ensure the AND index pulse corresponds to the optical AB pulse and that the optical pulses are not physically clipped by the chopper, we adjust the mechanical phase of the choppers accordingly. The method is described in the next section.

2.5.1 Chopper phasing

Artificial nonlinear signals can result from the chopper being out of phase, or only partially blocking the pump beam. To prevent these issues, it is important to center the beam in the aperture of the chopping wheel and verify the beam is smaller than the openings in the blade. Placing the chopper at a focus of the beam is the optimal configuration, as it increases the margin for error in setting the phase of the chopper.

To adjust the phase, we remove the organic crystals and place a photodiode where the pump beams are both focused. It is important to focus onto the photo diode so that the entire pump beam profile is integrated. In fact, here we are most interested in the outer edge of the

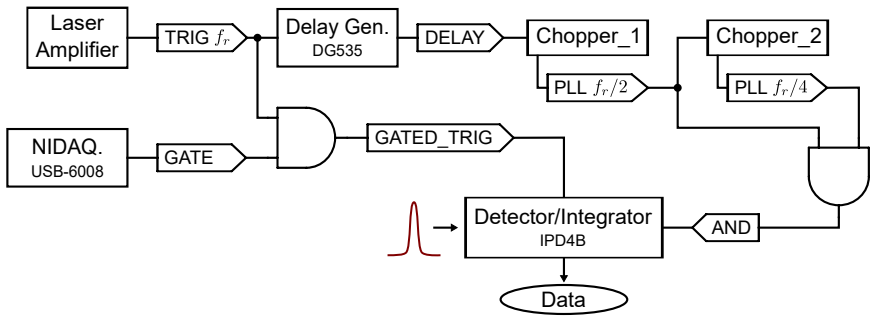

Figure 2.7. Long

beam profile where it could be partially clipped by the chopper. One must be certain that the focused beam is well within the active area of the photodiode, or risk returning a false-negative for clipping. The photodiode signal is monitored on an oscilloscope along with the timing index ('AND') pulse that is used as a trigger. The chopper phase is coarsely adjusted so that the AB index mark is aligned with the AB photodiode pulse, which is followed by the A photodiode pulse, as shown in the timing diagram (Fig. 2.6). The A and B beam paths are alternately blocked to identify the pulses in the sequence. The B beam is then blocked and the phase of the $\mathrm{CP_A}$ chopper is adjusted in one direction until the onset of signal leakage into the B or N photodiode bins—the phase value is noted. The adjustment is repeated in the opposite direction to find the other window-edge. The phase between these two edge-values centers the A beam in the chopper window. The same procedure is repeated for the B pulse with the A pulse blocked—now monitoring the A and N photodiode bins. Following this procedure, any residual signal in the N photodiode bin indicates one or both of the pump beam diameters is too large.

2.6 Benchmarking

In this section, we quantify several performance metrics and provide the results of a few basic tests to confirm that the instrument is operating as expected.

2.6.1 THz power measurement

To measure the THz power of the 'A' pump pulse, we pumped the DAST crystal at $1500\,\mathrm{nm}$, an average power of $185\,\mathrm{mW}$, and a repetition rate of $500\,\mathrm{Hz}$ (the repetition rate of the laser amplifier was $1\,\mathrm{kHz}$, but we chopped the beam at $500\,\mathrm{Hz}$ to reduce the average power). The pump pulse energy is therefore $185/500\mathrm{mJ} = 370\,\mu\mathrm{J}$. Additionally, the beam was modulated with another chopper at $25\,\mathrm{Hz}$ as required by the Gentec T-Rad power meter, detector head THz9B-BL-DZ.

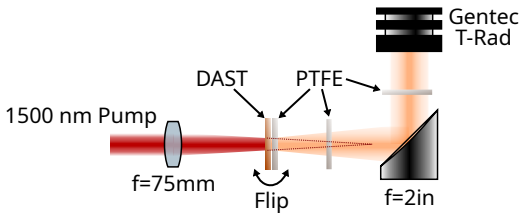

Figure 2.8. Schematic of the THz power measurement. The DAST and PTFE layer are flipped to measure an upper bound approximation for the residual $1500\,\mathrm{nm}$ pump light leaking though the PTFE filters. Component abbreviations: DAST, 4-N, N-dimethylamino-4′-N'-methyl-stilbazolium tosylate; PTFE, Polytetrafluoroethylene.

The DAST crystal is placed well within the $75\,\mathrm{mm}$ focal length of the pump-focusing lens, such that the full $5\,\mathrm{mm}$ aperture of the crystal is filled. The crystal is mounted on the back of a glass substrate, which provides mechanical support and thermal dissipation. The crystal is on the rear face of the substrate so that the emitted THz radiation is not attenuated by the substrate.

Within a few mm of the rear face of the crystal, a $0.1\,\mathrm{mm}$ thick polytetrafluoroethylene (PTFE) diffusing film is placed to scatter and absorb the residual $1500\,\mathrm{nm}$ pump light. A second absorbing/diffusing film is placed a few cm after the crystal, and a third is placed in the collimated beam after the OAP. The PTFE film is more effective as a diffuser than an absorber, therefore, it is important that the first layer of PTFE is close to the crystal to widely disperse the pump light. The subsequent layers of PTFE block the small portion of the now highly divergent residual pump light that is colinear with the THz beam. Increasing the distance and/or adding turns in the THz beam path further decreases the residual pump light.

To measure the amount of residual pump light, we flip the order of the first PTFE layer and DAST crystal. Because absorption of the pump light in PTFE and DAST is predominantly a *linear* process, and THz generation is a *second-order* nonlinear process [30], attenuation of the pump light should be similar, whereas the amount of THz generated should be substan-

tially reduced. In the flipped configuration, the measured residual pump light is $320\,\mu\mathrm{W}$, or only $0.173\,\%$ of the total.

Accounting for the residual pump power, we measure an average THz power of $1.530\,\mathrm{mW}$, which corresponds to a pulse energy of $3.60\,\mu\mathrm{J}$. The efficiency of the generation process is therefore $0.827\,\%$. The measured values are summarized in Table 2.2. We have not measured the power of the 'B' pulse, but based on the polarimetric/EO response, it is of the same order of magnitude.

Table 2.2. THz power measurement results.

Parameter	Value	Note
Pump Parameters		
Wavelength	$1500\,\mathrm{nm}$	
Rep-rate	$500\,\mathrm{Hz}$	Laser-rep $1\,\mathrm{kHz}$, chopped
Gentech mod.	$25\,\mathrm{Hz}$	Not sync'd to laser
Avg. power	$185\,\mathrm{mW}$	
Pulse energy	$185/500\,\mathrm{mJ} = 370\,\mu\mathrm{J}$	
Residual power	$320\,\mu\mathrm{W}$	Flipped crystal mount
Residual energy	$320/500\,\mathrm{uJ} = 370\,\mathrm{nJ}$	
THz Parameters		
Avg. power	$1.530\,\mathrm{mW}$	Pump residual subtracted
Pulse energy	$1.53/500\,\mathrm{mJ} = 3.60\,\mu\mathrm{J}$	
Generation Efficiency		
Efficiency	$3.06/370 * 100 = 0.827\,\%$	

2.6.2 THz Spectrum Measurement

In Fig. 2.9 we provide a measurement of the THz 'A' pulse's temporal waveform (a) and its spectrum (b). Two measurements were taken sequentially with a few minutes of waiting time between, as the enclosure was being purged with dry nitrogen to remove atmospheric water vapor. The absorption lines of water vapor serve as a useful ruler for ensuring the spectrum has been scaled correctly. At the bottom of panel (b), are the absorption lines for water calculated by Peter Uhd Jepsen [9, Chapter 6] from the HITRAN database [22]. We see a good agreement between the peak positions of the measured/calculated absorption dips/peaks, respectively. The system has a maximum dynamic- and spectral-range of around $40\,\mathrm{dB}$ and $8\,\mathrm{THz}$ respectively.

2.6.3 Polarimetry Probe-Intensity Dependence

The modulation signal measured with polarimetry, $\Delta S = \Delta I / I_0$ (Section 2.4), should be independent of the total probe intensity, I_0, based on the assumptions made in this thesis. In

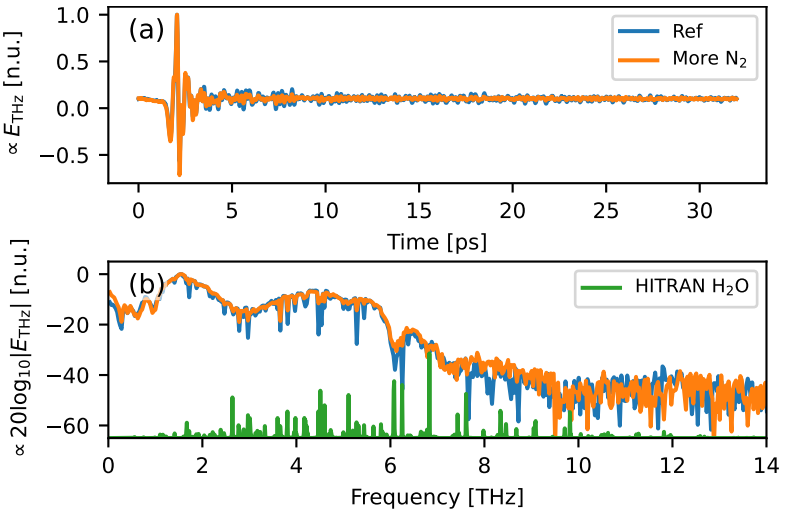

Figure 2.9. Temporal waveform (a) and spectrum (b) of the THz 'A' pump pulse on a good day. The system has a maximum dynamic- and spectral-range of around 40 dB and 8 THz respectively. The absorption lines of water, calculated by Peter Uhd Jepsen [9, Chapter 6] from the HITRAN database [22], serve as a useful ruler in (b).

Section 4.1 we will explore this property from the perspective of the small-field approximation for electro-optic detection [45]. It can also be inferred through inspection of the nonlinear polarization terms in Section 3.2.1 that generate ΔI. These terms are all linear in the probe field, and thus the *normalized* modulation ΔS should be independent of the probe intensity.

To determine the validity of our assumptions, we performed the same polarimetric measurement (EO detection) at several probe powers while holding all other parameters constant. Since we do not change the focused spot size of the probe in the ZnTe crystal, we assume the probe intensity is linearly proportional to the probe power. The probe intensities on photodiodes PD1 and PD2 (Fig. 2.5; components of the Wieserlabs WL-IPD4B boxcar photodiode integrator) are kept constant with a variable ND filter after the Wollaston polarizer; by doing so, we eliminate possible nonlinearities in the detection. To be clear, in these measurements we are determining the effect of varying the probe intensity on the ZnTe crystal, not on the photodiodes. The complementary measurement will be discussed in Section 2.6.4. Note, however, that for the two lowest probe powers we were unable to maintain the same intensity on the photodiodes, as can be seen in the sum of the PD1 and PD2 intensities, I_0, in Fig. 2.10 (a). This deviation is also apparent in panel (b), where otherwise the intensity difference between PD1 and PD2, ΔI, is relatively constant with probe power. In Panel (c) the intensity differences are normalized by the sums to calculate the modulation, ΔS. Normalization greatly reduces the degree to which the waveforms measured at a lower I_0 deviate from the others. However, there still appears to be a small shift in the modulation amplitude with probe intensity. To better view the trend, we have extracted the peak modulation value at two maxima in the THz waveform. The peak values are plotted in panel (c), and fit with a line. In the

fit, we have excluded the peaks for the waveforms where I_0 was significantly lower. For both maxima in the waveform, the modulation depth decreases with probe power. While we have not investigated the cause of this decrease, one possible explanation is a corresponding increase in free-carrier concentration through two-photon absorption of the probe [12]. For the higher probe powers, we do see a visible green emission from the ZnTe crystal, and there is strong evidence in the literature that free carriers attenuate the THz field [47, 56]. It is curious, however, that the trend is not clearly quadratic in probe power if it is related to two-photon absorption. In our measurements, we keep the probe power fixed to avoid deviations. We also choose a value at the lower end of the range, $266\,\mu\mathrm{W}$, where there is little visible emission from the ZnTe crystal.

2.6.4 Polarimetry WL-IPD4B-Count Dependence

We repeated the measurements in Section 2.6.3, except the probe power ($\propto$ intensity) was held constant at $540\,\mu\mathrm{W}$ in the ZnTe crystal, but varied on photodiodes PD1 and PD2. The measurements acquired with the Wieserlabs WL-IPD4B boxcar photodiode integrator are plotted in Fig. 2.11. Generally, we find that the photodiodes and boxcar-integration are very linear across the tested range, except perhaps at the lowest intensity. We typically operate with approximately $125 \times 10^3\,\mathrm{counts}$ on each photodiode, or $I_0 = 250 \times 10^3\,\mathrm{counts}$. The maximum integrated count value for each photodiode is $2^{20} \approx 1 \times 10^6\,\mathrm{counts}$.

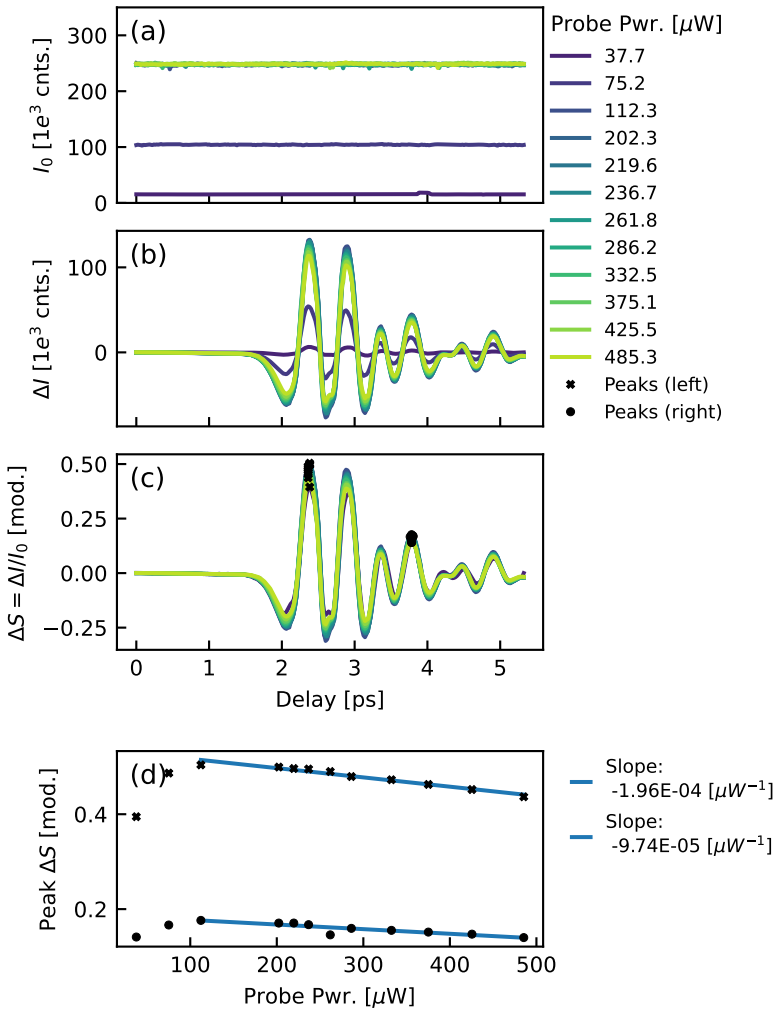

Figure 2.10. Polarimetry probe-power dependence in ZnTe. (a) Sum of the intensities on photodiodes PD1 and PD2 (Fig. 2.5)—*i.e.* the total probe intensity, I_0. A variable neutral density filter is used to maintain a constant value; for the lowest two probe powers, it is not possible. (b) The difference of the intensities on PD1 and PD2, ΔI. Except for the lowest two probe powers, there is only a small amplitude difference between the THz waveforms. (c) The normalized intensity difference $\Delta S = \Delta I/I_0$. Normalization greatly reduces the amplitude deviation for the lowest two probe powers. (d) Peak modulation at two maxima in the THz waveform, fit with a linear trend line. There is a gradual decrease in modulation depth with increasing probe power. This is possibly due to two-photon absorption of the probe and the related free-carrier generation. However, the lack of a clear quadratic dependence in probe power is curious if this is a two-photon process.

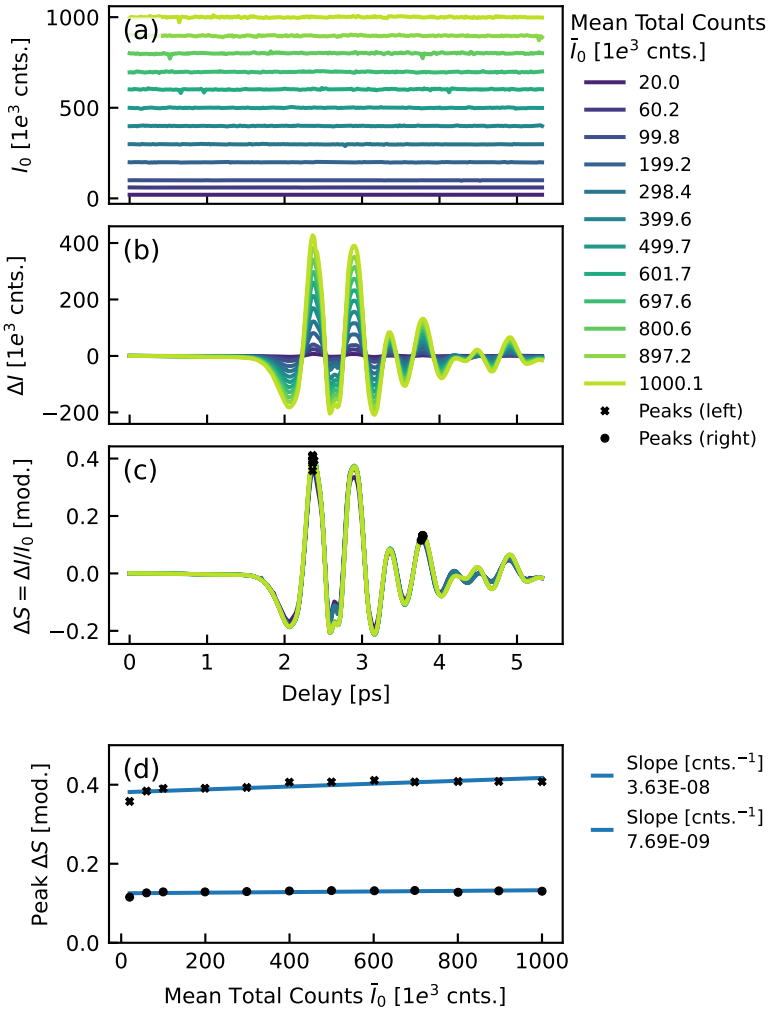

Figure 2.11. Dependence of the polarimetric signal on the total count returned by the WL-IPD4B ($\propto$ intensity on photodiodes PD1 and PD2). (a) Sum of the intensities on photodiodes PD1 and PD2 (Fig. 2.5)—*i.e.* the total probe intensity, I_0. A variable neutral density filter is used to adjust the incident probe intensity. (b) The difference of the intensities on PD1 and PD2, ΔI. (c) The normalized intensity difference $\Delta S = \Delta I / I_0$. (d) Peak modulation at two maxima in the THz waveform, fit with a linear trend line. There is only a very gradual increase in modulation depth with the total number of integrated counts.

CHAPTER 3

Numerical Pulse Propagation

In this chapter, we develop numerical tools that allow us to improve on the predictions of instantaneous models discussed in Section 1.6. Often, the interaction between a THz-frequency field and an optical-frequency probe pulse within non-centrosymmetric crystals (such as ZnTe) is modeled as the 'linear' electro-optic (Pockels) effect. This is a second-order *nonlinear* optical process wherein the quasi static THz field induces a birefringence that modulates the polarization of the probe [45]. For small fields, the birefringence is linearly proportional to the applied THz field strength (see Section 4.1). However, this interpretation does not account for the *non-zero* frequency of the THz fields, and is not easily extended to strong fields or higher order interactions.

A more accurate and extensible picture views the interaction as sum- and difference-frequency mixing between the THz field and optical probe [19]. This is also a second-order nonlinear optical process, but in this case the THz and optical-probe fields, together, induce a nonlinear polarization in the material. Importantly, the induced polarization is not limited to a simple instantaneous product of the fields (producing sum- and difference-frequencies), but also contains higher-order *direct* and *cascaded* products. The great benefit of this picture is that we can leverage decades of research on approaches to simulating these nonlinear optical processes.

In particular, we are guided by the work of Caumes et al. [10], who studied a *"Kerr-like nonlinearity induced via terahertz generation and the electro-optical effect"*. In short, it was shown that an optical pump pulse can generate a co-propagating THz field, which in turn can modulate the polarization of an optical probe pulse through the electro-optic effect. A subsequent experiment demonstrated that cascading can similarly occur between the THz field and the probe alone: the THz field can rotate the probe polarization via the electro-optic effect, such that second-harmonic generation of the probe is no longer symmetry forbidden [15]. As highlighted in Section 1.7, our 2D measurements contain a signal proportional to a product of the two THz pump fields E_A and E_B. We suggested two possible contributions:

$$\text{Direct:} \quad P = \epsilon_0 \chi^{(3)} E_A E_B E_{\mathrm{pr}} \tag{3.1}$$

$$\text{Cascaded:} \quad P = \epsilon_0 \chi^{(2)} \underbrace{\left[\chi^{(2)} E_A E_B\right]}_{\text{Reradiated}} E_{\mathrm{pr}}. \tag{3.2}$$

The first contribution is a direct third-order process between the THz fields and the optical probe. The second contribution involves two cascaded second-order processes, wherein the first step of the cascaded process entails the direct mixing of the two THz pump fields. To distinguish between the two contributions, we apply numerically-solved derivatives of the unidirectional pulse propagation equation (UPPE) developed by Kolesik and Moloney [33], with an algorithm similar to that used by Caumes et al. [10].

Our method is a two-step process. In the first 'THz-THz' step, we propagate the THz pump fields alone, in a carrier-resolved manner, to map their linear and nonlinear evolution through the crystal. In the second 'THz-probe' step, we propagate the optical probe through the material, considering its interaction with the previously calculated THz field map. A flowchart of the method is provided in Fig. 3.1. Since the bandwidth of the optical probe pulse is relatively small compared to its central frequency, the slowly varying envelope approximation (SVEA) is sufficiently accurate for the latter propagation [1, p.34]. Separating the THz and probe propagation calculations greatly reduces the numerical overhead. However, by isolating the THz field propagation, we essentially assume that the probe has an insignificant effect on the evolution of the THz field—equivalent to assuming the THz field is a 'strong pump' in the second propagation. This approximation is supported by the relatively small probe energy of $266\,\mathrm{nJ}$, the large pump energy of $3.06\,\mathrm{uJ}$, and the disparity in their photon energies—$\sim 1.55\,\mathrm{eV}$ and $\sim 0.0124\,\mathrm{eV}$ respectively. As a result, there are around 10^3 pump photons for every probe photon.

We only consider processes up to third-order in our simulation, although, quasi higher-order processes can still occur through cascading. As a practical matter, this approach avoids increasing analytic and numerical complexity beyond third-order; however, it does not prevent us from capturing the prevailing nonlinear behavior, since lower order contributions tend to be most significant. The nonlinear susceptibility tensors, $\chi^{(n)}$, generally decrease in strength by 10^{-12n} for $n > 1$ [7, p.3].

In the following sections, we outline the derivation and implementation of our method for studying direct and cascaded second- and third-order nonlinear optical processes between THz fields and an optical probe-pulse. We begin by following the procedure of Kolesik and Moloney [33] for deriving the forward Maxwell equation (FME) [29] and nonlienar Schrödinger equation (NLSE) from the UPPE. These are the carrier-resolved and envelope-approximation propagation equations, respectively. We then proceed to calculate the relevant polarization components, and finally, we give a brief description of the 'THz-THz' and 'THz-probe' steps of the method.

3.1 Derivation of the FME and NLSE

Kolesik and Moloney [33] provide an excellent guide for the development of numerically-solved pulse propagation simulations, which we have fully utilized in this section. Our only contributions are minor modifications that tailor their solutions to our specific problem. The unidirectional pulse propagation equation UPPE that they developed differs from solving Maxwell's equations only in the approximation that the backward traveling or "reflected"

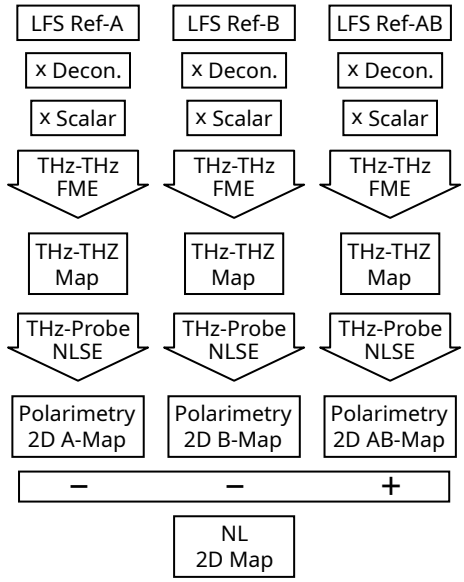

Figure 3.1. Flow chart of the numerical pulse propagation simulations. There are three parallel threads leading to the final nonlinear map (NL): one each for the A and B THz pump pulses alone, and one for their combined application. In each case we start with a low-field-strength (LFS) reference of the THz waveform (see Section 4.1), multiply it by a deconvolution factor to account for dispersion, loss, and the optical pulse duration, and then a scaling factor to simulate a chosen field strength. The THz pulses alone are propagated with the forward Maxwell equation (FME) to generate a map of their linear and nonlinear ('THz-THz') evolution through the crystal. This map is then sampled by the probe in a following 'THz-probe' propagation, carried out with the nonlinear Schrödinger equation (NLSE). The result is a 2D map of the polarimetric signal one would measure in the experiment. As done with the experimental data, the three maps are differenced to calculate the residual nonlinear (NL) signal.

components of the field are not required for calculating the nonlinear response of the medium. By further constraining the UPPE, one can derive other commonly used approximations of Maxwell's equations, such as the nonlinear Schrödinger equation (NLSE), and the forward Maxwell equation (FME). The following assumptions have been made for both the FME and the NLSE:

1. The pulse propagates down the z-coordinate axis.
2. The z or longitudinal components of the field are negligible in comparison to the transverse components (*i.e.* no extreme focusing).
3. Backward-traveling waves do not contribute to the nonlinear polarization.
4. The medium is homogeneous (but not necessarily isotropic)
5. Pulse propagation is sufficiently captured within a finite volume in space and time (this restriction is only for the numerical solution).

The scalar approximation of the UPPE is the starting point for deriving the NLSE and FME, it is defined as follows [33, Eqn. (39)]:

$$\partial_z E_{k_x k_y}(z,\omega) = iK E_{k_x k_y}(z,\omega) + iQ P_{k_x k_y}(z,\omega), \tag{3.3}$$

where

$$K(k_x k_y, \omega) = \sqrt{\omega^2 \epsilon(\omega)/c^2 - k_x^2 - k_y^2}, \tag{3.4}$$

and

$$Q(k_x k_y, \omega) = \frac{\omega^2}{2\epsilon_0 c^2 \sqrt{\omega^2 \epsilon(\omega)/c^2 - k_x^2 - k_y^2}}. \tag{3.5}$$

To derive the NLSE and FME, one selects appropriate approximations for K and Q.

3.1.1 Deriving the NLSE from the UPPE

For the NLSE one assumes a carrier-modulated envelope solution for the electric field, with angular frequency ω_0 and wave number $k_0 = k(\omega_0)$. The approximations for K and Q are

$$K \simeq k_0 + v_g^{-1}(\omega - \omega_0) + \cancel{\frac{k''}{2}(\omega - \omega_0)^2} - \cancel{\frac{1}{2k_0}(k_x^2 + k_y^2)}, \tag{3.6}$$

$$Q \simeq \frac{\omega_0}{2\epsilon_0 n(\omega_0) c}, \tag{3.7}$$

where v_g is the group velocity of the probe pulse. We further assume that dispersion can be ignored for the $\sim$100 fs FWHM probe pulse, and that it is a plane wave, leading respectively to the cancellation of the last two terms in K. The electric field and its Fourier transform are then

$$E(x,y,z,t) \simeq E(z,t) = \mathcal{A}(z,t) e^{i(k_0 z - \omega_0 t)}, \tag{3.8}$$

$$\text{FT:} \quad E(z, \omega - \omega_0) = \mathcal{A}(z, \omega - \omega_0) e^{i k_0 z}, \tag{3.9}$$

where $\mathcal{A}(z,t)$ is the complex envelope of the pulse. Substituting K, Q and $E(z, \omega - \omega_0)$ into Eqn. (3.3) yields

$$\partial_z \mathcal{A} + \cancel{ik_0 \mathcal{A}} = \cancel{ik_0 \mathcal{A}} + iv_g^{-1}(\omega - \omega_0)\mathcal{A} + \frac{i\omega_0}{2\epsilon_0 n(\omega_0) c}\mathcal{P} \tag{3.10}$$

Unlike Kolesik and Moloney [33], we maintain a generalized nonlinear polarization amplitude $\mathcal{P}(z,\omega)$. Transforming the NLSE to the time-domain, we obtain

$$\partial_z \mathcal{A}(z,t) = -v_g^{-1} \partial_t \mathcal{A}(z,t) + \frac{i\omega_0}{2\epsilon_0 n(\omega_0) c}\mathcal{P}(z,t), \tag{3.11}$$

where we have used the relation $i(\omega - \omega_0) \to -\partial_t$ when applied to a function modulated at carrier frequency ω_0.

To make the NLSE more amenable to numerical solution, we transform to a reference frame moving at the group velocity v_g by making the substitutions $\hat{t} = t - v_g^{-1} z$ and $\hat{z} = z$. The temporal and spatial operators $\partial_{\hat{t}}$ and $\partial_{\hat{z}}$ can be found with the chain rule. For $\partial_{\hat{t}}$ we have

$$\partial_t f(\hat{z},\hat{t}) = \frac{\partial f(\hat{z},\hat{t})}{\partial \hat{z}}\frac{\partial \hat{z}}{\partial t} + \frac{\partial f(\hat{z},\hat{t})}{\partial \hat{t}}\frac{\partial \hat{t}}{\partial t} \tag{3.12}$$

$$= \frac{\partial f(\hat{z},\hat{t})}{\partial \hat{z}}(0) + \frac{\partial f(\hat{z},\hat{t})}{\partial \hat{t}}(1) \tag{3.13}$$

$$= \frac{\partial f(\hat{z},\hat{t})}{\partial \hat{t}} \tag{3.14}$$

$$\therefore \partial_t = \partial_{\hat{t}}, \tag{3.15}$$

and for $\partial_{\hat{z}}$ we have

$$\partial_z f(\hat{z},\hat{t}) = \frac{\partial f(\hat{z},\hat{t})}{\partial \hat{z}}\frac{\partial \hat{z}}{\partial z} + \frac{\partial f(\hat{z},\hat{t})}{\partial \hat{t}}\frac{\partial \hat{t}}{\partial z} \tag{3.16}$$

$$= \frac{\partial f(\hat{z},\hat{t})}{\partial \hat{z}}(1) + \frac{\partial f(\hat{z},\hat{t})}{\partial \hat{t}}(-v_g^{-1}) \tag{3.17}$$

$$\therefore \partial_z = \partial_{\hat{z}} - v_g^{-1}\partial_{\hat{t}}. \tag{3.18}$$

Making these substitutions, the NLSE in the moving frame takes the form

$$\partial_{\hat{z}}\mathcal{A}(\hat{z},\hat{t}) = \frac{i\omega_0}{2\epsilon_0 n(\omega_0)c}\mathcal{P}(\hat{z},\hat{t}). \tag{3.19}$$

3.1.2 Deriving the FME from the UPPE

For the FME, few approximations are needed following the derivation of the scalar UPPE. In line with the requirement that the z or longitudinal component of the field is small, it is assumed that $k_x^2, k_y^2 \ll k_z^2 = \epsilon(\Omega)\,\Omega^2/c^2$, where we have made a change of variable name $\omega \to \Omega$ in anticipation that the FME will be used for the THz pump pulses. Given this assumption, the paraxial and zeroth-order approximations of K and Q respectively are then

$$K \simeq k(\Omega) - \frac{c}{2\Omega n(\Omega)}(k_x^2 + k_y^2), \qquad Q \simeq \frac{\Omega}{2\epsilon_0 c n(\Omega)}. \tag{3.20}$$

Substituting K and Q into Eqn. (3.3) yields

$$\partial_z E_{k_x k_y}(z,\Omega) = ik(\Omega)E_{k_x k_y}(z,\Omega) - \frac{ic}{2\Omega n(\Omega)}(k_x^2 + k_y^2)E_{k_x k_y}(z,\Omega) + \frac{i\Omega}{2\epsilon_0 c n(\Omega)}P_{k_x k_y}(z,\Omega). \tag{3.21}$$

The foregoing equation can be transformed to real-space in the transverse direction using the Fourier transform pair $ik_{x/y} \rightarrow -\partial_{x/y}$, or when used in succession, $-(k_x^2 + k_y^2) \rightarrow (\partial_x^2 + \partial_y^2) = \nabla_\perp$. Applying this relation, we have

$$\partial_z E(x,y,z,\Omega) = ik(\Omega)E(x,y,z,\Omega) + \frac{ic}{2\Omega n(\Omega)}\nabla_\perp E(x,y,z,\Omega) + \frac{i\Omega}{2\epsilon_0 cn(\Omega)}P(x,y,z,\Omega). \quad (3.22)$$

Assuming a plane-wave approximation for the THz pump pulses, there is no transverse spatial dependence, and the FME reduces to

$$\partial_z E(z,\Omega) = ik(\Omega)E(z,\Omega) + \frac{i\Omega}{2\epsilon_0 cn(\Omega)}P(z,\Omega). \quad (3.23)$$

As done for the NLSE, we transform to a reference frame moving at the *probe* group velocity v_g by making the substitutions $\hat{t} = t - v_g^{-1}z$ and $\hat{z} = z$. Ensuring our solutions are in the same reference frame allows us to easily calculate coupled polarization products involving both the THz and optical-probe fields. Using the relation $\partial_z = \partial_{\hat{z}} - v_g^{-1}\partial_{\hat{t}}$ (Eqn. 3.18) and $\partial_{\hat{t}} \rightarrow -i\Omega$, the FME in the moving frame is

$$\partial_{\hat{z}} E(\hat{z},\Omega) + i\Omega v_g^{-1} E(\hat{z},\Omega) = ik(\Omega)E(\hat{z},\Omega) + \frac{i\Omega}{2\epsilon_0 cn(\Omega)}P(\hat{z},\Omega). \quad (3.24)$$

Rearranging the equation reveals that the moving frame of reference effectively re-centers the refractive index of the material about the group-index seen by the probe, $n_g(\omega_0) = c/v_g$. In this form,

$$\partial_{\hat{z}} E(\hat{z},\Omega) = i\left[n(\Omega) - n_g(\omega_0)\right]\frac{\Omega}{c}E(\hat{z},\Omega) + \frac{i\Omega}{2\epsilon_0 cn(\Omega)}P(\hat{z},\Omega). \quad (3.25)$$

If the nonlinear polarization term is zero, the solution to Eqn. (3.25) is simply the pulse at $z = 0$ multiplied by a factor carrying the spectral phase accrued with respect to that of the optical probe pulse. Solving for that case, we obtain

$$\partial_{\hat{z}} E(\hat{z},\Omega) = i\left[n(\Omega) - n_g(\omega_0)\right]\frac{\Omega}{c}E(\hat{z},\Omega) \quad (3.26)$$

$$\therefore E(\hat{z},\Omega) = E(z=0,\Omega)e^{i[n(\Omega)-n_g(\omega_0)]\frac{\Omega}{c}z}. \quad (3.27)$$

The vectorial nature of light is partially captured with the FME by simultaneously solving two coupled scalar equations, one for each transverse component of the field. Again, the following equations assume a relatively small longitudinal ($\hat{\mathbf{e}}_z$) field component:

$$\partial_{\hat{z}} E(\hat{z},\Omega)\hat{\mathbf{e}}_i = i\left[n(\Omega) - n_g(\omega_0)\right]\frac{\Omega}{c}E(\hat{z},\Omega)\hat{\mathbf{e}}_i + \frac{i\Omega}{2\epsilon_0 cn(\Omega)}P(\hat{z},\Omega)\hat{\mathbf{e}}_i, \quad i \in \{x,y\}. \quad (3.28)$$

3.1.3 Calculating DFT Terms in the FME Jacobian

This subsection is not strictly necessary for understanding the simulations, however, it may be useful for those trying to implement their own solver. When calculating the polarization terms in the FME, we first Fourier transform to the time-domain where products and powers of the fields are computed, then inverse Fourier transform the result to get the spectral representation. These Fourier transforms, implemented numerically using the discrete Fourier transform (DFT) in NumPy [24], couple the FME ordinary differential equations (ODEs) together, since each ODE represents one frequency component of our pulse. In NumPy the forward and inverse DFT are defined as follows:

$$\text{forward DFT:} \qquad A_k = \sum_{m=0}^{N-1} a_m \exp\Big\{-2\pi i \frac{mk}{N}\Big\} \qquad k = 0, \ldots, N-1, \tag{3.29}$$

$$\text{inverse DFT:} \qquad a_m = \frac{1}{N} \sum_{k=0}^{N-1} A_k \exp\Big\{2\pi i \frac{mk}{N}\Big\} \qquad m = 0, \ldots, N-1. \tag{3.30}$$

Note again that the temporal signal at the m-th index is a weighted sum of all frequencies from $k = 0$ to $k = N-1$. It is also worth pointing out that k is *not* an angular frequency; the factor of 2π is absorbed to retrieve the angular-frequencies we have, at times, simply called 'frequencies'.

As an example for demonstrating the DFT-produced coupling between ODEs, let us consider ODEs of the form

$$\frac{\mathrm{d}E(z,\Omega)}{\mathrm{d}z} = Y(z,\Omega) = \mathcal{F}\left[\mathcal{F}^{-1}E(z,\Omega)\right]^{\alpha} = \mathcal{F}\,E(z,t)^{\alpha} = \mathcal{F}\,P(z,t), \tag{3.31}$$

where z is the propagation distance, $E(z,\Omega)$ is the electric field in the frequency domain, and $Y(z,\Omega)$ is the rate of change of that field in z. Here we consider a generic polarization term $P(z,t) = [E(z,t)]^{\alpha}$ in the time-domain. Discretizing the initial field at N points in time and applying the definitions of the forward and inverse DFT, we have

$$Y_j = \sum_{m=0}^{N-1} e^{-2\pi i \frac{mj}{N}} \left[\frac{1}{N}\sum_{k=0}^{N-1} E_k e^{2\pi i \frac{mk}{N}}\right]^{\alpha}. \tag{3.32}$$

The Jacobian for our system of ODEs is a square $N \times N$ matrix, where the (j,l)-th element is $\mathrm{d}Y_j/\mathrm{d}E_l$. The l-th index represents the k-th frequency component of the field, but has been redefined to avoid confusion with the generic k-th index used in the definition of the DFT. Loosely speaking, the elements represent the change in the growth rate of the field at Ω_l with

respect to the present strength of all other fields at $\Omega_k, k \in [0, N]$.

$$\begin{matrix} & \leftarrow \mathrm{d}E_l \rightarrow \\ \uparrow \\ \mathrm{d}Y_j \\ \downarrow \end{matrix} \begin{bmatrix} & \\ & \frac{\mathrm{d}Y_j}{\mathrm{d}E_l} \\ & \end{bmatrix} \tag{3.33}$$

We can partially calculate $\mathrm{d}Y_j/\mathrm{d}E_l$ as follows:

$$\frac{\mathrm{d}Y_j}{\mathrm{d}E_l} = \sum_{m=0}^{N-1} e^{-2\pi i \frac{mj}{N}} \frac{\mathrm{d}}{\mathrm{d}E_l} \left[\frac{1}{N} \sum_{k=0}^{N-1} E_k e^{2\pi i \frac{mk}{N}} \right]^{\alpha} \tag{3.34}$$

$$= \sum_{m=0}^{N-1} e^{-2\pi i \frac{mj}{N}} \alpha \left[\frac{1}{N} \sum_{k=0}^{N-1} E_k e^{2\pi i \frac{mk}{N}} \right]^{\alpha-1} \frac{1}{N} \sum_{k=0}^{N-1} \frac{\mathrm{d}E_k}{\mathrm{d}E_l} e^{2\pi i \frac{mk}{N}} \quad \left(\frac{\mathrm{d}E_k}{\mathrm{d}E_l} = \delta_{kl}\right) \tag{3.35}$$

$$= \sum_{m=0}^{N-1} \underbrace{e^{-2\pi i \frac{mj}{N}}}_{\text{at } \Omega_j} \underbrace{\left(\alpha \left[\mathcal{F}^{-1} E\right]^{\alpha-1}\right)_m}_{\text{Mixing Prods.}} \frac{1}{N} \underbrace{e^{2\pi i \frac{ml}{N}}}_{\text{at } \Omega_l} . \tag{3.36}$$

The last line is particularly illuminating: the mixing products of the field are sandwiched between two exponentials that essentially isolate the magnitude of the contributions at Ω_j (the 'output' frequency) *and* $-\Omega_l$ (the 'input' frequency), which is the difference frequency $\Omega_k = \Omega_j - \Omega_l$. If the medium were linear ($\alpha = 1$), the sum would reduce to $\sum_{m=0}^{N-1} \delta_{jl}/N$, which is 1 iff $j = l$ and zero otherwise. In other words, if no new frequency components are being generated, the rate of change of the field component at Ω_j is solely dependent on its current magnitude, and the Jacobian is the identity matrix.

If the medium is nonlinear and the polarization contains higher order terms ($\alpha > 1$), then frequency-mixing generates new frequency components at Ω_k. Rearranging Eqn. (3.36) once more, so that

$$\frac{\mathrm{d}Y_j}{\mathrm{d}E_l} = \frac{1}{N} \sum_{m=0}^{N-1} \underbrace{\left(\alpha \left[\mathcal{F}^{-1} E\right]^{\alpha-1}\right)_m}_{\text{Mixing Prods.}} \underbrace{e^{-2\pi i \frac{m(j-l)}{N}}}_{\text{at } \Omega_k = (\Omega_j - \Omega_l)} , \tag{3.37}$$

makes the mixing products at $\Omega_k = (\Omega_j - \Omega_l)$ more clear. Viewed from a different perspective, one contribution to the rate of sum frequency generation $Y_j = \mathrm{d}E_j/dz$ at frequency $\Omega_j = \Omega_k + \Omega_l$, is proportional to the magnitude of the field components at Ω_k and Ω_l. Each column of the Jacobian considers a contribution with a different Ω_l.

3.2 Calculating Polarization Terms

Generally, the total polarization $\tilde{\mathbf{P}}$ induced in a material is not linear in the electric field $\mathbf{E}$. Instead, it can be represented by an expansion in powers of $\mathbf{E}$ as follows [1, p.15]:

$$\tilde{\mathbf{P}} = \epsilon_0 \left(\chi^{(1)} \cdot \mathbf{E} + \chi^{(2)} : \mathbf{EE} + \chi^{(3)} \vdots \mathbf{EEE} + \cdots \right), \tag{3.38}$$

where ϵ_0 is the vacuum permittivity and $\chi^{(j)}$ is the jth order susceptibility. The susceptibility $\chi^{(j)}$ is a material-dependent tensor of rank $j+1$. In our simulations, we only consider the first three terms of the expansion. The first linear term is treated separately and will largely be removed by operating in a reference frame moving at the group velocity of the optical probe pulse. In the NLSE [Eqn. (3.19)] and the FME [Eqn. (3.28)], $\boldsymbol{\mathcal{P}}$ and $\mathbf{P}$ represent the nonlinear portions of $\tilde{\mathbf{P}}$. In the following, we detail how we calculate the polarizations for the THz-probe and THz-THz simulations separately. From here on, **the coordinate system has been changed** such that the pulse travels down the x-coordinate; therefore, $x \to y$, $y \to z$ and $z \to x$ with respect to Section 3.1. This will prove to be a more simple frame of reference when calculating the polarization components of ZnTe.

3.2.1 THz-Probe Polarization Terms

Let us start with the second-order polarization term

$$\mathbf{P}^{(2)} = \epsilon_0 \chi^{(2)} : \mathbf{EE}, \tag{3.39}$$

where $\mathbf{E}$ is the total *real* electric field. Following the approach of Cornet et al. [14], for the optical probe field we have an envelope-modulated plane-wave

$$\tilde{\mathbf{E}}_{\mathrm{pr}} = \frac{1}{2} \left[\tilde{\boldsymbol{\mathcal{A}}}_{\mathrm{pr}}(x,t) e^{i(k_{\mathrm{pr}} x - \omega_{\mathrm{pr}} t)} + c.c. \right], \tag{3.40}$$

where $\tilde{\boldsymbol{\mathcal{A}}}_{\mathrm{pr}}(x,t)$ is the complex envelope of the pulse and $c.c.$ is the complex conjugate. However, as done for the derivation of the NLSE (Sec. 3.1.1), we only consider the forward-traveling component by dropping the complex conjugate and absorbing the factor of $1/2$, yielding:

$$\mathbf{E}_{\mathrm{pr}} = \boldsymbol{\mathcal{A}}_{\mathrm{pr}}(x,t) e^{i(k_{\mathrm{pr}} x - \omega_{\mathrm{pr}} t)}. \tag{3.41}$$

For the THz pump field we simply have $\mathbf{E}_{\mathrm{pu}}$, which is the measured real-field. We do not factor a carrier frequency out of $\mathbf{E}_{\mathrm{pu}}$, because it only consists of a few cycles that vary slowly in comparison to the envelope of the optical probe pulse. The total field in the crystal is a sum of the probe and THz fields,

$$\mathbf{E} = \mathbf{E}_{\mathrm{pr}} + \mathbf{E}_{\mathrm{pu}}. \tag{3.42}$$

Inserting the total field into the definition of the second order polarization, Eqn. (3.39), we have

$$\mathbf{P}^{(2)} = \epsilon_0 \chi^{(2)} : (\mathbf{E}_{\mathrm{pr}} + \mathbf{E}_{\mathrm{pu}})^2, \tag{3.43}$$

$$\mathbf{P}^{(2)} = \epsilon_0 \chi^{(2)} : \left(\underbrace{\cancel{\mathbf{E}_{\mathrm{pr}}^2}}_{\sim 2\omega_{\mathrm{pr}}} + \underbrace{2\mathbf{E}_{\mathrm{pr}}\mathbf{E}_{\mathrm{pu}}}_{\sim \omega_{\mathrm{pr}}} + \underbrace{\cancel{\mathbf{E}_{\mathrm{pu}}^2}}_{\sim 0} \right). \tag{3.44}$$

In our simulations, we only consider components with an angular frequency near ω_{pr}. The THz components (~ 0) are not detectable on a photo diode, and will be treated separately in the next section. We have run the experiment with and without a $40\,\mathrm{nm}$ bandpass filter centered at $\omega_{\mathrm{pr}} \leftrightarrow 800\,\mathrm{nm}$ (Thorlabs FB800-40), which would filter out the components near the second harmonic $2\omega_{\mathrm{pr}}$, and saw little if any change.

The second-order polarization of interest can be expanded as a summation over its various polarization components as follows:

$$\mathbf{P}^{(2)} = \epsilon_0 \chi^{(2)} : 2\mathbf{E}_{\mathrm{pr}}\mathbf{E}_{\mathrm{pu}}, \tag{3.45}$$

$$P_i^{(2)} = 2\epsilon_0 \sum_{jk} \chi_{ijk}^{(2)} E_{\mathrm{pr}_j} E_{\mathrm{pu}_k}, \tag{3.46}$$

$$P_i^{(2)} = 2\epsilon_0 \sum_{jk} \chi_{ijk}^{(2)} \mathcal{A}_{\mathrm{pr}_j} e^{i(k_{\mathrm{pr}}x - \omega_{\mathrm{pr}}t)} E_{\mathrm{pu}_k}. \tag{3.47}$$

We also treat the polarization as a forward propagating plane-wave oscillating at the probe frequency, and define

$$\mathbf{P}^{(2)} = \boldsymbol{\mathcal{P}}^{(2)}(x,t) e^{i(k_{\mathrm{pr}}x - \omega_{\mathrm{pr}}t)}. \tag{3.48}$$

The complex envelope of the polarization amplitude is then

$$\mathcal{P}_i^{(2)}(x,t) = 2\epsilon_0 \sum_{jk} \chi_{ijk}^{(2)} \mathcal{A}_{\mathrm{pr}_j} E_{\mathrm{pu}_k}. \tag{3.49}$$

In Section 4.2 we explicitly calculate the non-zero polarization terms for both $\langle 100 \rangle$ and $\langle 110 \rangle$ cut ZnTe. For now, we move on to calculating the third-order terms.

The process proceeds as before, except we cube the total field to obtain

$$\mathbf{P}^{(3)} = \epsilon_0 \chi^{(3)} \vdots (\mathbf{E}_{\mathrm{pr}} + \mathbf{E}_{\mathrm{pu}})^3, \tag{3.50}$$

$$\mathbf{P}^{(3)} = \epsilon_0 \chi^{(3)} \vdots \left(\underbrace{\cancel{\mathbf{E}_{\mathrm{pr}}^3}}_{\sim 3\omega_{\mathrm{pr}}} + \underbrace{3\mathbf{E}_{\mathrm{pr}}^2\mathbf{E}_{\mathrm{pu}}}_{\sim 2\omega_{\mathrm{pr}}} + \underbrace{3\mathbf{E}_{\mathrm{pr}}\mathbf{E}_{\mathrm{pu}}^2}_{\sim \omega_{\mathrm{pr}}} + \underbrace{\cancel{\mathbf{E}_{\mathrm{pu}}^3}}_{\sim 0} \right). \tag{3.51}$$

Again, we only keep the terms oscillating near ω_{pr}. Expanding the selected term as a summation over the various polarization components we have

$$\mathbf{P}^{(3)} = \epsilon_0 \chi^{(3)} \vdots 3\mathbf{E}_{\mathrm{pr}}{\mathbf{E}_{\mathrm{pu}}}^2, \tag{3.52}$$

$$P_i^{(3)} = 3\epsilon_0 \sum_{jkl} \chi_{ijkl}^{(3)} E_{\mathrm{pr}_j} E_{\mathrm{pu}_k} E_{\mathrm{pu}_l}, \tag{3.53}$$

$$P_i^{(3)} = 3\epsilon_0 \sum_{jkl} \chi_{ijkl}^{(3)} \mathcal{A}_{\mathrm{pr}_j} e^{i(k_{\mathrm{pr}}x - \omega_{\mathrm{pr}}t)} E_{\mathrm{pu}_k} E_{\mathrm{pu}_l}. \tag{3.54}$$

Using a similar plane-wave assumption for the polarization, the corresponding complex envelope becomes

$$\mathcal{P}_i^{(3)}(x,t) = 3\epsilon_0 \sum_{jkl} \chi_{ijkl}^{(3)} \mathcal{A}_{\mathrm{pr}_j} E_{\mathrm{pu}_k} E_{\mathrm{pu}_l}. \tag{3.55}$$

When calculating the NLSE [Eqn. (3.19)], the sum of the second- and third-order polarizations is taken as the total nonlinear polarization,

$$\mathcal{P}_i(x,t) = \mathcal{P}_i^{(2)}(x,t) + \mathcal{P}_i^{(3)}(x,t). \tag{3.56}$$

3.2.2 THz-THz Polarization Terms

Calculating the second and third order contributions to the nonlinear polarization for the THz-THz simulations proceeds in the same manner as for the THz-probe simulations. However, the total field $\mathbf{E}$ is now simply $\mathbf{E}_{\mathrm{pu}}$. Depending on the particular sub-simulation, $\mathbf{E}_{\mathrm{pu}}$ will be one of the THz pump pulses $\mathbf{A} = \mathbf{E}_A(t)$ or $\mathbf{B} = \mathbf{E}_B(t)$, or the sum of both.

Let us start again with the second-order polarization term, immediately substituting the total field $\mathbf{E}_{\mathrm{pu}}$ to find

$$\mathbf{P}^{(2)} = \epsilon_0 \chi^{(2)} : \underbrace{\mathbf{E}_{\mathrm{pu}}\mathbf{E}_{\mathrm{pu}}}_{\sim \pm 2\Omega_0 \text{ and } \sim 0}, \tag{3.57}$$

where Ω_0 is the approximate center-angular-frequency of the THz pump pulses. As before, this can be expanded as a sum over polarization components:

$$\mathbf{P}^{(2)} = \epsilon_0 \chi^{(2)} : \mathbf{E}_{\mathrm{pu}}\mathbf{E}_{\mathrm{pu}}, \tag{3.58}$$

$$P_i^{(2)} = 2\epsilon_0 \sum_{jk} \chi_{ijk}^{(2)} E_{\mathrm{pu}_j} E_{\mathrm{pu}_k}. \tag{3.59}$$

Notably, this is as far as we need to go, since we will not be making an envelope approximation in the FME. The process is the same for the third-order polarization:

$$\mathbf{P}^{(3)} = \epsilon_0 \chi^{(3)} \vdots \underbrace{\mathbf{E}_{\mathrm{pu}}\mathbf{E}_{\mathrm{pu}}\mathbf{E}_{\mathrm{pu}}}_{\sim \pm 3\Omega_0 \text{ and } \sim \pm \Omega_0}, \tag{3.60}$$

$$P_i^{(3)} = \epsilon_0 \sum_{jkl} \chi_{ijkl}^{(3)} E_{\mathrm{pu}_j} E_{\mathrm{pu}_k} E_{\mathrm{pu}_l}. \tag{3.61}$$

The sum of the second- and third-order polarizations is again taken as the total nonlinear polarization,

$$P_i(x,t) = P_i^{(2)}(x,t) + P_i^{(3)}(x,t). \tag{3.62}$$

One major deviation from the THz-probe polarizations is that the Fourier transform of the total polarization,

$$P_i(x,\Omega) = \mathcal{F}\{P_i(x,t)\}, \tag{3.63}$$

will be used in the FME, since the equation is solved in the frequency-domain. However, as a practical matter, the total polarization will still be calculated in the time-domain, where it is intuitive to multiply the fields, rather than in the frequency domain where computation would require convolving the spectra [8, p. 115].

3.3 THz-THz simulations

In this first part of the simulation, we propagate the THz pump fields alone to map their linear and nonlinear evolution through the crystal. We will be solving the carrier-resolved forward Maxwell Equation [Eqn. (3.28)] that was rederived from the UPPE in Section 3.1.2. We continue to work in the coordinate system where the pulse travels down the x-coordinate ($x \to y$, $y \to z$ and $z \to x$ with respect to Section 3.1). Making the transformation, Eqn. (3.28) takes the form

$$\frac{\partial \mathbf{E}_{\mathrm{pu}}(x,\Omega)}{\partial x} = i\frac{[n(\Omega) - n_{\mathrm{gr}}(\omega_0)]\Omega}{c}\mathbf{E}_{\mathrm{pu}}(x,\Omega) + \frac{i\Omega}{2\epsilon_0 c n(\Omega)}\mathbf{P}_{\mathrm{pu}}(x,\Omega). \tag{3.64}$$

As a reminder, we have already taken a plane wave approximation, and are operating in a reference frame moving at the group velocity of the optical probe, $v_g = c/n_{\mathrm{gr}}(\omega_0)$. We consider the center wavelength of the probe to be $800\,\mathrm{nm}$, and determine the respective group refractive index, n_{gr}, in ZnTe using the values tabulated by [36]. For the refractive index in the THz domain, $n(\Omega)$, the real component is derived from the model for the dielectric constant provided by Gallot et al. [20, Eqn. (1)]. The imaginary component was extracted with an interpolation of the power absorption coefficient provided by the same authors [20, Fig. 1(b)]. We chose to interpolate the measured data for the imaginary components, since their model for the dielectric constant does not account for two broad absorption features around $1.6\,\mathrm{THz}$ and $3.7\,\mathrm{THz}$. The values are provided in Fig. 3.2, where we have converted the imaginary index components to more commonly used power absorption coefficients, α, using the relation

$$\alpha = \frac{2\Omega}{c}\mathrm{Im}\big[n(\Omega)\big]. \tag{3.65}$$

The vector FME will be solved as two separate scalar equations, one for each of the transverse components $\hat{y}$ and $\hat{z}$. The general second- and third order polarization terms were defined in Section 3.2.2, and the vector $\mathbf{P}_{\mathrm{pu}}$ is the sum over the transverse components

$$\mathbf{P}_{\mathrm{pu}}(x,\Omega) = \sum_i P_i(x,\Omega). \tag{3.66}$$

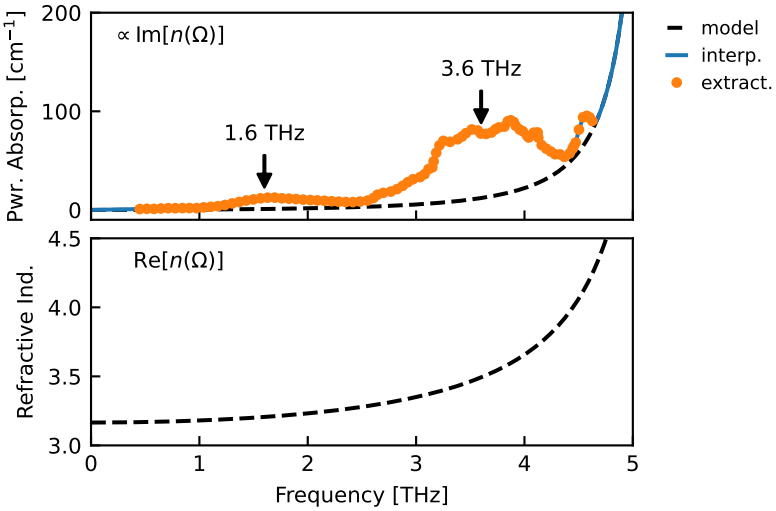

Figure 3.2. Power absorption coefficient and refractive index for ZnTe derived from [20] and used in the simulation. (a) The power absorption coefficient, α. There are two broad peaks at 1.7 THz and 3.6 THz in the data extracted from [20, fig. 1(b)] that are not included in the Lorentzian model [20, Eqn. (1)]. Thus, we have interpolated the data and extended it with the model. (b) The refractive index of ZnTe based on a Lorentzian oscillator model [20, Eqn. (1)].

The specific form of the polarization in ZnTe, for several experimental configurations, is discussed in Section 4.2.

Our model needs an initial field to propagate. To that end, we have recorded a reference THz waveform at a low field strength, such that any measured nonlinearities are negligible. To record the waveform, we used electro-optic detection (Section 2.4) in a $\langle 110 \rangle$ cut ZnTe crystal with a thickness of $l = 1\,\mathrm{mm}$. The details of this measurement are discussed in Section 4.1. The reference field is apodized with a Tukey window and interpolated with a spline so that is can be uniformly sampled at any desired density, typically we use 2^8 points. These points are distributed over a window that is approximately five times wider than the reference pulse, to avoid window-edge effects as the pulse disperses during the simulation. We zero pad the reference waveform so that the simulation domain is $[-10\,\mathrm{ps}, 18\,\mathrm{ps}]$, where $0\,\mathrm{ps}$ is approximately the leading edge of the pulse.

Notably, the resulting waveform represents the field measured as it propagates across the length of the crystal, not the field at the front face of the crystal. We will call this measured field $\mathbf{E}_{\mathrm{pu}}(x = l, t)$. Although $\mathbf{E}_{\mathrm{pu}}(x = l, t)$ contains negligible nonlinear content, the effects of material dispersion and loss, as well as convolution with the finite-duration optical probe, are significant. To attempt to nullify these contributions and retrieve an accurate representation of the waveform at the front face of the crystal, we Fourier transform $\mathbf{E}_{\mathrm{pu}}(x = l, t)$ and apply a deconvolution factor in the frequency domain. The spectrum of the THz waveform

at the front face of the crystal, and the input to our simulation, is taken to be:

$$\mathbf{E}_{\mathrm{pu}}(x=0,\Omega) = \frac{1}{f(\Omega)} \int_{-\infty}^{\infty} e^{i\Omega t} \mathbf{E}_{\mathrm{pu}}(x=l,t)dt. \tag{3.67}$$

The deconvolution factor, $f(\Omega)$, is given by Gallot and Grischkowsky [19]:

$$f(\Omega) = C_{opt}(\Omega)\chi^{(2)}_{eff}(\omega_0;\Omega,\omega_0-\Omega)\frac{\exp(i\Delta k l)-1}{i\Delta k}. \tag{3.68}$$

It is the product of three distinct contributions. The first, C_{opt}, accounts for the non-zero width of the optical probe pulse. It is the spectral amplitude of the optical probe pulse autocorrelation (AC), given by

$$C_{\mathrm{opt}} = \frac{1}{\Delta\Omega\sqrt{2\pi}} \exp(-\Omega^2/(2\Delta\Omega^2)), \tag{3.69}$$

for a Gaussian pulse with a spectral bandwidth

$$\Delta\Omega = 2\pi \frac{0.44}{\mathrm{FWHM}_{\mathrm{pr}}} \frac{1}{2\sqrt{\ln(2)}}, \tag{3.70}$$

where $\mathrm{FWHM}_{\mathrm{pr}}$ is the full-width-at-half-maximum duration of the probe pulse, which is approximately $100\,\mathrm{fs}$. The factor C_{opt} loosely conforms to the convolution theorem of the Fourier transform [8, p.115], since one can imagine electro-optic detection as a cross-correlation between the THz field and the optical probe pulse. In the time-domain, a wide-duration optical pulse will average a large section of the THz waveform, thus smoothing it out. In the frequency domain, a wide-duration pulse has a narrow spectrum. The spectrum of its autocorrelation, which has the carrier removed, is centered about zero THz, thus acting like a low-pass filter. The second contribution,

$$\chi^{(2)}_{eff} = n(\Omega)^2 - 1, \tag{3.71}$$

is the frequency dependent magnitude of the second order susceptibility (based on Miller's rule [6]). The strength of the electro-optic effect is frequency dependent, and is strongly suppressed for high-frequencies near the $5.32\,\mathrm{THz}$ phonon in ZnTe [20]. The remaining contribution,

$$\frac{\exp(i\Delta k l)-1}{i\Delta k}, \tag{3.72}$$

accounts for a lack of phase matching as well as absorption in the material. The wave vector mismatch of a THz field component relative to the effective group-wave-vector for the optical probe pulse is given by:

$$\Delta k = \frac{\Omega}{c}\left[n(\Omega) - n_{\mathrm{gr}}(\omega_0)\right]. \tag{3.73}$$

After applying the deconvolution factor, the THz field is propagated through the material. We use the *solve_ivp* method from SciPy [57], which is a wrapper of the FORTRAN solver

LSODA from ODEPACK [26]; although, a custom solver would likely be more efficient [33]. The spatial step size is selected adaptively by the solver as the solution progresses. The resulting THz waveforms at incremental depths into the material/crystal are interpolated with a bivariate spline approximation over a rectangular mesh *(RectBivariateSpline)*. This spatio-temporal map of the linear and nonlinear evolution of the THz field will be sampled by the optical probe in the 'THz-probe' simulation, as discussed in the following section. An example map is provided in Fig. 3.3.

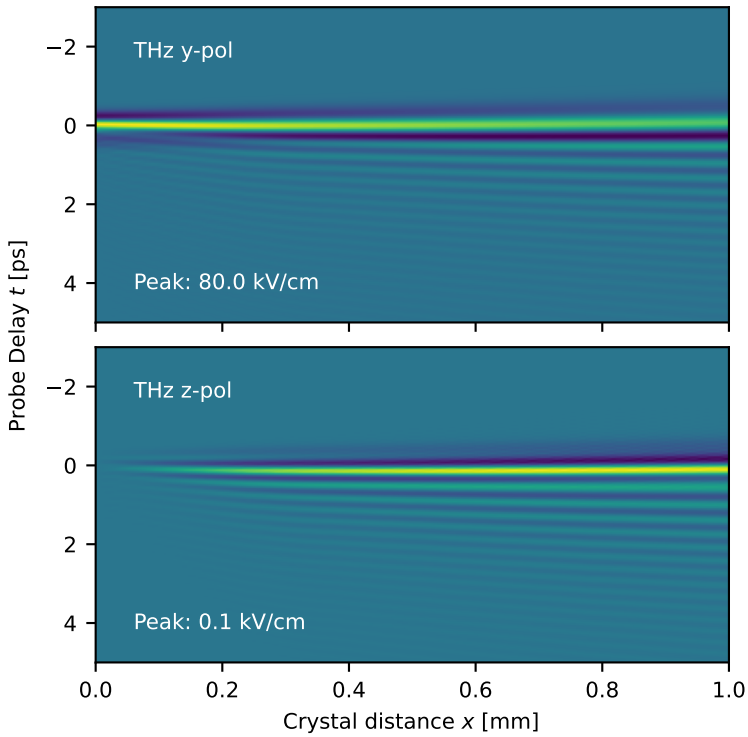

Figure 3.3. Spatio-temporal map of the linear and nonlinear evolution of the THz pump pulse in $1\,\mathrm{mm}$ thick, $\langle 110 \rangle$ ZnTe. The THz pump is initially completely $\hat{y}$ polarized, but as it propagates, a new $\hat{z}$ polarized component is generated. For both components, a long oscillating tail fans outs as the pulse is dispersed in the crystal. The probe delay range of the full map is $[-10\,\mathrm{ps}, 18\,\mathrm{ps}]$, but we have cropped it here to $[-3\,\mathrm{ps}, 5\,\mathrm{ps}]$. The peak field strengths of the $\hat{y}$ and $\hat{z}$ components over the map are indicated in the lower left corner.

3.4 THz-probe simulations

In this second part of the simulation, we propagate the optical probe pulse, considering its nonlinear interaction with the previously calculated spatio-temporal map of the THz pump pulse evolution. Specifically, we will be solving the nonlinear Schrödinger equation (NLSE) [Eqn. (3.19)] that was rederived from the UPPE in Section 3.1.1. We continue to work in the coordinate system where the pulse travels down the x-coordinate ($x \to y$, $y \to z$ and $z \to x$ with respect to Section 3.1). In addition, we want to emphasize that the simulation time, t_{sim}, is not equal to the probe-delay, t (see Note 3.1). Making these variable substitutions, Eqn. (3.19) takes the form

$$\partial_x \boldsymbol{\mathcal{A}}_{\mathrm{pr}}(x, t_{\mathrm{sim}}) = \frac{i\omega_0}{2\epsilon_0 n(\omega_0) c} \boldsymbol{\mathcal{P}}(x, t_{\mathrm{sim}}). \tag{3.74}$$

Note again that we are operating in a reference frame moving at the group velocity of the optical probe, $v_g = c/n_{\mathrm{gr}}(\omega_0)$. It is also worth mentioning that most of the quantities are determined by the center angular frequency of the optical probe, ω_0, corresponding to an $800\,\mathrm{nm}$ wavelength. This vector NLSE equation will be solved as two separate scalar equations, one for each of the transverse components $\hat{y}$ and $\hat{z}$. The general second- and third order polarization terms were defined in Section 3.2.1, and the vector $\boldsymbol{\mathcal{P}}$ is the sum over the transverse components

$$\boldsymbol{\mathcal{P}}(x, t) = \sum_i \mathcal{P}_i(x, t). \tag{3.75}$$

The specific form of the polarization in ZnTe, for several experimental configurations, is discussed in Section 4.2.

Note 3.1 Comparison to the experiment

The probe-delay, t (Fig. 1.4), is an initial relative delay between the THz field and the optical probe pulse. For each t, we carry out a full THz-probe simulation with an array of t_{sim} values that sample the delayed waveforms. This is very much like the experiment, where we step the probe delay stage ('Dly Pr' in Fig. 2.1) to increment t, then record the probe $\hat{y}$ and $\hat{z}$ intensities on photodiodes (effectively an integration over t_{sim}). We repeat this process for all delays t.

Because the FWHM duration of the probe is considerably shorter than the extent of the THz pump pulses and the variations within them, we use a simulation subdomain with a smaller step-size than for the THz-THz simulation, and interpolate the THz map. The subdomain is given by

$$t_{\mathrm{sim}} \in [t - 10\,\mathrm{FWHM}_{\mathrm{pr}},\ t + 10\,\mathrm{FWHM}_{\mathrm{pr}}], \tag{3.76}$$

where the value of the initial THz-probe delay, t, is incremented for each simulation (Note 3.1). A subdomain 20 times wider than the pulse duration avoids edge-effects at the boundary.

Typically, there are 2^8 THz-probe delays (simulations), and 2^7 simulation times, t_{sim}, in the subdomain.

Each simulation is initialized with the probe having a Gaussian complex envelope at the front face of the crystal, given by:

$$\mathcal{A}_{\mathrm{pr}}(x=0,t_{\mathrm{sim}}) = \left(\frac{2\sqrt{\ln 2}}{\mathrm{FWHM}_{\mathrm{pr}}\sqrt{\pi}}\right)^{1/2} \exp\left[\frac{-2\ln 2\,(t_{\mathrm{sim}}-t)^2}{\mathrm{FWHM}_{\mathrm{pr}}^2}\right]. \tag{3.77}$$

Notably, this is the electric field envelope, not the power envelope. The factor before the exponential normalizes the pulse energy to 1.

After simulating the probe-propagation for a given delay t, the effective polarimetric signal, ΔS, is calculated. This is implemented numerically in much the same way it is performed experimentally in the lab. Conceptually, we do the following:

1. Apply the Jones matrix for a quarter-wave plate (QWP) to circularize the probe polarization.
2. Apply the Jones matrix for a polarizer to separate the S- and P-polarized components of the probe.
3. Integrate the intensity of the S- and P-polarized components and take their difference.
4. Normalize the difference by the total integrated probe intensity.

We will now expand on those concepts. Before the crystal, the probe is linearly polarized at an angle θ_{pr}, which is defined absolutely in Fig. 4.7. However, regardless the absolute value, the angle of the QWP and polarizer are always defined relative to the probe angle. The QWP angle $\theta_{\mathrm{q}wp}$ is set to 'bias' the polarization of the probe so that, in the absence of any modulation by the crystal/THz-field, it is circularly polarized. This requires the QWP fast and slow axes to be at $45\,\mathrm{deg}$ to θ_{pr}, thus, $\theta_{\mathrm{q}wp} = \theta_{\mathrm{p}r} + 45\,\mathrm{deg}$. The Wollaston polarizer angle $\theta_{\mathrm{p}ol}$ is set such that, in the absence of the QWP and crystal/THz-field, the probe is entirely P-polarized. Therefore, $\theta_{\mathrm{p}ol} = \theta_{\mathrm{p}r}$. The Jones matrices for the QWP with its fast axis along $\hat{y}$, and the polarizer with its axes along $\hat{z}$ and $\hat{y}$, are as follows:

$$J_{\mathrm{q}wp} = \begin{bmatrix} 1 & 0 \\ 0 & -i \end{bmatrix}, \qquad J_{\mathrm{p}ol} = \begin{bmatrix} 1 & 0 \\ 0 & 1 \end{bmatrix}. \tag{3.78}$$

Rather than calculating Jones matrices for the rotated components, in the simulation it is easier to rotate the fields after the crystal. We apply a series of rotations matrices

$$R(\theta) = \begin{bmatrix} \cos(\theta) & -\sin(\theta) \\ \sin(\theta) & \cos(\theta) \end{bmatrix}, \tag{3.79}$$

where the total Jones matrix for detection is

$$J_{tot} = J_{\mathrm{p}ol} R(-\theta_{\mathrm{p}ol}) R(\theta_{\mathrm{q}wp}) J_{\mathrm{q}wp} R(-\theta_{\mathrm{q}wp}). \tag{3.80}$$

Detection takes place in the frame of the polarizer, where the S- and P-polarized components of the probe are already separated—we do not rotate back into the lab-frame. The detected intensity difference is

$$\Delta I = \sum_{t_{\mathrm{sim}}} \left(|\mathcal{A}_{\mathrm{pr}_S}|^2 - |\mathcal{A}_{\mathrm{pr}_P}|^2 \right) . \tag{3.81}$$

This difference is then normalized by the total probe intensity to get the modulation, $\Delta S = \Delta I / I_0$, which takes a value between 0 and 1.

In the absence of a THz pump field, the probe is perfectly circularly polarized and the polarizer will split the probe into equal S- and P-polarized components. The resulting intensity difference on the photo diodes, and modulation ΔS, would then be zero or 'balanced'. When the probe interacts with the crystal/THz-field the 'effective' polarization is modified (see Section 4.2 for further insights) so that the polarization after the QWP is elliptic, and the S- and P-polarization components after the polarizer are not equal.

CHAPTER 4

Nonlinear Optical Processes in ZnTe

In this chapter, we synthesize what we have discussed thus far and apply it to studying *direct* and *cascaded* nonlinear optical processes in ZnTe.

When discussing the instrumentation in Chapter 2, it may have seemed slightly odd that we avoided directly calling the measurement method electro-optic (EO) detection, and rather emphasized that the measurements were polarimetric. Indeed, we too started this project from the perspective that we were simply electro-optically detecting the fields in ZnTe, but it soon became apparent that this was too narrow a perspective. As emphasized in Section 2.4, polarimetry encompasses all sources of polarization modulation on the optical probe, be they inelastic Raman scattering [32, 38, 42, 52] or photon-energy conservative optical mixing processes [34, 44, 52]. Electro-optic detection results from just *one* of the numerous possible optical mixing contributions due to non-resonant interactions between the electric fields and the electronic-structure of the material. Specifically, in non-centrosymmetric crystals like ZnTe, the dominant interaction between the THz field and the optical probe is the 'linear' electro-optic (Pockels) effect—this is the basis of electro-optic detection. For small fields, the polarization modulation of the optical probe is linearly proportional to the applied THz field strength [45]. However, make no mistake, the 'linear' electro-optic effect is a *nonlinear* process—it is linear in either the THz or optical field, but the overall process is a nonlinear product of the two. This product is more clearly seen in the polarization term associated with the linear electro-optic effect,

$$\mathbf{P}^{(2)} = \epsilon_0 \chi^{(2)} : 2\mathbf{E}_{\mathrm{pr}}\mathbf{E}_{\mathrm{THz}}, \tag{4.1}$$

where $\mathbf{E}_{\mathrm{pr}}$ is the optical probe field and $\mathbf{E}_{\mathrm{THz}} \equiv \mathbf{E}_{\mathrm{pu}}$ is the THz pump field, which can take on the value $\mathbf{E}_A(t)$, $\mathbf{E}_B(t)$ or $[\mathbf{E}_A(t) + \mathbf{E}_B(t)]$, depending on whether the 'A', 'B' or both THz pump pulses are applied to the sample.

Rediscovering that electro-optic detection can be viewed as a nonlinear process [19] was the main point of departure in moving away from the often-used intuitive perspective that the quasi static THz field induces a birefringence 'sensed' by the optical probe [45]. Guided by the work of others, in Chapter 3 we developed numerical methods that now allow us to simulate other nonlinear processes occurring in parallel or sequentially with the linear electro-optic effect. In particular, we followed a long line of publications starting with Bosshard et al. [4] who showed that, through optical rectification, an optical pump pulse can generate a surround-

ing static electric field that subsequently rotates the polarization of a co-propagating optical probe pulse via the electro-optic effect. Caumes et al. [10] extended this to include not only the static electric field, but also the THz-frequency field radiated by—and co-propagating with—this traveling static impulse. This co-propagating THz-frequency field also modifies the polarization of the optical probe pulse through the electro-optic effect, just as if electro-optic detection were occurring in parallel. Further, Cornet et al. [15] demonstrated that beginning with a THz (rather than optical) pump pulse is no less interesting, in that the electro-optic effect can rotate the polarization of an optical probe such that it cascades into a previously symmetry-forbidden second harmonic generation process.

With the foregoing in view, the present chapter focuses on the power of 2D THz-THz-polarimetry in discriminating between cascaded processes—such as those just discussed—and concomitant direct processes. As highlighted in Section 1.7, our 2D measurements contain a signal proportional to a product of the two THz pump fields $\mathbf{E}_A$ and $\mathbf{E}_B$. We suggested two possible contributions:

$$\text{Direct:} \quad \mathbf{P} = \epsilon_0 \chi^{(3)} \mathbf{E}_A \mathbf{E}_B \mathbf{E}_{\mathrm{pr}} \tag{4.2}$$

$$\text{Cascaded:} \quad \mathbf{P} = \epsilon_0 \chi^{(2)} \underbrace{\left[\chi^{(2)} \mathbf{E}_A \mathbf{E}_B \right]}_{\text{Reradiated}} \mathbf{E}_{\mathrm{pr}}. \tag{4.3}$$

The first contribution is a direct third-order process between the THz fields and the optical probe. The second contribution involves two cascaded second-order processes. In the first of the cascaded processes, the two THz pump fields directly mix and radiate product fields; in the second process, the product fields are detected by the optical probe. To distinguish between the direct and cascaded processes, we have taken a combined experimental and numerical approach.

In the first experiment, our fields are normally-incident on a $\langle 100 \rangle$-cut ('inactive') ZnTe crystal so that second-order ($\chi^{(2)}$) processes are symmetry-forbidden for all transverse polarizations. The resulting measurement acts as a reference for the signature of third-order ($\chi^{(3)}$) processes alone. These experimental results are complemented by a simulation where we have set $\chi^{(2)} = 0$ to confirm that third-order processes account for what we have measured.

In the second experiment, our fields are normally-incident on a $\langle 110 \rangle$-cut ('active') ZnTe crystal. In this case, the field polarizations are configured so that second-order processes are initially forbidden, but can be accessed by cascading from a primary third-order process. For this experiment, our simulations are particularly illuminating. The ability to separate THz-THz and THz-probe interactions allows us to determine that the cascaded second-order processes suggested in Eqn. (4.3) are existent, but negligible. In fact, all THz-THz nonlinear contributions are negligible with respect to the THz-probe contributions. However, we also find that there is still a significant cascaded second-order THz-probe contribution, not yet considered.

In the following, we will start by detailing how the reference THz waveforms used in our simulations were retrieved from the polarimetric measurements. These measurements were carried out at low field strengths, where a straightforward interpretation using the small field approximations for electro-optic detection [45] is acceptable. We also demonstrate the

limitations of this model at higher field strengths. Notably, the latter part is slightly tangential, so please bear with us. Subsequently, we calculate the polarization terms for ZnTe using the framework laid out for a general material in Section 3.2. These polarization terms are dependent on the crystal and field orientations, and we will discuss how we selected the orientations to achieve the desired suppression of $\chi^{(2)}$ processes for each experiment. Finally, we provide the experimental and numerical results in a side-by-side fashion, showing how cascaded and direct processes are plainly discriminated. We will offer possible explanations for the specific features in the nonlinear maps.

Finally, the experimental and numerical results will be provided in a side-by-side fashion, demonstrating how cascaded and direct processes are plainly discriminated. Possible explanations for the specific features in the nonlinear maps will be offered.

4.1 Reference Waveforms

For our simulations, it is crucial to have an accurate reference for the amplitude and shape of the THz electric field before it interacts with the ZnTe detection crystal. While accounting for linear dispersion and loss in the crystal is relatively straight forward, untangling nonlinearities post-measurement poses a significant challenge. To ensure a reliable reference in a regime where nonlinearities can be safely ignored, we recorded a series of waveforms using 0 to 10 attenuating silicon (Si) wafers before the detection crystal. In this way, we gain a greater context for the degree to which our 10-wafer measurement is linear. To minimize potential nonlinear effects introduced by the wafers themselves, we placed them in a collimated section of the beam path between the two $4\,\mathrm{in}$ off-axis parabolic mirrors shown in Fig. 2.1, where the field strengths are already several orders of magnitude lower.

The measurements were made using EO detection—a sub-variant of polarimetry—discussed in more detail in Section 2.4. The relevant operating parameters and material properties are listed in Tbl. 4.1. Throughout this section, we only discuss the 'AB' waveforms, with the pump delay τ equal to zero and both the A and B THz pulses temporally overlapped (reference Fig. 1.4). This configuration produces the maximum attainable electric field strength. However, the simultaneously acquired A and B waveforms are what we will use in our simulations. We oriented the $\langle 110 \rangle$ cut ZnTe detection crystal such that $\alpha_p = -45\,\mathrm{deg}$ and $\varphi_p = (\alpha_p - 90\,\mathrm{deg})$. The subscript p is used to indicate 'Planken' variables [45], as illustrated in Fig. 4.1. Note that this is not the typical orientation for EO detection where $\alpha_p = 90\,\mathrm{deg}$. Fig. 4.2 shows that the chosen angles place us near a local maximum in the detection efficiency at approximately $-28\,\mathrm{deg}$, but avoid the global maximum at $90\,\mathrm{deg}$ to further reduce nonlinearities (Note 4.1).

The resulting recordings of the normalized intensity modulation, $\Delta S = \Delta I / I_0$, are shown in Fig. 4.3(a). As the number of wafers decreases from 10, the waveform largely maintains the same shape, only flattening slightly where the peak modulation depth reaches a value of 0.444. However, beyond this threshold the waveform becomes highly structured, indicating a far-from-linear detection regime. The maximum theoretical modulation depth, $\Delta S_{\max}(\alpha_p, \varphi_p)$, depends on the orientation of the fields with respect to the crystal, but does

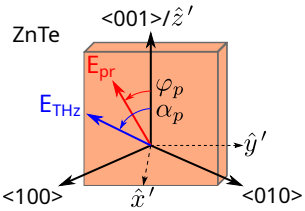

Figure 4.1. Definition of the crystal coordinate system used by Planken et al. [45]. The THz and NIR fields co-propagate along the $-\hat{x}'$ axis.

Table 4.1. Electro-optic detection parameters and material properties.

Parameter	Value	Parameter	Value
λ_{pr}	800 nm	ZnTe-cut	$\langle 110 \rangle$
ω_{pr}	$2\pi c/\lambda_{\mathrm{pr}}$	L	1.0 mm
n_{pr} [1]	2.85	r_{41} [2]	$-2.72\,\mathrm{pm/V}$

[1] [36]
[2] [10, 54], see Note 4.5

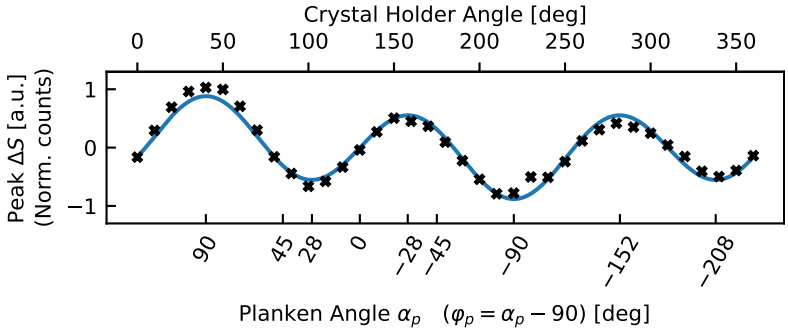

Figure 4.2. Calibration of the ZnTe crystal holder angle. The measured modulation depths ΔS at a fixed delay (black crosses, normalized to 1), are fit with the small-field approximation Eqn. (4.4) (blue), assuming $\varphi_p = (\alpha_p - 90\,\mathrm{deg})$. In this way we are able to determine the absolute angle of our fields with respect to the $\langle 001 \rangle$ axis of the ZnTe crystal. See Note 4.2 for more details.

Note 4.1 ZnTe Orientation

Typically, we will be operating at $\alpha_p = 90\,\mathrm{deg}$ and $\varphi_p = (\alpha_p - 90\,\mathrm{deg})$. This is the global maximum of the EO detection efficiency, as show in Fig. 4.2. Fortunately, in the *small-field* detection regime, the relative field/crystal orientations about the $\hat{x}'$ axis affect only the amplitude, not the shape of the THz waveform. The latter only depends on the dispersion of both the refractive index n_{pr} in the near-infrared (NIR) range and the electro-optic coefficient r_{41} [45].

Note 4.2 Crystal Holder Calibration

The crystal holder angle was calibrated by recording the modulation depth ΔS at a fixed delay for several crystal angles, and subsequently fitting the data with the small-field approximation [45]

$$\Delta S(\alpha_p, \varphi_p) \approx \frac{\omega_{\mathrm{pr}} n_{\mathrm{pr}}^3 E_{\mathrm{THz}} r_{41} L}{2c} (\cos\alpha_p \sin 2\varphi_p + 2\sin\alpha_p \cos 2\varphi_p). \tag{4.4}$$

The results are shown in Fig. 4.1. To ensure the validity of this approximation, the field was attenuated with a pair of wire-grid polarizes. The polarizers were set such that the attenuation factor was 0.087—equivalent to ~ 7 Si wafers.

not exceed 1. This limit is apparent upon inspecting the modulation equation [45]:

$$\Delta S(\alpha_p, \varphi_p) = \sin[2(\varphi_p - \theta_p)] \sin\left\{\frac{\omega_{\mathrm{pr}}}{c}[n_y(\alpha_p) - n_z(\alpha_p)]L\right\}. \tag{4.5}$$

In Eqn. (4.5), we observe that the modulation depth is proportional to the product of two sine functions. The argument of the leading sine only contains geometric parameters φ_p and θ_p. The later parameter, θ_p, represents the rotation angle of the index ellipsoid's principal axes about $\hat{x}'$ and is related to α_p by [45]

$$2\theta_p = -\arctan(2\tan\alpha_p) - n\pi, \tag{4.6}$$
$$\left(n - \frac{1}{2}\right)\pi \le \alpha_p < \left(n + \frac{1}{2}\right)\pi, \qquad n = 0, 1, \ldots.$$

Using these relations, we find that the leading sine reduces to 1 when $\alpha_p = 90\,\mathrm{deg}$ and $\varphi_p = (\alpha_p - 90\,\mathrm{deg})$, which corresponds to the maximum detection efficiency. However, if we maintain the relationship between φ_p and α_p but set $\alpha_p = -45\,\mathrm{deg}$, the leading sine sets the limit $\Delta S_{\max} \approx 0.447$. Indeed, in Fig. 4.3(a), we observe a peak modulation depth of approximately 0.444, which is close to this theoretical limit. The influence of the second sine-function in Eqn. (4.5) is more clearly seen in Fig. 4.3(c), where we have extracted the peak modulation depth as a function of the total attenuation factor γ (Note 4.3)—in effect, the incident THz field strength. We fit these peaks with a phenomenological sine function having γ in the argument. The excellent agreement demonstrates that, for large fields, the measured modulation ΔS deviates far from the linear approximation in Eqn. (4.4) and is instead nearly sinusoidal.

We can retrieve the THz field strength in absolute units by using a small-field approximation (Note 4.4) for the principal refractive indices, as given by [45]:

$$n_y(\alpha_p) \approx n_{\mathrm{pr}} + \frac{n_{\mathrm{pr}}^3}{2} E_{\mathrm{THz}} r_{41} [\cos\alpha_p \sin^2\theta_p + \cos(\alpha_p + 2\theta_p)], \tag{4.7}$$
$$n_z(\alpha_p) \approx n_{\mathrm{pr}} + \frac{n_{\mathrm{pr}}^3}{2} E_{\mathrm{THz}} r_{41} [\cos\alpha_p \cos^2\theta_p - \cos(\alpha_p + 2\theta_p)].$$

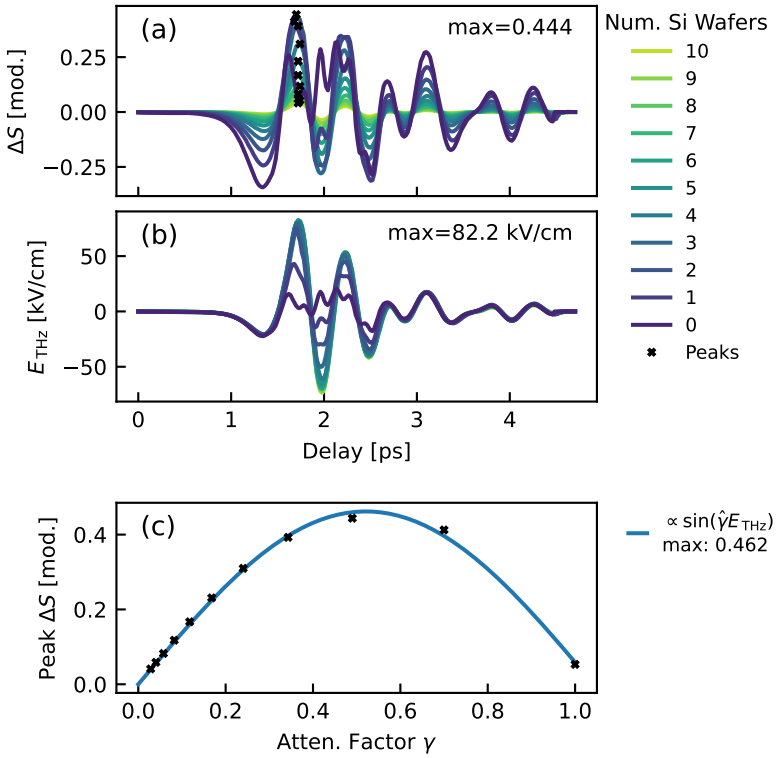

Figure 4.3. Measured field-strength dependence of EO-detection for $\alpha_p = -45\,\mathrm{deg}$ and $\varphi_p = (\alpha_p - 90\,\mathrm{deg})$. Silicon (Si) wafers are used to attenuate the field. Relevant operating parameters and material properties are found in Tbl. 4.1. (a) The measured modulation depth (fraction of 1). At higher field strengths ΔS is highly structured and no longer approaches the theoretical maximum of 0.447. (b) Field strength retrieved from ΔS using Eqn. (4.8). Similarly to (a), the apparent field strength is lower with less attenuation. (c) The peak modulation depth in (a) is fit with a phenomenological sine function having E_{THz} in the argument. The factor $\hat{\gamma}$ accounts for material properties and the attenuation factor (Note 4.3).

Note 4.3 Si Wafer Attenuation

Each Si wafer imparts an attenuation factor of 0.701, which accounts for reflection losses at the front and rear surface assuming a constant refractive index $n_{\mathrm{Si}} = 3.417$ and no absorption in the material [16]. The total attenuation for a series of wafers is then $\gamma = 0.701^{N_w}$, where N_w is the number of Si wafers.
Coincidentally, the factor of 0.701 is the same as the power transmission coefficient T for a single air/Si interface. This is because $T = |t||t|$, where $|t|$ is the magnitude of the complex amplitude transmission coefficient for a single interface, and for each wafer we have two interfaces.

Inserting these relations into Eqn. 4.5 and simplifying the trigonometric expressions yields:

$$\Delta S(\alpha_p, \varphi_p) \approx \sin[2(\varphi_p - \theta_p)] \sin\left\{\frac{\omega_{\mathrm{pr}} n_{\mathrm{pr}}^3 E_{\mathrm{THz}} r_{41} L}{2c}(\cos\alpha_p \cos 2\theta_p - 2\sin\alpha_p \sin 2\theta_p)\right\}. \quad (4.8)$$

As previously noted, the leading sine term determines the maximum modulation depth, $\Delta S_{\max}$. We have calculated its value for two different scenarios: the current geometry with $\alpha_p = -45\,\mathrm{deg}$, and the configuration that maximizes detection efficiency with $\alpha_p = 90\,\mathrm{deg}$. Again, for all cases considered $\varphi_p = (\alpha_p - 90\,\mathrm{deg})$. The results are as follows:

$$\Delta S_{\max} = \sin[2(\varphi_p - \theta_p)] \approx \begin{cases} 0.447, & \alpha_p = -45\,\mathrm{deg} \\ 1, & \alpha_p = 90\,\mathrm{deg} \end{cases}. \quad (4.9)$$

The respective inner geometric terms in the second sine are:

$$(\cos\alpha_p \cos 2\theta_p - 2\sin\alpha_p \sin 2\theta_p) \approx \begin{cases} 1.58, & \alpha_p = -45\,\mathrm{deg} \\ 2, & \alpha_p = 90\,\mathrm{deg} \end{cases}. \quad (4.10)$$

Note 4.4 Small-Field Approximation

The small-field approximation made in Eqn. (4.7) is quite different from that used to derive Eqn. (4.4). The sinusoidal nature of the polarimetric measurement described by Eqn. (4.5) is not inherently field dependent, but rather has to do with the 2π cyclicity of phase. For example, when two half-wave plates are stacked consecutively, the total retardation amounts to a full-wave, which, for sinusoidal signals, acts as an identity operator. In other words, the signal comes back on itself after a 2π phase retardation, just like the sine function. By considering the argument in Eqn. (4.5) to be small, we are assuming the phase retardation is small. Although this assumption often holds true for small fields, it is still possible to detect a seemingly "nonlinear" signal even for a small field if the crystal length, L, is large.

These calculations reveal that 'detuning' the crystal away from the maximum detection efficiency angle ($\alpha_p = 90\,\mathrm{deg}$) reduces the attainable modulation depth, as well as the rate of modulation through the argument in the second sine. Solving Eqn. (4.8) for E_{THz}, and dividing by the attenuation factor γ due to the Si wafers, allows us to recover the electric field before attenuation and detection [Fig. 4.3(b)] from the modulation depths [Fig. 4.3(a)].The parameters and material properties used for the calculations are listed in Table 4.1. The recovered peak field strength when using 10 Si wafers before the detection crystal is $82.2\,\mathrm{kV/cm}$. When only one or two attenuating wafers are used, it is no longer possible to recover the field. In fact, at these high field strengths, the deeply structured waveforms appear to have a lower peak field strength.

A lower recovered peak field strength is to be expected outside the small-field limit, but it is intriguing that the waveforms never reach the maximum modulation depth in Fig. 4.3(a). To understand this, consider again Eqn. 4.8. The second sine term is periodic in the field strength E_{THz}, reaching a maximum value when the argument is equal to $\pi/2$, which occurs when

$$\pi/2 \approx 1.58 \frac{\omega_{\mathrm{pr}} n_{\mathrm{pr}}^3 E_{\mathrm{THz}} r_{41} L}{2c} \tag{4.11}$$

$$\therefore E_{\mathrm{THz}} \approx 40\,\mathrm{kV/cm}. \tag{4.12}$$

At this field strength we reach $\Delta S_{\max}$, and what is called the 'over-rotation' point—the point at which larger field strengths lead to smaller modulations. However, fields exceeding this point should always reach $\Delta S_{\max}$ before decreasing again (perhaps multiple times if the field strength is great enough, since a sine function is cyclic). Instead, in Fig. 4.3(a) we only see a highly structured region reaching approximately $3/4$ of $\Delta S_{\max}$. The expected behavior is shown in Fig. 4.4, where we have used Eqn. (4.8) to calculate the theoretical ΔS signal for the 10-wafer reference waveform with a peak field strength of $82.2\,\mathrm{kV/cm}$ (Bell and Hilke [3, Fig. 7(b)] have reported similar results). The leading positive peak in Fig. 4.4(a) is essentially cut and mirrored about $\Delta S_{\max} \approx 0.447$. The same behavior is seen in Fig. 4.4(b) where we have retrieved the waveform in absolute units, except the field turns at the over-rotation point, $E_{\mathrm{THz}} \approx 40\,\mathrm{kV/cm}$.

It is perhaps not entirely surprising that Eqn. (4.8) does not hold up at high field strengths given the small-field approximation made in Eqn. (4.7). However, we now have our first opportunity to test if the numerical pulse propagation methods developed in Chapter 3 more accurately represent what we see in these measurements. As an input to the simulation, we again use the electric field retrieved from the reference measurement taken with 10 attenuating Si wafers and having a peak field strength of $82.2\,\mathrm{kV/cm}$ [Fig. 4.3(b)]. Note that this is the same field we will soon use for modeling direct and cascaded nonlinearities in Section 4.3. Overall, we are pleased to see a generally good agreement between the simulation results in Fig. 4.5 and the measured data in Fig. 4.3. The ripples preceding the pulse in the simulation are due to the deconvolution process used to account for dispersion and loss in the ZnTe crystal (see Section 3.3). We unfortunately have not had time to adequately analyze these results, however, we hypothesize that the inability of Eqn. (4.8) to account for the behavior at high field strengths stems from neglecting dispersion and third-order nonlinearities. We

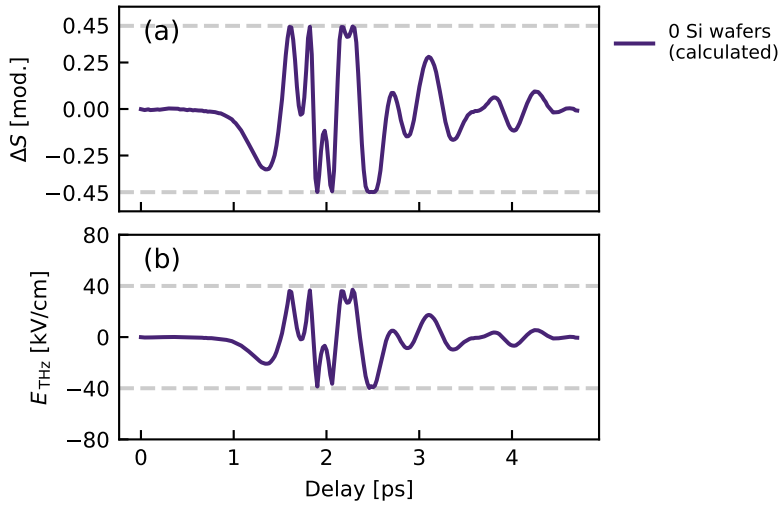

Figure 4.4. Theoretical waveforms for the unattenuated (0 silicon [Si] wafers) electric field calculated with Eqn. 4.8. As input, we used the electric field retrieved from the reference measurement taken with 10 attenuating Si wafers, having a peak field strength of $82.2\,\mathrm{kV/cm}$ [Fig. 4.3(b)]. The EO detection parameters are listed in Table 4.1. In (a) we see the modulation depth reaches the theoretical maximum of 0.447. The peak of the pulse is essentially cutoff and flipped across this limit. In (b) we have inverted Eqn. (4.8) to find E_{THz} from the calculated values of ΔS. Because $\arcsin$ is only defined on $[-\pi/2, \pi/2]$, the recovered field similarly is clipped at the over-rotation point $E_{\mathrm{THz}} \approx 40\,\mathrm{kV/cm}$.

have previously found that when only second-order THz-probe nonlinearities are considered in our simulations, they are visually indistinguishable from the Planken model [Eqn. (4.8)] up to a field strength of at least $44\,\mathrm{kV/cm}$

We repeated these simulations but rotated the crystal such that $\alpha_p = 90\,\mathrm{deg}$, maximizing the detection efficiency. The results are presented in Fig. 4.6. In panel (a), the modulation depth approaches 1, as expected from Eqn. (4.9). For high levels of attenuation, both the simulation with $\alpha_p = -45\,\mathrm{deg}$ and $\alpha_p = 90\,\mathrm{deg}$ yield a peak field strength of $85.4\,\mathrm{kV/cm}$ (*cf.* Fig. 4.5(b) and Fig. 4.6(b)). However, noticeable differences in the retrieved fields emerge at lower levels of attenuation. Although further investigation is required, it is worth noting that the assertion by Planken et al. [45] regarding the waveform's structure being independent of crystal angle appears to be limited to the small-field regime (as considered by them).

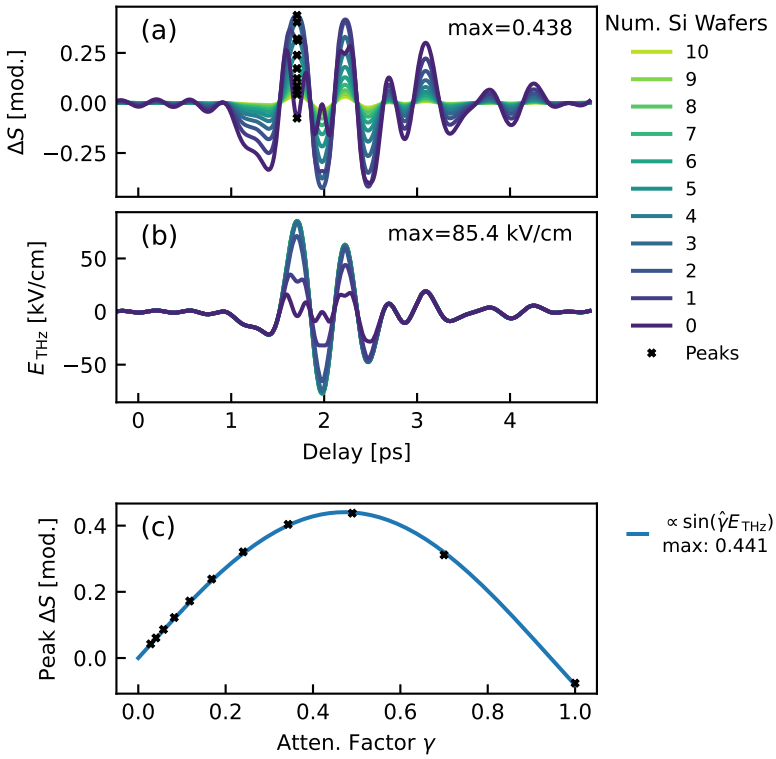

Figure 4.5. Simulated field-strength dependence of EO-detection for $\alpha_p = -45\,\mathrm{deg}$. All parameters/properties match those used in the measurements in Fig. 4.3. We used the electric field retrieved from the reference measurement taken with 10 attenuating silicon (Si) wafers as the input (Fig. 4.3(b), $82.2\,\mathrm{kV/cm}$ peak). (a) The simulated modulation depth (fraction of 1). (b) Field strength retrieved from ΔS using Eqn. (4.8). (c) The peak modulation depth in (a) fit with a phenomenological sine function having E_{THz} in the argument. The factor $\hat{\gamma}$ accounts for material properties and the attenuation factor (Note 4.3). Generally, the simulations match the behavior seen in the measurements.

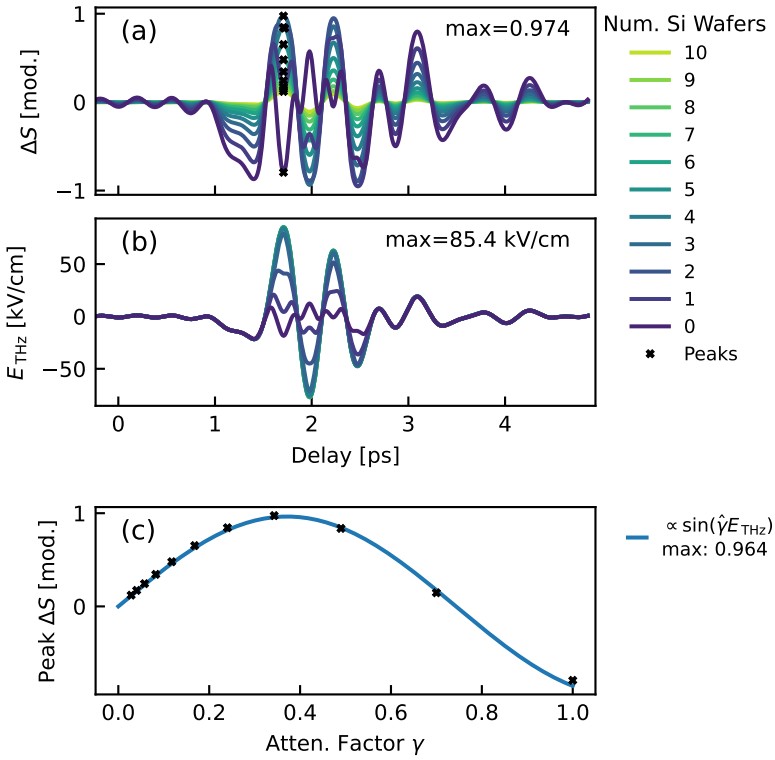

Figure 4.6. Simulated field-strength dependence of EO-detection for $\alpha_p = 90\,\mathrm{deg}$. All other parameters/properties match those used in the measurements in Fig. 4.3. We used the electric field retrieved from the reference measurement taken with 10 attenuating silicon (Si) wafers as the input (Fig. 4.3(b), $82.2\,\mathrm{kV/cm}$ peak). (a) The simulated modulation depth (fraction of 1). With $\alpha_p = 90\,\mathrm{deg}$ the detection efficiency is enhanced and ΔS approaches the theoretical maximum of 1. (b) Field strength retrieved from ΔS using Eqn. (4.8). (c) The peak modulation depth in (a) is fit with a phenomenological sine function having E_{THz} in the argument. The factor $\hat{\gamma}$ accounts for material properties and the attenuation factor (Note 4.3). For high attenuation (small-fields) the simulation is similar to that for $\alpha_p = -45\,\mathrm{deg}$ (Fig. 4.5). At higher fields, the structure of the waveforms is not independent of α_p.

4.2 ZnTe Polarization Terms

In Section 3.2 we calculated the second- and third-order polarizations generally for any material. In this section, we will use the crystal-symmetries of ZnTe and our knowledge of the fields to narrow down the relevant contributions. ZnTe is a cubic crystal with a $\bar{4}3m$ point-group. Assuming Kleinman symmetry (Note 4.5), the only non-zero elements of $\chi^{(2)}_{ijk}$ are [7, p.47]:

$$ijk \in \{XYZ = XZY = YZX = YXZ = ZXY = ZYX\},$$

where capital X, Y, Z denote crystallographic axes, and all elements have the same value of $\bar{\chi}^{(2)} = 90 \times 10^{-12}\,\mathrm{m/V}$ [10]. For $\chi^{(3)}_{ijkl}$, there are four independent terms following the relationships [7, p.53]:

$$\begin{aligned} ijkl \in \{&a = XXXX = YYYY = ZZZZ,\\ &b = YYZZ = ZZYY = ZZXX = XXZZ = XXYY = YYXX,\\ &b = YZYZ = ZYZY = ZXZX = XZXZ = XYXY = YXYX,\\ &b = YZZY = ZYYZ = ZXXZ = XZZX = XYYX = YXXY\}, \end{aligned}$$

where $a = 3 \times 10^{-19}\,\mathrm{m^2/V^2}$ and $b = a/1.9$ [10]. To be clear, these tensor elements are

Note 4.5 Kleinman Symmetry

Kleinman symmetry is valid whenever dispersion (and by extension via the Kramers–Kronig relations, absorption) of the susceptibility can be neglected and allows us to freely permute the indices of the susceptibility tensors [7]. It is often valid for optical frequencies in the NIR and visible ranges, far from ionic and electronic resonances [6, 7]. However, for the THz frequencies considered herein, Kleinman symmetry is a poor approximation given the large TO phonon at $5.32\,\mathrm{THz}$, and the smaller, yet broad, second-order phonon absorption bands around $1.6\,\mathrm{THz}$ and $3.7\,\mathrm{THz}$ [20, 48]. Lack of Kleinman symmetry is plainly evident in the disparity between the optical susceptibility $\bar{\chi}^{(2)} = 90 \times 10^{-12}\,\mathrm{m/V}$ [10] and the electro-optic coefficient $r_{41} = 3.9\,\mathrm{pm/V}$ [3], which can be converted to a susceptibility with the relation [6]

$$2\chi^{(2)}_{ijk} = d_{ijk} = -\frac{1}{4} n_i^2 n_j^2 r_{ijk}, \tag{4.13}$$

where in any system of units $\chi^{(2)} = 2d$ by convention [7, p.50]. Using this relation, we find $\bar{\chi}^{(2)}_{r41} \approx -130 \times 10^{-12}\,\mathrm{m/V}$, a factor of -1.4 times $\bar{\chi}^{(2)}$. The author admits he does not understand the significance of the sign change, but it results from a Taylor expansion of the optical indicatrix [5, 54].

in the *crystal* reference frame (X, Y, Z), whereas our fields are defined in the *lab/simulation* reference frame $(\hat{x}, \hat{y}, \hat{z})$. To move between the two, we use the rotation matrix $\mathrm{R}(\phi, \theta)$, which

rotates the crystal by an angle ϕ about the $\hat{z}$ axis, *then* by an angle θ about the $\hat{x}$ axis. The order and direction of the rotations is important. The direction is defined in Fig. 4.7 and follows the 'right-hand-rule'.

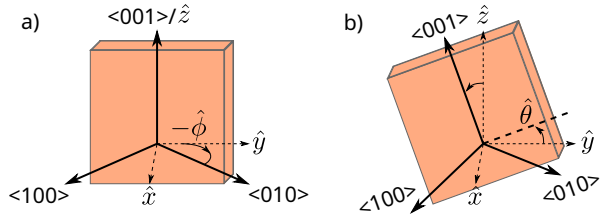

Figure 4.7. Definition of the crystal rotation angles used in the simulations. Angle brackets $\langle XYZ \rangle$ denote crystallographic axes; lab/simulation-frame axes are indicated by $\hat{x}, \hat{y}, \hat{z}$. The crystal- and lab-frames are initially coincident. (a) The crystal is first rotated about the $\hat{z}$ axis by angle ϕ, (b) and then about the $\hat{x}$ by angle θ. The order and direction are important. Note that the illustrated ϕ-rotation is in the negative direction, and that both ϕ and θ are defined with respect to the $\hat{y}$ axis.

In addition to the orientation of the crystal in the lab-frame, we can judiciously set the polarization of the electric fields to eliminate alternative confounding contributions to the total nonlinear-polarization. We will first only describe the purpose of our selected polarizations, then follow up with calculations of the polarization terms to justify the choices. In Fig. 4.8 the three crystal-field configurations considered in our study are illustrated. In all cases, the optical probe ($\mathbf{E}_{\mathrm{pr}}$) and THz pump ($\mathbf{E}_{\mathrm{pu}}$) fields co-propagate down the $\hat{x}$ axis. Panel (a) shows 'inactive' $\langle 100 \rangle$ cut ZnTe. The name refers to the lack of a detectable electro-optic effect—a $\chi^{(2)}$ process—for fields polarized in the cut-plane. In fact, all in-plane $\chi^{(2)}$ processes are symmetry-forbidden in this configuration, and this property will allow us to measure the signature of $\chi^{(3)}$ processes alone (Note 4.6).

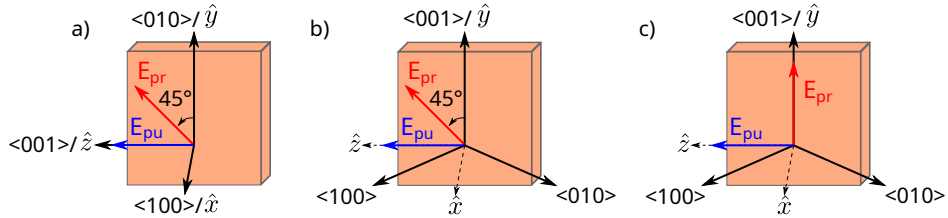

Figure 4.8. ZnTe crystal and field orientations used in the experiments and simulations. See Fig. 4.7 for axis and angle definitions. (a) 'Inactive' $\langle 100 \rangle$ cut, rotation angles $\phi = 0\,\mathrm{deg}$ and $\theta = 0\,\mathrm{deg}$. (b) 'Active' $\langle 110 \rangle$ cut, rotation angles $\phi = -45\,\mathrm{deg}$ and $\theta = -90\,\mathrm{deg}$. Probed such that $\chi^{(2)}$ processes cancel. (c) 'Active' $\langle 110 \rangle$ cut, rotation angles $\phi = -45\,\mathrm{deg}$ and $\theta = -90\,\mathrm{deg}$. Probed such that $\chi^{(2)}$ processes are maximally imbalanced. (a, b, c) The THz polarization angle, θ_{pu}, is $90\,\mathrm{def}$ in all cases. (a, b) The optical probe polarization angle, θ_{pr}, is $45\,\mathrm{def}$, and (c) $0\,\mathrm{def}$. The polarization angles are defined like the crystal angle θ.

Although we can freely choose any in-plane polarizations for $\mathbf{E}_{\mathrm{pr}}$ and $\mathbf{E}_{\mathrm{pu}}$ in the $\langle 100 \rangle$ cut crystal, they are strategically chosen for the second half of the experiment in panel (b),

Note 4.6 'Inactive' ZnTe

Recall, a major assumption we made when deriving the FME and NLSE equations (Section 3.1) was that the longitudinal ($\hat{x}$) components of the fields are negligible in comparison to the transverse ($\hat{y}, \hat{z}$) components. This immediately shows why the $\langle 100 \rangle$ cut ZnTe, depicted in Fig. 4.8(a), is called 'inactive': all second-order tensor elements with $j, k = X$ are zero, and the remaining elements XYZ and XZY only produce a polarization in the $X = \hat{x}$ direction. Radiation from a polarization in $\hat{x}$ does not propagate in the $\hat{x}$ direction, so it will not be detectable after the crystal. Furthermore, since the radiated field does not co-propagate in the crystal, cascaded effects are likely negligible—this assumption appears to bear out in the experiments discussed later in Section 4.3. In order to create a detectable second-order polarization and make the crystal 'active', we need to reorient the crystal and electric fields.

where the crystal has been rotated and cut along the $\langle 110 \rangle$ plane making it 'active'. With $\mathbf{E}_{\mathrm{pr}} = 45\,\mathrm{deg}$ and $\mathbf{E}_{\mathrm{pu}} = 90\,\mathrm{deg}$, $\chi^{(2)}$ processes are perfectly balanced in opposition, and do not alter the polarization of the probe. To be clear, $\chi^{(2)}$ processes still occur (and likely shift the spectrum of the probe [19, 31]), but they do not influence the signal measured with polarimetry. Polarimetry will only detect a $\chi^{(2)}$ process if it cascades from a primary $\chi^{(3)}$ process. The primary $\chi^{(3)}$ process can be said to break the equilibrium between the two opposing $\chi^{(2)}$ processes. Therefore, a difference in the signal measured between configurations (a) and (b) is evidence towards a cascaded process.

While somewhat tangential to the main experiment, panel (c) shows a typical configuration for electro-optic detection [45], as used in Section 4.1 to record reference waveforms of the THz electric fields. To Transition from panel (b) to (c), we rotated the probe to $0\,\mathrm{deg}$, purposefully maximizing the imbalance between the $\chi^{(2)}$ processes. We previously presented our repetition of the angle-dependent measurements performed by Planken et al. [45] in Fig. 4.2, and reconfirmed that the configuration in panel (c) yields the greatest detection efficiency. This outcome aligns with the predictions made by their small-field index-ellipsoid model; in the following, we provide an alternative argument based on the second-order polarization terms.

To calculate the polarization terms, we first need to project the electric fields, $\mathbf{E}$, from the lab-frame into the crystal-frame with the rotation operator $R(\phi, \theta)$. Recall, the nonlinear tensor χ is defined in the crystal-frame X, Y, Z, not the lab-frame $\hat{x}, \hat{y}, \hat{z}$. Afterwards, to find the nonlinear polarization in the lab-frame, $\mathbf{P}$, we project out of the crystal frame with the inverse operator $R(\phi, \theta)^{-1}$. This procedure can be written as

$$\mathbf{P} = \epsilon_0 R(\phi, \theta)^{-1} \chi R(\phi, \theta) \mathbf{E}. \tag{4.14}$$

The total operator $\left[\epsilon_0 R(\phi, \theta)^{-1} \chi R(\phi, \theta)\right]$, for $\langle 110 \rangle$ and $\langle 100 \rangle$ cut crystals assuming negligible longitudinal field components E_{pr_x} and E_{pu_x}, is provided in Appendix A. For the

second-order THz-Probe polarizations, Eqn. (4.14) takes the form

$$\begin{bmatrix} P^{(2)}_{\mathrm{pr}_x} \\ P^{(2)}_{\mathrm{pr}_y} \\ P^{(2)}_{\mathrm{pr}_z} \end{bmatrix} = \epsilon_0 \mathrm{R}(\phi,\theta)^{-1} \chi^{(2)} \mathrm{R}(\phi,\theta) \begin{bmatrix} E_{\mathrm{pr}_y} E_{\mathrm{pu}_y} \\ E_{\mathrm{pr}_y} E_{\mathrm{pu}_z} \\ E_{\mathrm{pr}_z} E_{\mathrm{pu}_y} \\ E_{\mathrm{pr}_z} E_{\mathrm{pu}_z} \end{bmatrix}. \tag{4.15}$$

For a $\langle 110 \rangle$ cut crystal, $\phi = -45\,\mathrm{deg}$, and in both configurations (b) and (c) in Fig. 4.8, $\theta = -90\,\mathrm{deg}$. In these cases, Eqn. (4.15) reduces to

$$\begin{bmatrix} P^{(2)}_{\mathrm{pr}_x} \\ P^{(2)}_{\mathrm{pr}_y} \\ P^{(2)}_{\mathrm{pr}_z} \end{bmatrix} = 2\epsilon_0 \bar{\chi}^{(2)} \begin{bmatrix} 0 \\ -E_{\mathrm{pr}_z} E_{\mathrm{pu}_z} \\ -E_{\mathrm{pr}_y} E_{\mathrm{pu}_z} - \cancel{E_{\mathrm{pr}_z} E_{\mathrm{pu}_y}} \end{bmatrix}. \tag{4.16}$$

We have canceled the field term with E_{pu_y} because the THz pump polarization angle at the front surface of the crystal is $\theta_{\mathrm{pu}} = 90\,\mathrm{deg}$—in other words, entirely $\hat{z}$-polarized. This could, however, change when the fields propagate through the crystal, but for now we are only making an argument based on the prevailing initial condition. In Fig. 4.9 we have plotted the in-plane components of this polarization, $P^{(2)}_{\mathrm{pr}_y}$ and $P^{(2)}_{\mathrm{pr}_z}$. The $\mathbf{E}_{\mathrm{pu}}$ and $\mathbf{E}_{\mathrm{pr}}$ field strengths have been normalized to 1, thus the in-plane components are:

$$E_{\mathrm{pu}_z} = 1, \quad E_{\mathrm{pr}_y} = \cos(\theta_{\mathrm{pr}}), \text{ and } E_{\mathrm{pr}_z} = \sin(\theta_{\mathrm{pr}}). \tag{4.17}$$

Considering we are making a polarimetric measurement, what we are really interested in is the rate at which the probe polarization changes in the crystal. There are two ways the probe polarization can be modified: (1) $\hat{y}$-polarized photons are converted to $\hat{z}$-polarized photons, and vice versa; (2) $\hat{y}$-polarized photons are retarded with respect to $\hat{z}$-polarized photons, and vice versa. The first process is associated with polarization terms that are orthogonal to the constituent probe electric field component. These are terms with the form $P_{\mathrm{pr}_j} \propto E_{\mathrm{pr}_i}$ and $j \neq i$. The second process results from the parallelly-polarized terms with $j = i$. In this second process, one can imagine the radiation from an induced-polarization as virtually-absorbed and re-emitted photons—the momentary absorption imparts a small delay in time. Alternatively, causality requires the induced polarization to occur after the electric field has arrived, so the radiated field must be delayed with respect to the generating field.

The second-order polarization we are considering here [Eqn. (4.16)] initially only contains 'cross-polarized' terms, with $j \neq i$. To approximate the rate of the polarization change, we calculate the magnitude-squared difference, $\Delta|i \neq j|$, between conversion from $\hat{y}$ to $\hat{z}$ polarized photons ($\hat{y} \rightarrow \hat{z}$) and $\hat{z}$ to $\hat{y}$ polarized photons ($\hat{z} \rightarrow \hat{y}$). Explicitly,

$$\Delta|i \neq j| = |P_{\mathrm{pr}_y}|^2 - |P_{\mathrm{pr}_z}|^2 \tag{4.18}$$

$$= |-E_{\mathrm{pr}_z} E_{\mathrm{pu}_z}|^2 - |-E_{\mathrm{pr}_y} E_{\mathrm{pu}_z}|^2. \tag{4.19}$$

Inspecting $\Delta|i \neq j|$ as a function of θ_{pr} in Fig. 4.9(a), we see it is peaked at $\theta_{\mathrm{pr}} = 0\,\mathrm{deg}$ (configuration (c) in Fig. 4.8) and $\theta_{\mathrm{pr}} = 90\,\mathrm{deg}$. These angles maximize the polarization modulation rate of the probe, which aligns with the prediction of the small-field index-ellipsoid

model (Section 4.1 and [45]). Importantly, Fig. 4.9(a) also shows that the second-order modulation rate is zero for $\theta_{\mathrm{pr}} = 45\,\mathrm{deg}$. At this angle, the $\chi^{(2)}$ processes are in equilibrium. This is what we desired for configuration (b) in Fig. 4.8, where second-order processes should only produce a measurable effect if cascading from a primary third-order process breaks the equilibrium.

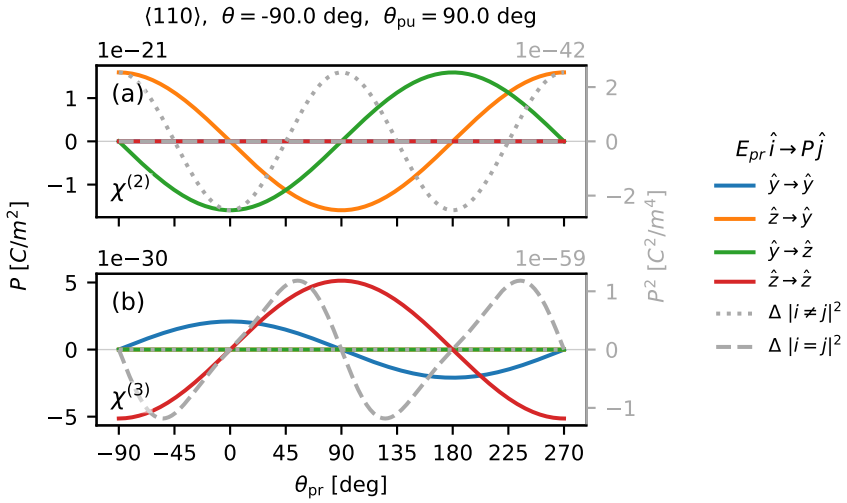

Figure 4.9. Second- and third-order nonlinear polarization terms in $\langle 110 \rangle$ cut ZnTe as a function of the probe polarization angle θ_{pr}. The crystal angle, θ, is $-90\,\mathrm{deg}$, and the THz pump polarization angle, θ_{pu}, is $90\,\mathrm{deg}$. See Fig. 4.7 for angle definitions. The curves show the nonlinear polarization terms $P_{\mathrm{pr}_j} \propto E_{\mathrm{pr}_i}$. 'Orthogonal' terms with $j \neq i$, and 'parallel' terms with $j = i$ are grouped separately. $\Delta|i \neq j|$ is the magnitude-squared difference of the $\hat{z} \to \hat{y}$ and $\hat{y} \to \hat{z}$ terms. $\Delta|i = j|$ is the magnitude-squared difference of the $\hat{y} \to \hat{y}$ and $\hat{z} \to \hat{z}$ terms in a rotated frame fixed at a $45\,\mathrm{deg}$ angle to the probe (see text for details). (a) Second-order ($\chi^{(2)}$) nonlinear polarization terms. Both $i = j$ terms are zero. (b) Third-order ($\chi^{(3)}$) nonlinear polarization terms. Both $i \neq j$ terms are zero.

We can apply a similar analysis for the third-order polarization terms that we selectively prioritize in configuration (b) (Fig. 4.8). At the front-face of the $\langle 110 \rangle$ cut crystal, we have

$$\begin{bmatrix} P^{(3)}_{\mathrm{pr}_x} \\ P^{(3)}_{\mathrm{pr}_y} \\ P^{(3)}_{\mathrm{pr}_z} \end{bmatrix} = \frac{3\epsilon_0}{2} \begin{bmatrix} 0 \\ 2bE_{\mathrm{pr}_y} E^2_{\mathrm{pu}_z} \\ (a+3b)E_{\mathrm{pr}_z} E^2_{\mathrm{pu}_z} \end{bmatrix}. \tag{4.20}$$

Notice that these are 'parallel-polarized' terms with $j = i$, rather than 'cross-polarized' terms with $j \neq i$. Again, with $P_{\mathrm{pr}_j} \propto E_{\mathrm{pr}_i}$, there is an in-plane effective retardation of the probe that is proportional to the nonlinear polarization magnitude. If the nonlinear polarization in $\hat{y}$ and $\hat{z}$ is not the same, then the material is essentially birefringent and acts as a waveplate. From this perspective, the change in the probe's polarization depends on both the magnitude of the birefringence *and* the orientation of the 'fast' (less retardation) and 'slow' (more retardation) axes of the waveplate with respect to the probe. For example, if the probe is entirely

polarized along either the slow or fast axis then, regardless the magnitude of the birefringence, there will be no change in the probe's polarization, because *all* the components either travel 'slow' or 'fast'—we need part of the probe to travel faster than the other to produce a phase difference that changes its polarization (see [13] for a refresher on waveplates). Therefore, rather than calculating the magnitude-squared difference of the nonlinear polarization along the $\hat{y}$ and $\hat{z}$ axes, like we did for $\Delta|i \neq j|$, we will first transform the polarizations to a rotated coordinate frame ($\hat{y} \rightarrow \hat{y}'$, $\hat{z} \rightarrow \hat{z}'$) where the magnitude of the probe is equal on both axes. This is like passing a waveplate at $45\,\mathrm{deg}$ to the fast or slow axis, and will produce the maximum polarization change. The polarization in the rotated frame is

$$(P'_{\mathrm{pr}_y}, P'_{\mathrm{pr}_z}) = R(-\theta_{\mathrm{pr}} - 45^\circ)(P_{\mathrm{pr}_y}, P_{\mathrm{pr}_z}), \tag{4.21}$$

where $R(-\theta_{\mathrm{pr}} - 45^\circ)$ projects to a coordinate frame angled at $45\,\mathrm{deg}$ to the probe. The magnitude-squared difference of the 'parallel-polarized' terms ($i = j$) in the rotated frame is

$$\Delta|i = j| = |P'_{\mathrm{pr}_y}|^2 - |P'_{\mathrm{pr}_z}|^2. \tag{4.22}$$

In Fig. 4.9(b), $\Delta|i = j|$ is plotted as a function of θ_{pr}. We see the function is peaked at $\theta_{\mathrm{pr}} \approx \pm 45\,\mathrm{deg}$. Conveniently, this is the same angle that balances the second-order processes in configuration (b) (Fig. 4.8). Operating near the maximum of $\Delta|i = j|$ provides a better chance of detecting $\chi^{(3)}$ processes, which are on the order of $1e^{-9}$ times weaker than competing $\chi^{(2)}$ processes (compare the amplitudes in Fig 4.9).

It is not a coincidence that the maximum of $\Delta|i = j|$ occurs when the probe is at approximately $\pm 45\,\mathrm{deg}$ to the THz pump field—the THz field modifies the refractive index in what is called the 'Terahertz Kerr effect' [18], which has been demonstrated in liquids [27] and our material of interest ZnTe [14]. A keen observer will notice that the peaks of $\Delta|i = j|$ are slightly shifted from $45\,\mathrm{deg}$ towards $90\,\mathrm{deg}$. We believe this is because the nonlinear-polarization, and hence the magnitude of the birefringence, also depends on the field strength of the probe. When the probe and THz pump fields are aligned, it increases the birefringence. Note that for our argument we normalized both the probe and pump electric field strengths to 1, but in the experiment the THz field is much stronger (see the introduction of Chapter 3). Therefore, we expect the peak polarization modulation in the experiment to occur nearer to $45\,\mathrm{deg}$ than depicted in Fig. 4.9(b).

The same analysis was also applied to configuration (a) in Fig. 4.8, having a $\langle 100 \rangle$ cut crystal. The resulting polarization terms as a function of the probe angle are plotted in Fig. 4.10. The key difference is that the second-order nonlinear polarization terms are all zero for any probe angle. This property is clear upon inspection of the second-order nonlinear polarization vector (also found in Appendix A):

$$\begin{bmatrix} P^{(2)}_{\mathrm{pr}_x} \\ P^{(2)}_{\mathrm{pr}_y} \\ P^{(2)}_{\mathrm{pr}_z} \end{bmatrix} = 2\epsilon_0 \bar{\chi}^{(2)} \begin{bmatrix} -\sin(2\theta) & \cos(2\theta) & \cos(2\theta) & \sin(2\theta) \\ 0 & 0 & 0 & 0 \\ 0 & 0 & 0 & 0 \end{bmatrix} \begin{bmatrix} E_{\mathrm{pr}_y} E_{\mathrm{pu}_y} \\ E_{\mathrm{pr}_y} E_{\mathrm{pu}_z} \\ E_{\mathrm{pr}_z} E_{\mathrm{pu}_y} \\ E_{\mathrm{pr}_z} E_{\mathrm{pu}_z} \end{bmatrix}, \tag{4.23}$$

where all the transverse ($\hat{y}/\hat{z}$) contributions are zero. Moreover, one can see that this condition holds for any pump angle as well. The robustness of this property is why we have chosen a $\langle 100 \rangle$ crystal for isolating the third-order ($\chi^{(3)}$) nonlinear contribution.

With respect to the third-order polarization terms plotted in Fig. 4.10(b), it is fortuitous that their probe-angle dependence is the same for all crystal/field configurations used in the experiments [(a), (b), and (c) Fig. 4.8]. Comparing Fig. 4.10(b) and Fig. 4.9(b), it is apparent that only the magnitudes of the third order terms have changed. This property increases our confidence that the third-order nonlinear signal measured in both the $\langle 110 \rangle$ and $\langle 100 \rangle$ crystal will be the same, given the THz pump field is scaled appropriately.

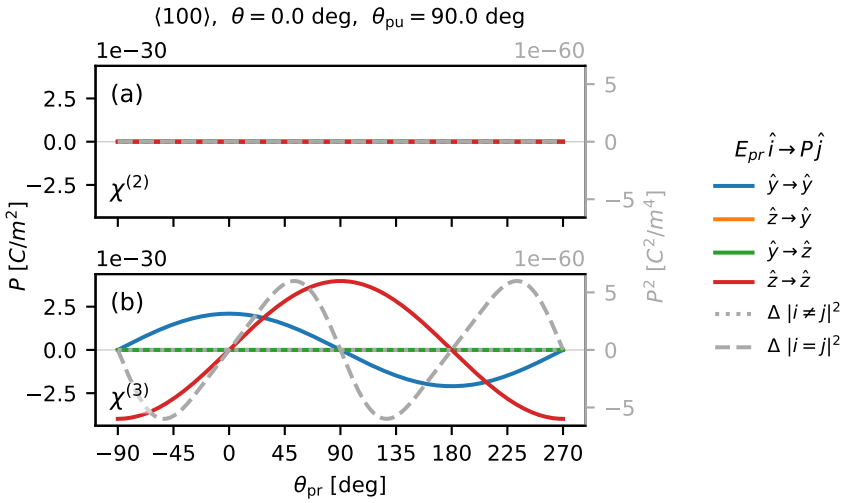

Figure 4.10. Second- and third-order nonlinear polarization terms in $\langle 100 \rangle$ cut ZnTe as a function of the probe polarization angle θ_{pr}. The crystal angle, θ, is $0\,\mathrm{deg}$, and the THz pump polarization angle, θ_{pu}, is $90\,\mathrm{deg}$. See Fig. 4.7 for angle definitions. The curves show the nonlinear polarization terms $P_{\mathrm{pr}_j} \propto E_{\mathrm{pr}_i}$. 'Orthogonal' terms with $j \neq i$, and 'parallel' terms with $j = i$ are grouped separately. $\Delta|i \neq j|$ is the magnitude-squared difference of the $\hat{z} \rightarrow \hat{y}$ and $\hat{y} \rightarrow \hat{z}$ terms. $\Delta|i = j|$ is the magnitude-squared difference of the $\hat{y} \rightarrow \hat{y}$ and $\hat{z} \rightarrow \hat{z}$ terms in a rotated frame fixed at a $45\,\mathrm{deg}$ angle to the probe (see text for details). (a) Second-order ($\chi^{(2)}$) nonlinear polarization terms. All terms are zero. (b) Third-order ($\chi^{(3)}$) nonlinear polarization terms. Both $i \neq j$ terms are zero.

4.3 2D THz-THz Polarimetry of ZnTe

With the foundations of the experiment laid, we can now present the culminating result in Fig.4.11. The experimental 2D THz-THz-polarimetry measurements on $1\,\mathrm{mm}$-thick $\langle 100\rangle$ and $\langle 110\rangle$ cut ZnTe are depicted at the top and bottom, respectively. Between these experimental measurements, simulations at several field strengths are included. All maps show only the *nonlinear* (NL) residual component, derived using a differential measurement as discussed in Section1.3.

As argued in the previous section, the measurement on $\langle 100\rangle$ cut ZnTe (top) should isolate third-order nonlinearities since the crystal and fields were oriented as illustrated in Fig. 4.8(a). In contrast, the measurement on $\langle 110\rangle$ cut ZnTe (bottom) would allow second-order nonlinearities to occur *only* via cascading through a primary third-order process, given that the crystal and fields were oriented as illustrated in Fig. 4.8(b). Comparing the two measurements, it is clear there is a difference between them, suggesting second-order nonlinearities are at play in the $\langle 110\rangle$ cut crystal.

To begin to attribute specific nonlinear processes to the features in these maps, rows (b) through (e) present a sequence of simulations where only nonlinear mixing products arising from THz-probe interactions were enabled. All nonlinear THz-THz interactions were disabled, although, linear dispersion and absorption of the THz pulses were still accounted for when generating the spatio-temporal maps of the THz fields in the crystal (refer to Sections 3.3 and 3.4 for implementation details).

In row (b), the simulation for $\langle 100\rangle$ cut ZnTe shows a marked similarity to the instantaneous sum- and difference-frequency generation (SFG and DFG) model presented in the introduction (Fig. 1.10). This is reasonable since, when *only* third-order processes are allowed, the direct process dominates:

$$\mathbf{P} = \epsilon_0 \chi^{(3)} \mathbf{E}_A \mathbf{E}_B \mathbf{E}_{\mathrm{pr}}. \tag{4.24}$$

The product $\mathbf{E}_A\mathbf{E}_B$ in this polarization term was the basis of the instantaneous SFG/DFG map. Surprisingly, a simple (instantaneous) multiplication of the measured fields can produce an accurate approximation of the full simulation, which integrates the evolution of the fields over the length of the crystal.

Moving from row (b) to row (c) in the main figure, we transitioned to a $\langle 110\rangle$ cut crystal, where second-order process are allowed *via cascading*, and reduced the simulated peak field strength to $10\,\mathrm{kV/cm}$. By sweeping the field strength from $10\,\mathrm{kV/cm}$ in row (c) to $40\,\mathrm{kV/cm}$ in row (e), we reveal that direct DFG/SFG features precede a multitude of secondary features that emerge around them. This order and the dependence on field strength suggest the presence of cascading, because typically, lower-order processes would dominate from the beginning, as evidenced by comparing the magnitudes of the second- and third-order polarization terms in Fig. 4.9. Therefore, it is likely that the direct third-order DFG/SFG processes indeed imbalance the second-order processes, allowing them to be detected with polarimetry as intended by the selection of the crystal and field orientations shown in Fig.4.8(b).

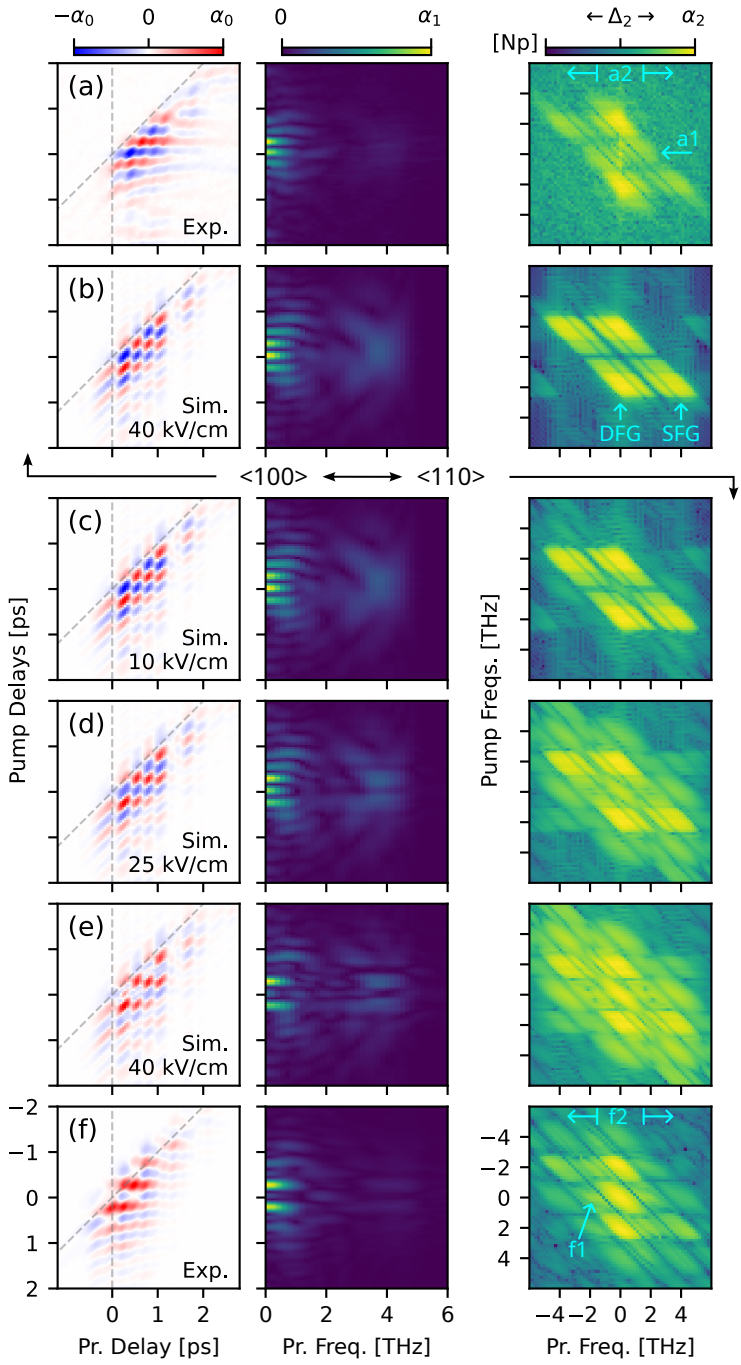

Figure 4.11. 2D THz-THz-polarimetry maps of the experimental (Exp.) and simulated (Sim.) nonlinear signal from 1 mm thick, ⟨100⟩ and ⟨110⟩ cut ZnTe. *(caption continues on next page. . .)*

Figure 4.11. *(. . . continued)* Rows (a) and (f) are the measured experimental data. Between them, in rows (b)-(e), are a series of simulations showing the evolution of the nonlinear signal as the crystal orientation and field strength are varied. For rows (a)-(b), the crystal is $\langle 100 \rangle$ cut, and oriented as specified in Fig.4.8(a). Moving to rows (c)-(f), we have changed to a $\langle 110 \rangle$ cut crystal, oriented as specified in Fig.4.8(b). The columns show different time-frequency representations: (left) time-time maps, linear-scale; (center) time-frequency maps, absolute-value linear-scale; (right) frequency-frequency maps, log-scale. The colormap scales are found in Tbl. 4.2. The nonlinear signals in rows (a) and (b), for the $\langle 100 \rangle$ crystal, serve as a reference of the primary third-order sum- and difference-frequency generation DFG/SFG contributions alone. In rows (c) through (e), for the $\langle 110 \rangle$ crystal, the emergence of secondary features with increasing field strength is indicative of cascading. Generally, there is good agreement between the experimental and simulated data, assuming a $40\,\mathrm{kV/cm}$ peak field strength in the models. Annotations a1 and f1 point out differences in the structure. Annotations a2 and f2 indicate a uniform attenuation of the measured data at higher probe-frequencies.

Table 4.2. Scales for the colormaps in Fig. 4.11

Row	Type	Cut	Pk. Field	α_0	α_1	α_2	Δ_2
(a)	Exp.	$\langle 100 \rangle$	$> 25\,\mathrm{kV/cm}$	2.50E−3	0.06	−0.22	12.46
(b)	Sim.	$\langle 100 \rangle$	$40\,\mathrm{kV/cm}$	4.11E−3	0.05	−0.65	13.22
(c)	Sim.	$\langle 110 \rangle$	$10\,\mathrm{kV/cm}$,	2.42E−4	2.83E−3	−3.46	12.97
(d)	Sim.	$\langle 110 \rangle$	$25\,\mathrm{kV/cm}$	1.39E−3	0.02	−1.82	14.57
(e)	Sim.	$\langle 110 \rangle$	$40\,\mathrm{kV/cm}$	3.00E−3	0.03	−1.27	13.96
(f)	Exp.	$\langle 110 \rangle$	$> 25\,\mathrm{kV/cm}$	0.08	1.52	2.95	10.54

However, we have yet to conclusively eliminate THz-THz nonlinearities as a significant contribution. The associated re-radiated polarization term is embedded in the cascaded process:

$$\mathbf{P} = \epsilon_0 \chi^{(2)} \underbrace{\left[\chi^{(2)} \mathbf{E}_A \mathbf{E}_B\right]}_{\text{Reradiated THz}} \mathbf{E}_{\mathrm{pr}}, \tag{4.25}$$

This process also contains the product $\mathbf{E}_A \mathbf{E}_B$. To determine its effect, we re-simulated the conditions from row (e) in the main figure, but with THz-THz nonlinearities *enabled*. The results are presented in Fig.4.12(a). For comparison, in Fig.4.12(b), we disabled THz-THz nonlinearities again. Inspecting the two simulations, it is difficult to visually identify any differences in their patterns or magnitudes. In Fig.4.12(c), we computed their difference, which appears to show that THz-THz components enhance the SFG content, albeit to a very small degree. However, it is worth noting that not accounting for dispersion of the second-order susceptibility could potentially underestimate the enhancement (Note4.5). Overall, the THz-THz contributions are on the order of 10^{-5} times smaller. Thus, it seems appropriate to consider them negligible.

By eliminating the influence of THz-THz interactions in our models, the vector diagrams introduced in Section 1.5 now offer greater clarity regarding the specific processes contributing to features in the frequency-frequency maps. We begin by analyzing the simulation for

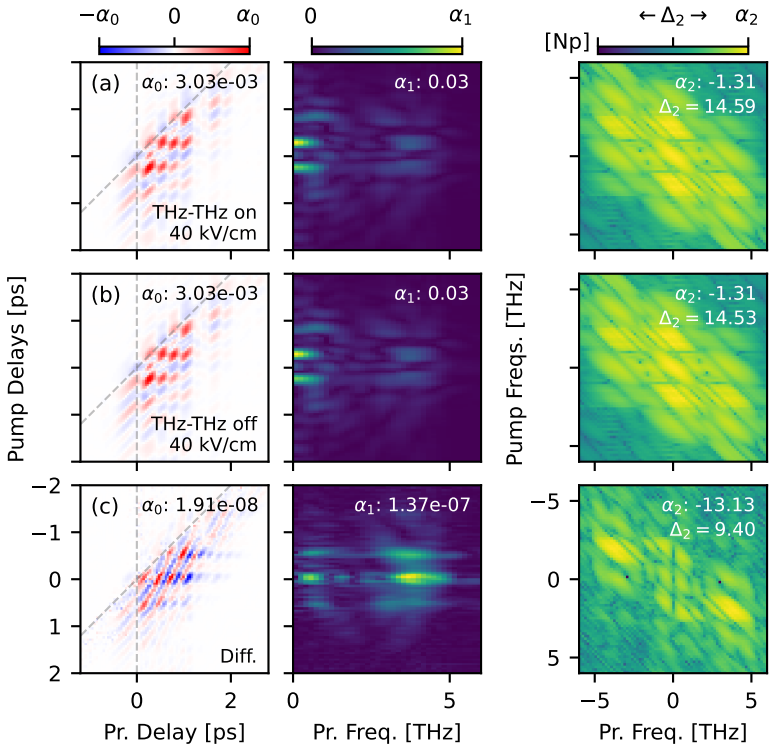

Figure 4.12. Comparison of the nonlinear (NL) signal for ⟨110⟩ cut ZnTe, oriented as in 4.8(b), with THz-THz nonlinear interactions on (a) and off (b). (b) This is the same nonlinear signal as in row-(e) of Fig. 4.11. (c) The difference of the nonlinear signals, (a) − (b). The nonlinear signals in (a) and (b) are visually indistinguishable, since the additional nonlinear content in (c) is approximately 10^{-5} of the amplitude. Notably, THz-THz nonlinearities seem to preferentially enhance the sum-frequency components, as seen in the frequency-frequency plot of difference (c).

⟨100⟩ cut ZnTe presented in row (b) of the main figure (Fig. 4.11), where only third-order nonlinearities are symmetry-allowed. We already identified the four main features in the frequency-frequency map (forming a left-leaning parallelogram) as direct third-order DFG and SFG products. For this crystal cut, the next-lowest-order processes are quasi fifth-order, arising from subsequent third-order processes that cascade from the primary direct third-order DFG and SFG products. The pathways for these processes are illustrated as vector chains in Fig. 4.13(a), and the locations of their products are indicated on the ⟨100⟩ frequency-frequency map in Fig. 4.13(b). Notably, the contribution from third-order cascading is weak, suggesting the secondary features that emerge with increasing field strength for the ⟨110⟩ cut in rows (c) through (e) result from second-order cascading.

To highlight the significance of this finding, it is important to understand that in the ⟨110⟩ cut crystal, second-order cascading can also produce quasi fifth-order products that are indistinguishable from those produced by third-order cascading. Second-order cascading is similar

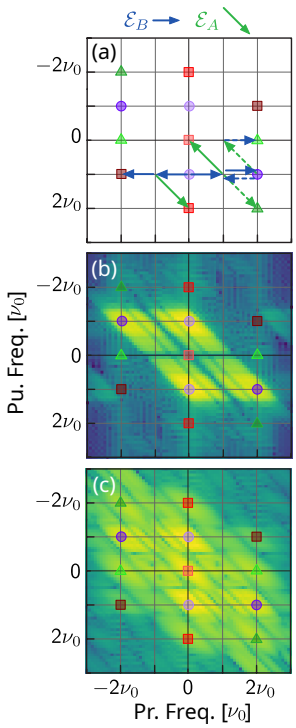

Direct Third-Order	Coords.	
$\mathcal{P}(\nu_A - \nu_B) \propto \left[\epsilon_0 \chi^{(3)} \mathcal{E}_A \mathcal{E}_B^* \mathcal{E}_{\mathrm{pr}}\right]$	$[0, \nu_0]$	DFG
$\mathcal{P}(\nu_A + \nu_B) \propto \left[\epsilon_0 \chi^{(3)} \mathcal{E}_A \mathcal{E}_B \mathcal{E}_{\mathrm{pr}}\right]$	$[2\nu_0, \nu_0]$	SFG

Third-Order Cascading	Coords.
$\mathcal{P}(0) \propto \epsilon_0 \chi^{(3)} \mathcal{E}_B \mathcal{E}_A^* [\mathrm{DFG}]$	$[0, 0]$
$\mathcal{P}(2\nu_A - 2\nu_B) \propto \epsilon_0 \chi^{(3)} \mathcal{E}_B^* \mathcal{E}_A [\mathrm{DFG}]$	$[0, 2\nu_0]$
$\mathcal{P}(\nu_A - 3\nu_B) \propto \epsilon_0 \chi^{(3)} \mathcal{E}_B^* \mathcal{E}_B^* [\mathrm{DFG}]$	$[-2\nu_0, \nu_0]$
$\mathcal{P}(2\nu_B) \propto \epsilon_0 \chi^{(3)} \mathcal{E}_A^* \mathcal{E}_B [\mathrm{SFG}]$	$[2\nu_0, 0]$
$\mathcal{P}(2\nu_A) \propto \epsilon_0 \chi^{(3)} \mathcal{E}_B^* \mathcal{E}_A [\mathrm{SFG}]$	$[2\nu_0, 2\nu_0]$

Second-Order Cascading	Coords.
$\mathcal{P}(0) \propto \epsilon_0 \chi^{(2)} \mathcal{E}_B \left(\epsilon_0 \chi^{(2)} \mathcal{E}_A^* [\mathrm{DFG}]\right)$	$[0, 0]$
$\mathcal{P}(2\nu_A - 2\nu_B) \propto \epsilon_0 \chi^{(2)} \mathcal{E}_B^* \left(\epsilon_0 \chi^{(2)} \mathcal{E}_A [\mathrm{DFG}]\right)$	$[0, 2\nu_0]$
$\mathcal{P}(\nu_A - 3\nu_B) \propto \epsilon_0 \chi^{(2)} \mathcal{E}_B^* \left(\epsilon_0 \chi^{(2)} \mathcal{E}_B^* [\mathrm{DFG}]\right)$	$[-2\nu_0, \nu_0]$
$\mathcal{P}(2\nu_B) \propto \epsilon_0 \chi^{(2)} \mathcal{E}_A^* \left(\epsilon_0 \chi^{(2)} \mathcal{E}_B [\mathrm{SFG}]\right)$	$[2\nu_0, 0]$
$\mathcal{P}(2\nu_A) \propto \epsilon_0 \chi^{(2)} \mathcal{E}_B^* \left(\epsilon_0 \chi^{(2)} \mathcal{E}_A [\mathrm{SFG}]\right)$	$[2\nu_0, 2\nu_0]$

Figure 4.13. Frequency vector representation of quasi-fifth-order products cascading from direct third-order products. (a) Vector-chain diagram. Direct third-order products (purple circles) at the difference- or sum-frequencies (DFG/SFG) are the same as in Fig. 1.9 (introduction, Section 1.5), but here the origin is shifted such that $[0, 0] = \omega_{\mathrm{pr}}$. The DFG or SFG terms can cascade with another third-order process to effectively create fifth-order products (red squares for DFG terms and green triangles for SFG terms). Similarly, two second-order processes can also cascade from the primary DFG or SFG terms (the *same* red squares and green triangles, respectively). Notably, third- and second-order cascaded products overlap in the frequency-frequency plots, highlighting the importance of comparing 2D THz-THz-polarimetry maps for the $\langle 100 \rangle$ cut (b), where only third-order products are allowed, and the $\langle 110 \rangle$ cut (c), where second-order processes are also allowed. Features beyond direct DFG and SFG (purple circles) appear to largely result from second-order cascading.

to its third-order counterpart, except that *two* second-order processes cascade from the direct third-order DFG and SFG products. The locations of these quasi fifth-order products are indicated on the $\langle 110 \rangle$ frequency-frequency map in Fig. 4.13(c), marking several of the secondary features. Significantly, the majority of the 'smooth' features can be accounted for by the quasi fifth-order products, including the prominent feature at $[0, 0]$THz, which can be attributed to quasi fifth-order optical rectification.

Before presenting our hypothesis, let us examine the quasi fourth-order terms presented in Fig.4.14. These terms arise from just *one* second order process cascading from the primary direct third-order DFG and SFG products. In the vector diagram shown in Fig.4.14(a), each primary DFG and SHG product gives rise to four possible cascaded pathways radiating away from it. Unlike for the fifth-order products, some of these pathways *overlap*. The cascaded products at the end of these pathways are indicated on the $\langle 110 \rangle$ frequency-frequency map in Fig. 4.14(b), where we are pleased to observe that the remaining secondary features have been marked. Notably, the products resulting from multiple excitation pathways align with the more structured features in the map, which we attribute to spectral interference. Each pathway may impart a different phase, leading to spectral holes where there is destructive interference, and peaks where constructive interference occurs.

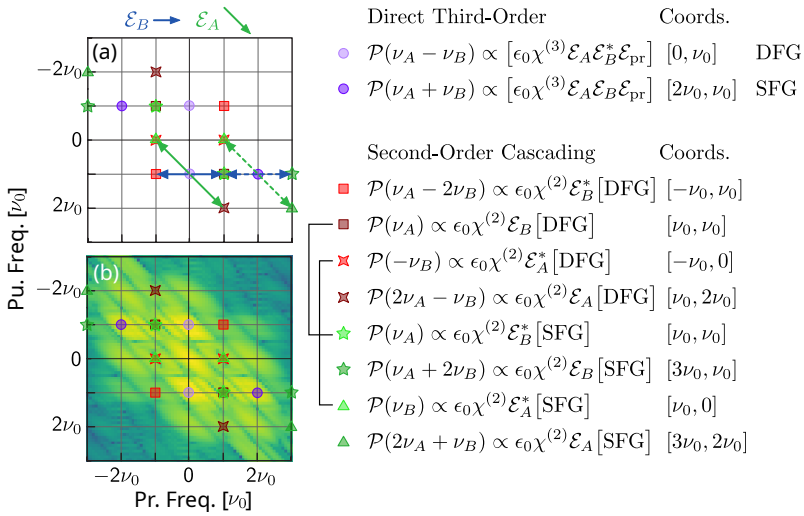

Figure 4.14. Frequency vector representation of quasi-fourth-order products cascading from direct third-order products. (a) Vector-chain diagram. Direct third-order products (purple circles) at the difference- or sum-frequencies (DFG/SFG) are the same as in Fig. 1.9 (introduction, Section 1.5), but here the origin is shifted such that $[0, 0] = \omega_{\rm pr}$. The DFG or SFG terms can cascade with another second-order process to effectively create fourth-order products (red squares and four-point stars for DFG terms, and green triangles and five-point stars for SFG terms). Notably, some products overlap in the frequency-frequency plots, and these happen to be the more structured features in the map for the $\langle 110 \rangle$ cut crystal (b). We hypothesize that the structure results from spectral interference between the two cascaded excitation pathways when they are in/out of phase.

To drive-home the influence of cascading in the $\langle 110 \rangle$ crystal, we performed a simple numerical experiment. Unlike in the real world, we can freely enable or disable $\chi^{(2)}$ and $\chi^{(3)}$. This allows us to examine the contributions of second- ($\chi^{(2)}$) and third-order ($\chi^{(3)}$) processes separately. Although we have already presented evidence supporting cascading, let us momentarily adopt a naive perspective. In Fig. 4.15(a) the nonlinear signal with both $\chi^{(2)}$ and $\chi^{(3)}$ enabled is presented, which is simply a reproduction of row (e) in the main figure. It is a complicated nonlinear map, which one would expect given the wide variety of possible second- and third-order processes. Consequently, a logical first step is reducing the complexity by disabling $\chi^{(3)}$ and observing the sole contribution of the second-order processes. This scenario is presented in Fig. 4.15(b), resulting in only numerical noise. It appears second-order processes are entirely negligible, which is perhaps not surprising given we oriented the

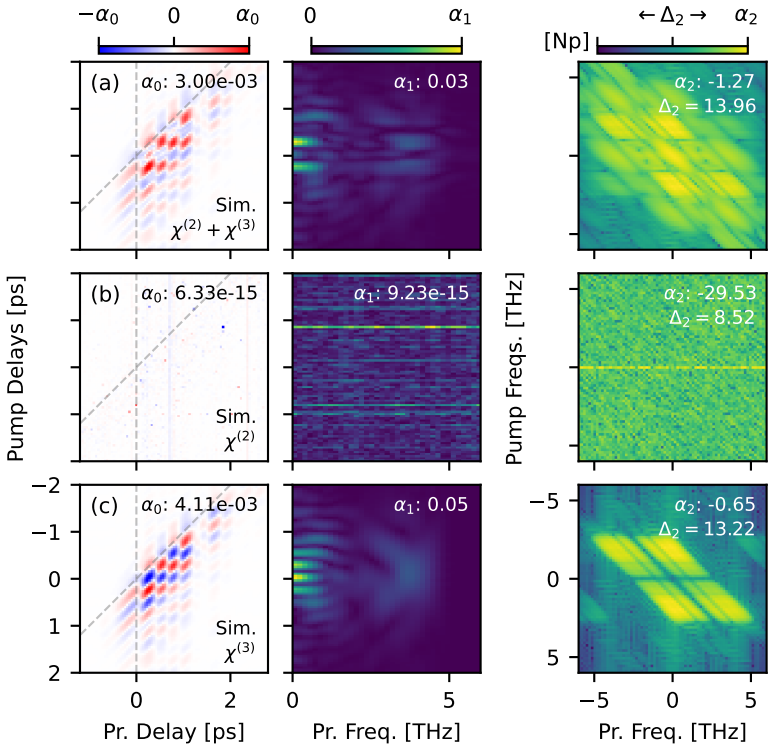

Figure 4.15. A simple numerical experiment to demonstrate the influence of cascading in the $\langle 110 \rangle$ crystal. We selectively enable or disable $\chi^{(2)}$ and $\chi^{(3)}$ to determine their influence separately. (a) Nonlinear signal with both $\chi^{(2)}$ and $\chi^{(3)}$ enabled, showing the full array of nonlinear products. (b) Sole contribution of $\chi^{(2)}$ with $\chi^{(3)}$ disabled, resulting in numerical noise only. (c) Sole contribution of $\chi^{(3)}$ with $\chi^{(2)}$ disabled, showing an incomplete array of nonlinear products. These findings indicate the presence of emergent phenomena, where the full nonlinear signal exceeds the sum of its parts. The interaction or 'cascade' between the second- and third-order processes is evident in the 2D maps, confirming the sensitivity of 2D THz-THz-polarimetry in revealing cascaded phenomena.

crystal and fields as shown in Fig. 4.8(b), with the aim of nullifying the second-order contribution to the polarimetric signal. Given this outcome, it might be reasonable to expect third-order processes are the sole contributors. However, as demonstrated in Fig. 4.8(c), where only $\chi^{(3)}$ is enabled, we do not recover the full array of nonlinear features. This surprising result reveals the presence of emergent phenomena: the whole nonlinear signal is greater than the sum of its parts. There are processes that evolve in the crystal only when *both* $\chi^{(2)}$ and $\chi^{(3)}$ are non-zero. In other words, the second- and third-order processes interact or 'cascade' with each other. The products of these interactions are plainly evident in the 2D maps, proving 2D THz-THz-polarimetry is a sensitive technique for revealing cascaded phenomena.

4.3.1 Improvements and Future work

With a better understanding of the simulations established, we can now comment on a few features in the measured data that deviate from our models. In the $\langle 100 \rangle$ frequency-frequency plot displayed in row (a) of the main figure (Fig. 4.11), there are additional features along the horizontal mid-line (pump-frequency = 0 THz) in comparison to the simulation in row (b). The sharp point at the origin, $[0, 0]$ THz, is perhaps simply an overall 'DC'-offset of the data that was not entirely removed. However, the feature labeled 'a1' cannot be dismissed as easily. It is located at approximately $[2, 0]$ THz, which overlaps the fundamental frequency of the B pump pulse, as shown in Fig. 1.7. Given the breadth of the feature, we know it is not simply leakage of the B-pulse fundamental, but likely contains products of the A-pulse that cancel, such as $\mathcal{E}_A \mathcal{E}_A^*$ (refer back to Section 1.7). One possible explanation is that the fields are not perfectly normally-incident on the $\langle 100 \rangle$ cut-plane and there is a small second-order contribution from the terms

$$\mathcal{P}(-\nu_B) \propto \epsilon_0 \chi^{(2)} \mathcal{E}_A^* \big[\mathrm{DFG}\big] \; [-\nu_0, 0], \tag{4.26}$$

$$\mathcal{P}(\nu_B) \propto \epsilon_0 \chi^{(2)} \mathcal{E}_A^* \big[\mathrm{SFG}\big] \quad [\nu_0, 0]. \tag{4.27}$$

The products from these terms are indicated in Fig. 4.14. Alternatively, this feature could be a third-order THz-THz 'pump-probe' signal, where the A-pulse pumps the sample and the B-pulse is influenced by the resulting material change [35]. This nonlinearity has the form

$$\mathcal{P}(\nu_B) \propto \epsilon_0 \chi^{(3)} \mathcal{E}_A \mathcal{E}_A^* \mathcal{E}_B [\nu_0, 0], \tag{4.28}$$

and is not necessarily included in our model. For example, if the A-pulse generates free carriers through impact-ionization, then that would increase the attenuation of the B-pulse and would not be included in our model [28]. If the THz-THz pump-probe process is strongly dependent on field strength, it would perhaps also explain why we do not see a 'B-pump A-probe' signal since, as shown in Fig. 4.16, the A-pulse is higher amplitude than the B-pulse.

On the matter of field strengths, Fig. 4.16(b) raises a glaring oversight: for the measurements in the main figure (Fig. 4.11), there were two wire grid polarizers (PureWave PW005-012-075) placed in the collimated section of beam path between the two 4 in off-axis parabolic mirrors shown in Fig. 2.1. Unfortunately, we did not record reference waveforms with the polarizers in place and in a nitrogen-purged environment. However, the polarizers were oriented

with the wires perpendicular to the polarization direction of the THz pump fields in order to be maximally transparent. The theoretical transmission factor for each polarizer is > 0.97 (see *specifications*), although based on the measurements, it seems likely that the real-world transmission factor is lower. Regardless, it is difficult to make a conclusive statement, since we observe strong ringing after the main pulse in Fig. 4.16(b) that is indicative of water-vapor absorption (refer back to Section 2.6.2). Therefore, we considered the peak field strengths used in our simulations to be fitting parameters that we adjusted to obtain the optimal qualitative pattern. It is possible that small deviations in the fine-structure of the measurements, for example the feature annotated 'f1' in row (f) of the main figure, are due to a slight alteration of the THz pump pulses with respect to the reference waveforms.

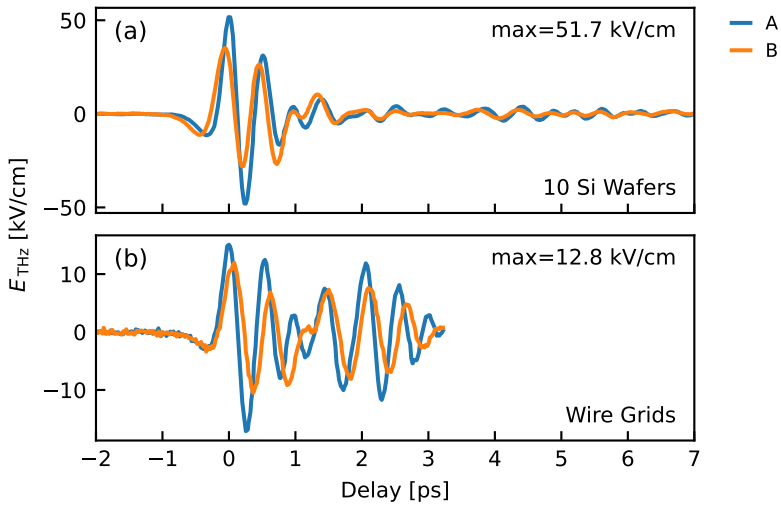

Figure 4.16. Comparison of the A and B THz pump pulse electric fields. These are the recovered field strengths before attenuation. (a) Attenuation with 10 Si wafers, relatively well purged environment. (b) Attenuation with wire grid polarizers, unpurged environment.

With respect to the amplitudes of the nonlinear signals in the main figure (Fig.4.11), it is difficult to ignore the fact that the magnitude of the nonlinear signal for the experimental $\langle 110 \rangle$ data in row (f) is an outlier. In this work, we have primarily focused on the qualitative pattern of features rather than their absolute magnitude. As mentioned, we considered the peak field strengths used in our simulations as fitting parameters. With that said, we were pleased to see a generally good agreement between the magnitudes of the experimental and simulated data for the $\langle 100 \rangle$ cut crystal, in rows (a) and (b) respectively (refer to Tbl.4.2 for values). The simulations, too, generally behave as one would expect for the $\langle 110 \rangle$ cut crystal in rows (c) through (f): the magnitude of the nonlinear signal increases with field strength, ultimately reaching a value $\alpha_0 = 3.00\text{E}{-3}$ at $40\,\text{kV/cm}$, which is very close to $\alpha_0 = 4.11\text{E}{-3}$ for the $\langle 100 \rangle$ simulation at the same field strength. The magnitudes for the $\langle 100 \rangle$ and $\langle 110 \rangle$ cuts should be similar since the second-order processes cascade from primary third-order processes, and therefore, the latter largely sets the upper bound. At the moment,

we do not know if the deviation of the experimental $\langle 110 \rangle$ measurements is simply an error of scaling or if it is truly physical. It is an area of active investigation.

The final aspect of improvement under discussion is the disparity in magnitude between the direct third-order DFG and SFG products. In general, all features at higher probe frequencies in the measured frequency-frequency maps are weaker, as indicated by annotations 'a2' and 'f2'. We do not see the same behavior in the simulations, even though linear absorption is taken into account (refer back to Section 3.3). It would have been reasonable to attribute additional attenuation to the broad absorption peak at 3.7 THz in Fig. 3.2, but the reality is more complex. Indeed, completely neglecting the absorption peak makes little difference in the simulation. This is because the frequency-frequency maps display the THz modulation at *optical* frequencies. It is important to remember that we indirectly measure the THz field as a modulation of the optical probe's polarization. The origins of the frequency-frequency maps, which are currently $[0, 0]$ THz, should realistically be shifted to $[2\pi\omega_0, 2\pi\omega_0]$ THz, where ω_0 is the carrier angular frequency of the probe. The significance of this is that once the THz fields modulate the probe polarization, the resulting product is shifted up by the optical carrier frequency of the probe, and the absorption coefficient at THz frequencies is irrelevant.

However, the same phonons responsible for the broad absorption peak at 3.7 THz may potentially alter the nonlinear susceptibility. Typically, Miller's rule, which estimates the nonlinear susceptibility as a product of the linear susceptibilities at all the involved frequencies, provides a reasonable approximation. For the third-order susceptibility considered here, it takes the form:

$$\chi^{(3)}(\omega_f, \pm\Omega, \pm\Omega, \omega_0) = \delta\chi^{(1)}(\omega_f)\chi^{(1)}(\Omega)\chi^{(1)}(\Omega)\chi^{(1)}(\omega_0), \tag{4.29}$$

where $\omega_f \in \omega_0 \pm \{2\Omega, 0\}$ is the final product angular frequency and δ is assumed to be frequency-independent and nearly the same for all materials [7, Sec. 5.2]. The issue with Miller's rule in our case is that a few-THz change is essentially negligible at optical frequencies, where the susceptibility is relatively flat. Consequently, $\chi^{(1)}(\omega_f) \approx \chi^{(1)}(\omega_0)$ and $\chi^{(3)}(\omega_0 \pm 2\Omega) \approx \chi^{(3)}(\omega_0 \pm 0)$, implying that both SFG and DFG should be equally favorable. However, our measurements indicate that $\chi^{(3)}(\omega_0 \pm 2\Omega)$ must be less than $\chi^{(3)}(\omega_0 \pm 0)$.

Based on the literature, it is possible that a more complex second-order phonon process is altering the effective third-order nonlinear susceptibility, as the broad absorption band at 3.7 THz arises from the difference modes between optical and acoustic phonons in ZnTe [11, 48]. It is conceivable that the phonons associated with the 3.7 THz absorption band also provide a non-radiative decay channel for the considered SFG process. Schall et al. [48] demonstrated that cooling ZnTe below 50 K nearly eliminates these second-order phonon absorption bands, offering a straightforward experiment to potentially determine their role in attenuating the SFG product.

Conclusion

The foregoing chapters have reported recent developments in two-dimensional (2D) terahertz (THz) spectroscopy at DTU, including instrumentation, a numerical pulse propagation methodology for simulation, and their combined application for distinguishing cascaded and direct nonlinear optical (NLO) process.

Specifically, we have performed a series of experiments to demonstrate the capacity of 2D THz-THz-polarimetry for distinguishing direct and cascaded nonlinear optical properties in ZnTe. Firstly, a $\langle 100 \rangle$ cut ZnTe crystal was used to effectively disable second-order $(\chi^{(2)})$ processes for all field polarizations, regardless of cascading. This served as a reference for the signature of third-order $(\chi^{(3)})$ processes alone. Secondly, a $\langle 110 \rangle$ cut ZnTe crystal was oriented in a way that second-order processes could only occur by cascading through a primary third-order process.

The results of these measurements were presented alongside corresponding numerical pulse propagation simulations. A comparative analysis of the measured and simulated nonlinear polarimetric maps revealed a high degree of self-consistency. This result provided the confidence to further utilize the simulations to selectively enable or disable the underlying second- and third-order processes numerically, aiming to isolate their independent and coupled contributions. By doing so, we determined that 'THz-THz' processes between the two THz pump pulses themselves made negligible contributions to the nonlinear signal. Instead, the predominant contributions came from both direct and cascaded nonlinear 'THz-probe' processes between the THz pump pulses and the optical probe pulse.

With the identification of 'THz-probe' nonlinearities as the main contributors, we then were able to assign specific direct and cascaded nonlinear optical processes to features in the 2D frequency-frequency maps using the frequency vector representation developed by Kuehn et al. [34, 35].

The numerical tools and methodologies developed are immediately applicable to all other zincblende crystals and can be extended to include other crystal space groups and higher-order nonlinear optical processes. Moreover, we have highlighted the possible contribution of coupled second-order *phonon* processes to the nonlinear polarimetric maps, suggesting a potential direction for future research.

Overall, the instrumentation and interpretations reported herein are applicable to a broad range of physical phenomena. It is our hope that this thesis proves to be a valuable resource for future endeavors in this field.

Appendices

APPENDIX A

Nonlinear Polarizations

A.1 $\langle 110 \rangle$ ZnTe THz-THz Nonlinear Polarizations

$$\begin{bmatrix} P^{(2)}_{\mathrm{pu}_x} \\ P^{(2)}_{\mathrm{pu}_y} \\ P^{(2)}_{\mathrm{pu}_z} \end{bmatrix} = \epsilon_0 \bar{\chi}^{(2)} \begin{bmatrix} 0 & 0 & 0 \\ 3\sin\theta\cos^2\theta & 6\sin^2\theta\cos\theta - 2\cos\theta & 3\sin^3\theta - 2\sin\theta \\ 2\cos\theta - 3\cos^3\theta & 6\sin^3\theta - 4\sin\theta & -3\sin^2\theta\cos\theta \end{bmatrix} \begin{bmatrix} E^2_{\mathrm{pu}_y} \\ E_{\mathrm{pu}_y} E_{\mathrm{pu}_z} \\ E^2_{\mathrm{pu}_z} \end{bmatrix} \tag{A.1}$$

$$\begin{bmatrix} P^{(3)}_{\mathrm{pu}_x} \\ P^{(3)}_{\mathrm{pu}_y} \\ P^{(3)}_{\mathrm{pu}_z} \end{bmatrix} = \frac{\epsilon_0}{2} \begin{bmatrix} 0 & \cdots \\ \left(3\sin^4\theta - 2\sin^2\theta + 1\right)a + \left(6\sin^2\theta - 9\sin^4\theta + 3\right)b & \cdots \\ \left(\sin\theta\cos^3\theta - 2\sin^3\theta\cos\theta\right)a + \left(6\sin^3\theta\cos\theta - 3\sin\theta\cos^3\theta\right)b & \cdots \end{bmatrix} \tag{A.2}$$

$$\begin{matrix} \cdots \\ \cdots \\ \cdots \\ \cdots \\ \cdots \\ \cdots \\ \cdots \\ \cdots \\ \cdots \end{matrix} \begin{bmatrix} 0 & \cdots \\ \left(3\sin\theta\cos^3\theta - 6\sin^3\theta\cos\theta\right)a + \left(18\sin^3\theta\cos\theta - 9\sin\theta\cos^3\theta\right)b & \cdots \\ \left(9\sin^2\theta - 9\sin^4\theta\right)a + \left(27\sin^4\theta - 27\sin^2\theta + 6\right)b & \cdots \\ 0 & \cdots \\ \left(9\sin^2\theta - 9\sin^4\theta\right)a + \left(27\sin^4\theta - 27\sin^2\theta + 6\right)b & \cdots \\ \left(3\sin^3\theta\cos\theta - 6\sin\theta\cos^3\theta\right)a + \left(18\sin\theta\cos^3\theta - 9\sin^3\theta\cos\theta\right)b & \cdots \\ 0 & \cdots \\ \left(\sin^3\theta\cos\theta - 2\sin\theta\cos^3\theta\right)a + \left(6\sin\theta\cos^3\theta - 3\sin^3\theta\cos\theta\right)b & \cdots \\ \left(3\sin^4\theta - 4\sin^2\theta + 2\right)a + \left(12\sin^2\theta - 9\sin^4\theta\right)b & \cdots \end{bmatrix} \begin{bmatrix} E^3_{\mathrm{pu}_y} \\ E^2_{\mathrm{pu}_y} E_{\mathrm{pu}_z} \\ E_{\mathrm{pu}_y} E^2_{\mathrm{pu}_z} \\ E^3_{\mathrm{pu}_z} \end{bmatrix}$$

A.2 $\langle 110 \rangle$ ZnTe THz-Probe Nonlinear Polarizations

$$\begin{bmatrix} P^{(2)}_{\mathrm{pr}_x} \\ P^{(2)}_{\mathrm{pr}_y} \\ P^{(2)}_{\mathrm{pr}_z} \end{bmatrix} = 2\epsilon_0 \bar{\chi}^{(2)} \begin{bmatrix} 0 & 0 & 0 & 0 \\ -3\sin^3\theta + 3\sin\theta & 2\cos\theta - 3\cos^3\theta & 2\cos\theta - 3\cos^3\theta & 3\sin^3\theta - 2\sin\theta \\ 2\cos\theta - 3\cos^3\theta & 3\sin^3\theta - 2\sin\theta & 3\sin^3\theta - 2\sin\theta & 3\cos^3\theta - 3\cos\theta \end{bmatrix} \begin{bmatrix} E_{\mathrm{pr}_y} E_{\mathrm{pu}_y} \\ E_{\mathrm{pr}_y} E_{\mathrm{pu}_z} \\ E_{\mathrm{pr}_z} E_{\mathrm{pu}_y} \\ E_{\mathrm{pr}_z} E_{\mathrm{pu}_z} \end{bmatrix} \tag{A.3}$$

$$
\begin{bmatrix} P^{(3)}_{\mathrm{pr}_x} \\ P^{(3)}_{\mathrm{pr}_y} \\ P^{(3)}_{\mathrm{pr}_z} \end{bmatrix} = \frac{3\epsilon_0}{2} \begin{bmatrix}
\cdots & & \cdots & \\
0 & & & \\
\left(3\sin^4\theta - 2\sin^2\theta + 1\right)a + \left(-9\sin^4\theta + 6\sin^2\theta + 3\right)b & \cdots & & \\
\left(-2\sin^3\theta\cos\theta + \sin\theta\cos^3\theta\right)a + \left(6\sin^3\theta\cos\theta - 3\sin\theta\cos^3\theta\right)b & \cdots & & \\
\cdots & & \cdots & \\
0 & & & \\
\left(-4\sin^3\theta\cos\theta + 2\sin\theta\cos^3\theta\right)a + \left(12\sin^3\theta\cos\theta - 6\sin\theta\cos^3\theta\right)b & \cdots & & \\
\left(-6\sin^4\theta + 6\sin^2\theta\right)a + \left(18\sin^4\theta - 18\sin^2\theta + 4\right)b & \cdots & & \\
\cdots & & \cdots & \\
0 & & & \\
\left(-3\sin^4\theta + 3\sin^2\theta\right)a + \left(9\sin^4\theta - 9\sin^2\theta + 2\right)b & \cdots & & \\
\left(\sin^3\theta\cos\theta - 2\sin\theta\cos^3\theta\right)a + \left(-3\sin^3\theta\cos\theta + 6\sin\theta\cos^3\theta\right)b & \cdots & & \\
\cdots & & \cdots & \\
0 & & & \\
\left(-2\sin^3\theta\cos\theta + \sin\theta\cos^3\theta\right)a + \left(6\sin^3\theta\cos\theta - 3\sin\theta\cos^3\theta\right)b & \cdots & & \\
\left(-3\sin^4\theta + 3\sin^2\theta\right)a + \left(9\sin^4\theta - 9\sin^2\theta + 2\right)b & \cdots & & \\
\cdots & & \cdots & \\
0 & & & \\
\left(-6\sin^4\theta + 6\sin^2\theta\right)a + \left(18\sin^4\theta - 18\sin^2\theta + 4\right)b & \cdots & & \\
\left(2\sin^3\theta\cos\theta - 4\sin\theta\cos^3\theta\right)a + \left(-6\sin^3\theta\cos\theta + 12\sin\theta\cos^3\theta\right)b & \cdots & & \\
\cdots & & \cdots & \\
0 & & & \\
\left(\sin^3\theta\cos\theta - 2\sin\theta\cos^3\theta\right)a + \left(-3\sin^3\theta\cos\theta + 6\sin\theta\cos^3\theta\right)b & & & \\
\left(3\sin^4\theta - 4\sin^2\theta + 2\right)a + \left(-9\sin^4\theta + 12\sin^2\theta\right)b & & &
\end{bmatrix}
\begin{bmatrix}
E_{\mathrm{pr}_y}E^2_{\mathrm{pu}_y} \\
E_{\mathrm{pr}_y}E_{\mathrm{pu}_y}E_{\mathrm{pu}_z} \\
E_{\mathrm{pr}_y}E^2_{\mathrm{pu}_z} \\
E_{\mathrm{pr}_z}E^2_{\mathrm{pu}_y} \\
E_{\mathrm{pr}_z}E_{\mathrm{pu}_y}E_{\mathrm{pu}_z} \\
E_{\mathrm{pr}_z}E^2_{\mathrm{pu}_z}
\end{bmatrix}
\tag{A.4}
$$

A.3 $\langle 100 \rangle$ ZnTe THz-THz Nonlinear Polarizations

$$\begin{bmatrix} P^{(2)}_{\mathrm{pu}_x} \\ P^{(2)}_{\mathrm{pu}_y} \\ P^{(2)}_{\mathrm{pu}_z} \end{bmatrix} = \epsilon_0 \bar{\chi}^{(2)} \begin{bmatrix} -\sin(2\theta) & 2\cos(2\theta) & \sin(2\theta) \\ 0 & 0 & 0 \\ 0 & 0 & 0 \end{bmatrix} \begin{bmatrix} E^2_{\mathrm{pu}_y} \\ E_{\mathrm{pu}_y} E_{\mathrm{pu}_z} \\ E^2_{\mathrm{pu}_z} \end{bmatrix} \tag{A.5}$$

$$\begin{bmatrix} P^{(3)}_{\mathrm{pu}_x} \\ P^{(3)}_{\mathrm{pu}_y} \\ P^{(3)}_{\mathrm{pu}_z} \end{bmatrix} = \frac{\epsilon_0}{4} \begin{bmatrix} 0 & \cdot & \cdots \\ \left(2\sin^4\theta - 2\sin^2\theta + 1\right) a + \left(-6\sin^4\theta + 6\sin^2\theta\right) b & \cdots & \cdots \\ \left(-2\sin^3\theta\cos\theta + \sin\theta\cos\theta\right) a + \left(6\sin^3\theta\cos\theta - 3\sin\theta\cos\theta\right) b & \cdots & \cdots \end{bmatrix} \tag{A.6}$$

$$\begin{bmatrix} \cdots & 0 & \cdots \\ \cdots & \left(-6\sin^3\theta\cos\theta + 3\sin\theta\cos\theta\right) a + \left(18\sin^3\theta\cos\theta - 9\sin\theta\cos\theta\right) b & \cdots \\ \cdots & \left(-6\sin^4\theta + 6\sin^2\theta\right) a + \left(18\sin^4\theta - 18\sin^2\theta + 3\right) b & \cdots \\ \cdots & 0 & \cdots \\ \cdots & \left(-6\sin^4\theta + 6\sin^2\theta\right) a + \left(18\sin^4\theta - 18\sin^2\theta + 3\right) b & \cdots \\ \cdots & \left(6\sin^3\theta\cos\theta - 3\sin\theta\cos\theta\right) a + \left(-18\sin^3\theta\cos\theta + 9\sin\theta\cos\theta\right) b & \cdots \\ \cdots & 0 & \\ \cdots & \left(2\sin^3\theta\cos\theta - \sin\theta\cos\theta\right) a + \left(-6\sin^3\theta\cos\theta + 3\sin\theta\cos\theta\right) b & \\ \cdots & \left(2\sin^4\theta - 2\sin^2\theta + 1\right) a + \left(-6\sin^4\theta + 6\sin^2\theta\right) b & \end{bmatrix} \begin{bmatrix} E^3_{\mathrm{pu}_y} \\ E^2_{\mathrm{pu}_y} E_{\mathrm{pu}_z} \\ E_{\mathrm{pu}_y} E^2_{\mathrm{pu}_z} \\ E^3_{\mathrm{pu}_z} \end{bmatrix}$$

A.4 $\langle 100 \rangle$ ZnTe THz-Probe Nonlinear Polarizations

$$\begin{bmatrix} P^{(2)}_{\mathrm{pr}_x} \\ P^{(2)}_{\mathrm{pr}_y} \\ P^{(2)}_{\mathrm{pr}_z} \end{bmatrix} = 2\epsilon_0 \bar{\chi}^{(2)} \begin{bmatrix} -\sin(2\theta) & \cos(2\theta) & \cos(2\theta) & \sin(2\theta) \\ 0 & 0 & 0 & 0 \\ 0 & 0 & 0 & 0 \end{bmatrix} \begin{bmatrix} E_{\mathrm{pr}_y} E_{\mathrm{pu}_y} \\ E_{\mathrm{pr}_y} E_{\mathrm{pu}_z} \\ E_{\mathrm{pr}_z} E_{\mathrm{pu}_y} \\ E_{\mathrm{pr}_z} E_{\mathrm{pu}_z} \end{bmatrix} \tag{A.7}$$

$$
\begin{bmatrix} P^{(3)}_{\mathrm{pr}_x} \\ P^{(3)}_{\mathrm{pr}_y} \\ P^{(3)}_{\mathrm{pr}_z} \end{bmatrix} = 3\epsilon_0 \begin{bmatrix}
0 & \cdots & & & & \cdots \\
\left(2\sin^4\theta - 2\sin^2\theta + 1\right)a + \left(-6\sin^4\theta + 6\sin^2\theta\right)b & \cdots & & & & \cdots \\
\left(-2\sin^3\theta\cos\theta + \sin\theta\cos\theta\right)a + \left(6\sin^3\theta\cos\theta - 3\sin\theta\cos\theta\right)b & \cdots & & & & \cdots \\
\cdots & 0 & \cdots & & & \cdots \\
\cdots & \left(-4\sin^3\theta\cos\theta + 2\sin\theta\cos\theta\right)a + \left(12\sin^3\theta\cos\theta - 6\sin\theta\cos\theta\right)b & \cdots & & & \cdots \\
\cdots & \left(-4\sin^4\theta + 4\sin^2\theta\right)a + \left(12\sin^4\theta - 12\sin^2\theta + 2\right)b & \cdots & & & \cdots \\
\cdots & 0 & \cdots & & & \\
\cdots & \left(-2\sin^4\theta + 2\sin^2\theta\right)a + \left(6\sin^4\theta - 6\sin^2\theta + 1\right)b & \cdots & & & \\
\cdots & \left(2\sin^3\theta\cos\theta - \sin\theta\cos\theta\right)a + \left(-6\sin^3\theta\cos\theta + 3\sin\theta\cos\theta\right)b & \cdots & & & \\
\cdots & 0 & \cdots & & & \\
\cdots & \left(-2\sin^3\theta\cos\theta + \sin\theta\cos\theta\right)a + \left(6\sin^3\theta\cos\theta - 3\sin\theta\cos\theta\right)b & \cdots & & & \\
\cdots & \left(-2\sin^4\theta + 2\sin^2\theta\right)a + \left(6\sin^4\theta - 6\sin^2\theta + 1\right)b & \cdots & & & \\
\cdots & 0 & \cdots & & & \cdots \\
\cdots & \left(-4\sin^4\theta + 4\sin^2\theta\right)a + \left(12\sin^4\theta - 12\sin^2\theta + 2\right)b & \cdots & & & \cdots \\
\cdots & \left(4\sin^3\theta\cos\theta - 2\sin\theta\cos\theta\right)a + \left(-12\sin^3\theta\cos\theta + 6\sin\theta\cos\theta\right)b & \cdots & & & \cdots \\
\cdots & 0 & \cdots & & & \\
\cdots & \left(2\sin^3\theta\cos\theta - \sin\theta\cos\theta\right)a + \left(-6\sin^3\theta\cos\theta + 3\sin\theta\cos\theta\right)b & \cdots & & & \\
\cdots & \left(2\sin^4\theta - 2\sin^2\theta + 1\right)a + \left(-6\sin^4\theta + 6\sin^2\theta\right)b & \cdots & & &
\end{bmatrix}
\begin{bmatrix} E_{\mathrm{pr}_y}E^2_{\mathrm{pu}_y} \\ E_{\mathrm{pr}_y}E_{\mathrm{pu}_y}E_{\mathrm{pu}_z} \\ E_{\mathrm{pr}_y}E^2_{\mathrm{pu}_z} \\ E_{\mathrm{pr}_z}E^2_{\mathrm{pu}_y} \\ E_{\mathrm{pr}_z}E_{\mathrm{pu}_y}E_{\mathrm{pu}_z} \\ E_{\mathrm{pr}_z}E^2_{\mathrm{pu}_z} \end{bmatrix} \tag{A.8}
$$

Publications and Contributions

Publications

- Martin J. Cross, Malte L. Welsch, Edmund J. R. Kelleher, Peter U. Jepsen, "*Discriminating THz-Frequency Nonlinear Optical Processes in ZnTe with Two-Dimensional Spectroscopy*" (**in preperation**)
- Malte L.Welsch, Martin J. Cross, Tobias O.Buchmann, Simon J. Lange, Edmund J. R. Kelleher, Peter U. Jepsen, "*Autocorrelation with novel field-driven photomultiplier for mid-infrared light*" (**in preperation**)
- Malte L.Welsch, Martin J. Cross, Lars R. Lindvold, Simon J. Lange, Edmund J. R. Kelleher, Peter U. Jepsen, "*Electron field emission into liquids and gases: exploring tunnel ionization effects and their influence*" (**in preperation**)

Conference Contributions

- Martin J. Cross, Malte L.Welsch, Edmund J. R. Kelleher, Peter U. Jepsen, "*Discriminating THz-Frequency Nonlinear Optical Processes in ZnTe with Two-Dimensional Spectroscopy*", Optical Terahertz Science and Technology (OTST), 2022, Budapest (**talk**)
- Malte L.Welsch, Martin J. Cross, Lars R. Lindvold, Simon J. Lange, Edmund J. R. Kelleher, Peter U. Jepsen, "*Light Emission from Gases and Liquids Excited by THz-Driven Field-Emitted Electrons*", Optical Terahertz Science and Technology (OTST), 2022, Budapest (**talk**)

Bibliography

[1] G. P. Agrawal. *Nonlinear Fiber Optics*. Elsevier/Academic Press, Amsterdam, fifth edition edition, 2013. ISBN 978-0-12-397023-7.

[2] H. J. Bakker, G. C. Cho, H. Kurz, Q. Wu, and X.-C. Zhang. Distortion of terahertz pulses in electro-optic sampling. *Journal of the Optical Society of America B*, 15(6): 1795, June 1998. ISSN 0740-3224, 1520-8540. doi: 10.1364/JOSAB.15.001795.

[3] G. Bell and M. Hilke. Polarization Effects of Electro-optic Sampling and Over-rotation for High Field THz Detection. *Journal of Infrared, Millimeter, and Terahertz Waves*, 41(8):880–893, Aug. 2020. ISSN 1866-6892, 1866-6906. doi: 10.1007/s10762-020-00724-z.

[4] Ch. Bosshard, R. Spreiter, M. Zgonik, and P. Günter. Kerr Nonlinearity via Cascaded Optical Rectification and the Linear Electro-optic Effect. *Physical Review Letters*, 74 (14):2816–2819, Apr. 1995. ISSN 0031-9007, 1079-7114. doi: 10.1103/PhysRevLett.74.2816.

[5] G. D. Boyd and D. A. Kleinman. Parametric Interaction of Focused Gaussian Light Beams. *Journal of Applied Physics*, 39(8):3597–3639, July 1968. ISSN 0021-8979. doi: 10.1063/1.1656831.

[6] G. D. Boyd and M. A. Pollack. Microwave Nonlinearities in Anisotropic Dielectrics and Their Relation to Optical and Electro-Optical Nonlinearities. *Physical Review B*, 7 (12):5345–5359, June 1973. ISSN 0556-2805. doi: 10.1103/PhysRevB.7.5345.

[7] R. W. Boyd. *Nonlinear Optics*. Academic Press, Amsterdam ; Boston, 3rd ed edition, 2008. ISBN 978-0-12-369470-6.

[8] R. N. Bracewell. *The Fourier Transform and Its Applications*. McGraw-Hill Series in Electrical and Computer Engineering. McGraw Hill, Boston, 3rd ed edition, 2000. ISBN 978-0-07-303938-1.

[9] T. O. Buchmann. *High-Power Terahertz Generation at Megahertz Repetition Rates Using Few-Cycle Pulses*. PhD thesis, Technical University of Denmark, 2021.

[10] J.-P. Caumes, L. Videau, C. Rouyer, and E. Freysz. Kerr-Like Nonlinearity Induced via Terahertz Generation and the Electro-Optical Effect in Zinc Blende Crystals. *Physical*

Review Letters, 89(4):047401, July 2002. ISSN 0031-9007, 1079-7114. doi: 10.1103/PhysRevLett.89.047401.

[11] T. Chen, X. Wang, P. Han, W. Sun, S. Feng, J. Ye, Y. Xu, and Y. Zhang. First- and second-order photon–phonon interactions and optical parameters of ZnTe crystal: A broadband terahertz time-domain spectroscopy study. *Journal of Physics D: Applied Physics*, 52 (45):455101, Aug. 2019. ISSN 0022-3727. doi: 10.1088/1361-6463/ab36cb.

[12] X. Chen, S. He, Z. Shen, F. Li Zhao, K. Y. Xu, G. Wang, R. Wang, and N. Dai. Influence of nonlinear effects in ZnTe on generation and detection of terahertz waves. *Journal of Applied Physics*, 105(2):023106, Jan. 2009. ISSN 0021-8979, 1089-7550. doi: 10.1063/1.3068480.

[13] E. Collett. *Field Guide to Polarization*. SPIE, Sept. 2005. ISBN 978-0-8194-7820-7. doi: 10.1117/3.626141.

[14] M. Cornet, J. Degert, E. Abraham, and E. Freysz. Terahertz Kerr effect in gallium phosphide crystal. *Journal of the Optical Society of America B*, 31(7):1648, July 2014. ISSN 0740-3224, 1520-8540. doi: 10.1364/JOSAB.31.001648.

[15] M. Cornet, J. Degert, E. Abraham, and E. Freysz. Terahertz-field-induced second harmonic generation through Pockels effect in zinc telluride crystal. *Optics Letters*, 39(20): 5921, Oct. 2014. ISSN 0146-9592, 1539-4794. doi: 10.1364/OL.39.005921.

[16] J. Dai, J. Zhang, W. Zhang, and D. Grischkowsky. Terahertz time-domain spectroscopy characterization of the far-infrared absorption and index of refraction of high-resistivity, float-zone silicon. *JOSA B*, 21(7):1379–1386, July 2004. ISSN 1520-8540. doi: 10.1364/JOSAB.21.001379.

[17] Ph. Dittrich, R. Bartlome, G. Montemezzani, and P. Günter. Femtosecond laser ablation of DAST. *Applied Surface Science*, 220(1):88–95, Dec. 2003. ISSN 0169-4332. doi: 10.1016/S0169-4332(03)00745-1.

[18] E. Freysz and J. Degert. Terahertz Kerr effect. *Nature Photonics*, 4(3):131–132, Mar. 2010. ISSN 1749-4885, 1749-4893. doi: 10.1038/nphoton.2010.14.

[19] G. Gallot and D. Grischkowsky. Electro-optic detection of terahertz radiation. *JOSA B*, 16(8):1204–1212, Aug. 1999. ISSN 1520-8540. doi: 10.1364/JOSAB.16.001204.

[20] G. Gallot, J. Zhang, R. W. McGowan, T.-I. Jeon, and D. Grischkowsky. Measurements of the THz absorption and dispersion of ZnTe and their relevance to the electro-optic detection of THz radiation. *Applied Physics Letters*, 74(23):3450–3452, June 1999. ISSN 0003-6951, 1077-3118. doi: 10.1063/1.124124.

[21] C. Gollner, M. Shalaby, C. Brodeur, I. Astrauskas, R. Jutas, E. Constable, L. Bergen, A. Baltuška, and A. Pugžlys. Highly efficient THz generation by optical rectification of mid-IR pulses in DAST. *APL Photonics*, 6(4):046105, Apr. 2021. ISSN 2378-0967. doi: 10.1063/5.0037235.

[22] I. E. Gordon, L. S. Rothman, R. J. Hargreaves, R. Hashemi, E. V. Karlovets, F. M. Skinner, E. K. Conway, C. Hill, R. V. Kochanov, Y. Tan, P. Wcisło, A. A. Finenko, K. Nelson, P. F. Bernath, M. Birk, V. Boudon, A. Campargue, K. V. Chance, A. Coustenis, B. J. Drouin, J. –. Flaud, R. R. Gamache, J. T. Hodges, D. Jacquemart, E. J. Mlawer, A. V. Nikitin, V. I. Perevalov, M. Rotger, J. Tennyson, G. C. Toon, H. Tran, V. G. Tyuterev, E. M. Adkins, A. Baker, A. Barbe, E. Canè, A. G. Császár, A. Dudaryonok, O. Egorov, A. J. Fleisher, H. Fleurbaey, A. Foltynowicz, T. Furtenbacher, J. J. Harrison, J. –. Hartmann, V. –. Horneman, X. Huang, T. Karman, J. Karns, S. Kassi, I. Kleiner, V. Kofman, F. Kwabia–Tchana, N. N. Lavrentieva, T. J. Lee, D. A. Long, A. A. Lukashevskaya, O. M. Lyulin, V. Yu. Makhnev, W. Matt, S. T. Massie, M. Melosso, S. N. Mikhailenko, D. Mondelain, H. S. P. Müller, O. V. Naumenko, A. Perrin, O. L. Polyansky, E. Raddaoui, P. L. Raston, Z. D. Reed, M. Rey, C. Richard, R. Tóbiás, I. Sadiek, D. W. Schwenke, E. Starikova, K. Sung, F. Tamassia, S. A. Tashkun, J. Vander Auwera, I. A. Vasilenko, A. A. Vigasin, G. L. Villanueva, B. Vispoel, G. Wagner, A. Yachmenev, and S. N. Yurchenko. The HITRAN2020 molecular spectroscopic database. *Journal of Quantitative Spectroscopy and Radiative Transfer*, 277:107949, Jan. 2022. ISSN 0022-4073. doi: 10.1016/j.jqsrt.2021.107949.

[23] D. J. Griffiths. *Introduction to Electrodynamics*. Pearson, Boston, fourth edition edition, 2013. ISBN 978-0-321-85656-2.

[24] C. R. Harris, K. J. Millman, S. J. van der Walt, R. Gommers, P. Virtanen, D. Cournapeau, E. Wieser, J. Taylor, S. Berg, N. J. Smith, R. Kern, M. Picus, S. Hoyer, M. H. van Kerkwijk, M. Brett, A. Haldane, J. F. del Río, M. Wiebe, P. Peterson, P. Gérard-Marchant, K. Sheppard, T. Reddy, W. Weckesser, H. Abbasi, C. Gohlke, and T. E. Oliphant. Array programming with NumPy. *Nature*, 585(7825):357–362, Sept. 2020. ISSN 1476-4687. doi: 10.1038/s41586-020-2649-2.

[25] M. Hase, M. Kitajima, A. M. Constantinescu, and H. Petek. The birth of a quasiparticle in silicon observed in time–frequency space. *Nature*, 426(6962):51–54, Nov. 2003. ISSN 1476-4687. doi: 10.1038/nature02044.

[26] A. Hindmarsh. ODEPACK. A Collection of ODE System Solvers. Technical Report ESTSC-000166CY00100; NESC-9935, Lawrence Livermore National Lab. (LLNL), Livermore, CA (United States), Jan. 1992.

[27] M. C. Hoffmann, N. C. Brandt, H. Y. Hwang, K.-L. Yeh, and K. A. Nelson. Terahertz Kerr effect. *Applied Physics Letters*, 95(23):231105, Dec. 2009. ISSN 0003-6951. doi: 10.1063/1.3271520.

[28] M. C. Hoffmann, J. Hebling, H. Y. Hwang, K.-L. Yeh, and K. A. Nelson. Impact ionization in InSb probed by terahertz pump—terahertz probe spectroscopy. *Physical Review B*, 79(16):161201, Apr. 2009. doi: 10.1103/PhysRevB.79.161201.

[29] A. V. Husakou and J. Herrmann. Supercontinuum Generation of Higher-Order Solitons by Fission in Photonic Crystal Fibers. *Physical Review Letters*, 87(20):4, 2001.

[30] M. Jazbinsek, U. Puc, A. Abina, and A. Zidansek. Organic Crystals for THz Photonics. *Applied Sciences*, 9(5):882, Jan. 2019. doi: 10.3390/app9050882.

[31] M. Jewariya, M. Nagai, and K. Tanaka. Enhancement of terahertz wave generation by cascaded \chi{(2)} processes in LiNbO_3. *Journal of the Optical Society of America B*, 26(9):A101, Sept. 2009. ISSN 0740-3224, 1520-8540. doi: 10.1364/JOSAB.26.00A101.

[32] C. L. Johnson, B. E. Knighton, and J. A. Johnson. Distinguishing Nonlinear Terahertz Excitation Pathways with Two-Dimensional Spectroscopy. *Physical Review Letters*, 122(7):073901, Feb. 2019. ISSN 0031-9007, 1079-7114. doi: 10.1103/PhysRevLett.122.073901.

[33] M. Kolesik and J. V. Moloney. Nonlinear optical pulse propagation simulation: From Maxwell's to unidirectional equations. *Physical Review E*, 70(3):036604, Sept. 2004. ISSN 1539-3755, 1550-2376. doi: 10.1103/PhysRevE.70.036604.

[34] W. Kuehn, K. Reimann, M. Woerner, and T. Elsaesser. Phase-resolved two-dimensional spectroscopy based on collinear n-wave mixing in the ultrafast time domain. *The Journal of Chemical Physics*, 130(16):164503, Apr. 2009. ISSN 0021-9606, 1089-7690. doi: 10.1063/1.3120766.

[35] W. Kuehn, K. Reimann, M. Woerner, T. Elsaesser, and R. Hey. Two-Dimensional Terahertz Correlation Spectra of Electronic Excitations in Semiconductor Quantum Wells. *The Journal of Physical Chemistry B*, 115(18):5448–5455, May 2011. ISSN 1520-6106, 1520-5207. doi: 10.1021/jp1099046.

[36] H. H. Li. Refractive Index of ZnS, ZnSe, and ZnTe and Its Wavelength and Temperature Derivatives. *Journal of Physical and Chemical Reference Data*, 13(1):103–150, Jan. 1984. ISSN 0047-2689, 1529-7845. doi: 10.1063/1.555705.

[37] X. Li, T. Qiu, J. Zhang, E. Baldini, J. Lu, A. M. Rappe, and K. A. Nelson. Terahertz field–induced ferroelectricity in quantum paraelectric SrTiO $_3$. *Science*, 364(6445):1079–1082, June 2019. ISSN 0036-8075, 1095-9203. doi: 10.1126/science.aaw4913.

[38] H.-W. Lin, G. Mead, and G. A. Blake. Mapping ${\mathrm{LiNbO}}_{3}$ Phonon-Polariton Nonlinearities with 2D THz-THz-Raman Spectroscopy. *Physical Review Letters*, 129(20):207401, Nov. 2022. doi: 10.1103/PhysRevLett.129.207401.

[39] S. Maehrlein, A. Paarmann, M. Wolf, and T. Kampfrath. Terahertz Sum-Frequency Excitation of a Raman-Active Phonon. *Physical Review Letters*, 119(12):127402, Sept. 2017. ISSN 0031-9007, 1079-7114. doi: 10.1103/PhysRevLett.119.127402.

[40] D. Malacara, editor. *Optical Shop Testing*. Wiley Series in Pure and Applied Optics. Wiley-Interscience, Hoboken, N.J, 3rd ed edition, 2007. ISBN 978-0-471-48404-2.

[41] I. H. Malitson. Interspecimen Comparison of the Refractive Index of Fused Silica*,†. *JOSA*, 55(10):1205–1209, Oct. 1965. doi: 10.1364/JOSA.55.001205.

[42] G. Mead, H.-W. Lin, I.-B. Magdău, T. F. I. Miller, and G. A. Blake. Sum-Frequency Signals in 2D-Terahertz-Terahertz-Raman Spectroscopy. *The Journal of Physical Chemistry B*, 124(40):8904–8908, Oct. 2020. ISSN 1520-6106. doi: 10.1021/acs.jpcb.0c07935.

[43] T. F. Nova, A. S. Disa, M. Fechner, and A. Cavalleri. Metastable ferroelectricity in optically strained $SrTiO_3$. *Science*, 364(6445):1075–1079, June 2019. ISSN 0036-8075, 1095-9203. doi: 10.1126/science.aaw4911.

[44] S. Pal, N. Strkalj, C.-J. Yang, M. C. Weber, M. Trassin, M. Woerner, and M. Fiebig. Origin of Terahertz Soft-Mode Nonlinearities in Ferroelectric Perovskites. *Physical Review X*, 11(2):021023, Apr. 2021. ISSN 2160-3308. doi: 10.1103/PhysRevX.11.021023.

[45] P. C. M. Planken, H.-K. Nienhuys, H. J. Bakker, and T. Wenckebach. Measurement and calculation of the orientation dependence of terahertz pulse detection in ZnTe. *Journal of the Optical Society of America B*, 18(3):313, Mar. 2001. ISSN 0740-3224, 1520-8540. doi: 10.1364/JOSAB.18.000313.

[46] A. Rice, Y. Jin, X. F. Ma, X.-C. Zhang, D. Bliss, J. Larkin, and M. Alexander. Terahertz optical rectification from $\langle 110 \rangle$ zinc-blende crystals. *Applied Physics Letters*, 64(11):1324–1326, Mar. 1994. ISSN 0003-6951. doi: 10.1063/1.111922.

[47] M. Schall and P. U. Jepsen. Above-band gap two-photon absorption and its influence on ultrafast carrier dynamics in ZnTe and CdTe. *Applied Physics Letters*, 80(25):4771–4773, June 2002. ISSN 0003-6951, 1077-3118. doi: 10.1063/1.1489480.

[48] M. Schall, M. Walther, and P. Uhd Jepsen. Fundamental and second-order phonon processes in CdTe and ZnTe. *Physical Review B*, 64(9):094301, Aug. 2001. ISSN 0163-1829, 1095-3795. doi: 10.1103/PhysRevB.64.094301.

[49] M. Shalaby and C. P. Hauri. Demonstration of a low-frequency three-dimensional terahertz bullet with extreme brightness. *Nature Communications*, 6(1):5976, Jan. 2015. ISSN 2041-1723. doi: 10.1038/ncomms6976.

[50] S. J. Sheldon, L. V. Knight, and J. M. Thorne. Laser-induced thermal lens effect: A new theoretical model. *Applied Optics*, 21(9):1663, May 1982. ISSN 0003-6935, 1539-4522. doi: 10.1364/AO.21.001663.

[51] J. Shi, Y.-Q. Bie, W. Chen, S. Fang, J. Han, Z. Cao, T. Taniguchi, K. Watanabe, V. Bulović, E. Kaxiras, P. Jarillo-Herrero, and K. A. Nelson. Terahertz-driven irreversible topological phase transition in two-dimensional MoTe$_{2}$. *arXiv:1910.13609 [cond-mat, physics:physics]*, Oct. 2019.

[52] D. Sidler and P. Hamm. A Feynman diagram description of the 2D-Raman-THz response of amorphous ice. *The Journal of Chemical Physics*, 153(4):044502, July 2020. ISSN 0021-9606. doi: 10.1063/5.0018485.

[53] A. E. Siegman. *Lasers*. University Science Books, Mill Valley, California, 1986. ISBN 978-0-935702-11-8 978-0-19-855713-5.

[54] P. Steglich, C. Mai, C. Villringer, and A. Mai. Direct observation and simultaneous use of linear and quadratic electro-optical effects. *Journal of Physics D: Applied Physics*, 53(12):125106, Mar. 2020. ISSN 0022-3727, 1361-6463. doi: 10.1088/1361-6463/ab6059.

[55] R. Trebino. *Frequency-Resolved Optical Gating: The Measurement of Ultrashort Laser Pulses*. Springer US, Boston, MA, 2000. ISBN 978-1-4613-5432-1 978-1-4615-1181-6. doi: 10.1007/978-1-4615-1181-6.

[56] S. Vidal, J. Degert, M. Tondusson, J. Oberlé, and E. Freysz. Impact of dispersion, free carriers, and two-photon absorption on the generation of intense terahertz pulses in ZnTe crystals. *Applied Physics Letters*, 98(19):191103, May 2011. ISSN 0003-6951, 1077-3118. doi: 10.1063/1.3588411.

[57] P. Virtanen, R. Gommers, T. E. Oliphant, M. Haberland, T. Reddy, D. Cournapeau, E. Burovski, P. Peterson, W. Weckesser, J. Bright, S. J. Van Der Walt, M. Brett, J. Wilson, K. J. Millman, N. Mayorov, A. R. J. Nelson, E. Jones, R. Kern, E. Larson, C. J. Carey, İ. Polat, Y. Feng, E. W. Moore, J. VanderPlas, D. Laxalde, J. Perktold, R. Cimrman, I. Henriksen, E. A. Quintero, C. R. Harris, A. M. Archibald, A. H. Ribeiro, F. Pedregosa, P. Van Mulbregt, SciPy 1.0 Contributors, A. Vijaykumar, A. P. Bardelli, A. Rothberg, A. Hilboll, A. Kloeckner, A. Scopatz, A. Lee, A. Rokem, C. N. Woods, C. Fulton, C. Masson, C. Häggström, C. Fitzgerald, D. A. Nicholson, D. R. Hagen, D. V. Pasechnik, E. Olivetti, E. Martin, E. Wieser, F. Silva, F. Lenders, F. Wilhelm, G. Young, G. A. Price, G.-L. Ingold, G. E. Allen, G. R. Lee, H. Audren, I. Probst, J. P. Dietrich, J. Silterra, J. T. Webber, J. Slavič, J. Nothman, J. Buchner, J. Kulick, J. L. Schönberger, J. V. De Miranda Cardoso, J. Reimer, J. Harrington, J. L. C. Rodríguez, J. Nunez-Iglesias, J. Kuczynski, K. Tritz, M. Thoma, M. Newville, M. Kümmerer, M. Bolingbroke, M. Tartre, M. Pak, N. J. Smith, N. Nowaczyk, N. Shebanov, O. Pavlyk, P. A. Brodtkorb, P. Lee, R. T. McGibbon, R. Feldbauer, S. Lewis, S. Tygier, S. Sievert, S. Vigna, S. Peterson, S. More, T. Pudlik, T. Oshima, T. J. Pingel, T. P. Robitaille, T. Spura, T. R. Jones, T. Cera, T. Leslie, T. Zito, T. Krauss, U. Upadhyay, Y. O. Halchenko, and Y. Vázquez-Baeza. SciPy 1.0: Fundamental algorithms for scientific computing in Python. *Nature Methods*, 17(3):261–272, Mar. 2020. ISSN 1548-7091, 1548-7105. doi: 10.1038/s41592-019-0686-2.

[58] WiredSense. How to align optical delay stages correctly within 5 minutes. https://www.wiredsense.com/en/tutorials/how-to-align-optical-delay-stages-correctly-within-5-minutes, June 2023.

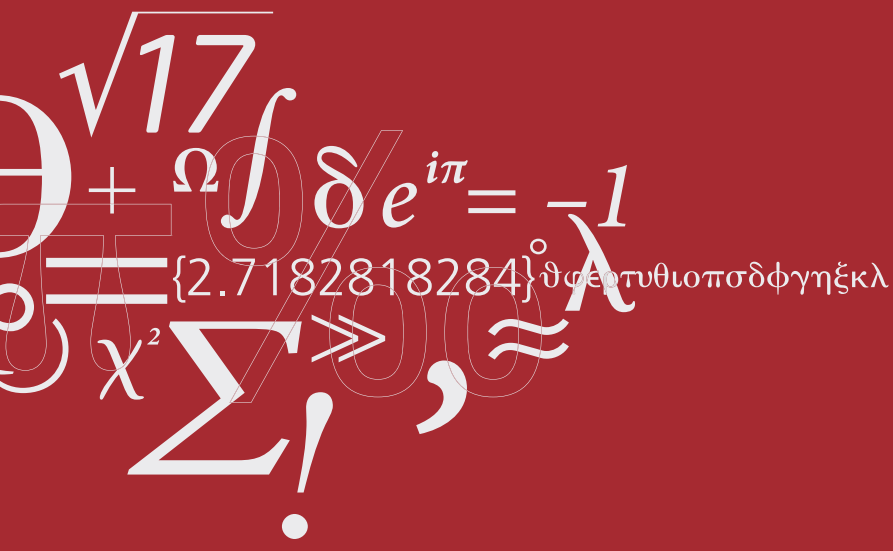
$\sqrt{17}$
$\Omega \int \delta e^{i\pi} = -1$
{2.7182818284}
ϑφέρτυθιοπσδφγηξκλ
χ^2
$\sum$
$\gg$
$\approx$
λ